

JAN 2
G
AEC RESE/
DEVELOPMENT
OCTO

Prime No.

GEAP-4386

Secondary Nos.

 ACCENT
ON VALUE



MASTER

**THE FEASIBILITY OF USING
IN-CORE ION CHAMBERS TO COVER
THE COMPLETE REACTOR NEUTRON
FLUX RANGE FROM STARTUP
TO FULL POWER**

**IN-CORE INSTRUMENTATION
DEVELOPMENT PROGRAM
QUARTERLY PROGRESS REPORT
JUNE - SEPTEMBER 1963**

By
R.A. DuBRIDGE

U.S. ATOMIC ENERGY COMMISSION
CONTRACT AT(04-3)-189
PROJECT AGREEMENT 22

Facsimile Price \$ 10.50
Microfilm Price \$ 4.34

Available from the
Office of Technical Services
Department of Commerce
Washington 25, D. C.

ATOMIC POWER EQUIPMENT DEPARTMENT
GENERAL  ELECTRIC
SAN JOSE, CALIFORNIA

GEAP-4386
AEC Research and
Development Report
October, 1963

**THE FEASIBILITY OF USING IN-CORE ION CHAMBERS
TO COVER THE COMPLETE REACTOR NEUTRON FLUX RANGE
FROM STARTUP TO FULL POWER.**

**IN-CORE INSTRUMENTATION DEVELOPMENT PROGRAM
QUARTERLY PROGRESS REPORT
JUNE - SEPTEMBER 1963**

By

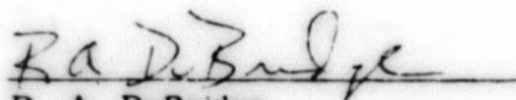
R. A. DuBridge

**U. S. Atomic Energy Commission
Contract AT(04-3)-189
Project Agreement 22**

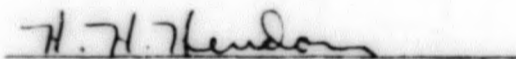
Printed in U. S. A. Price \$2. 00. Copies Available from
Office of Technical Services, Department of Commerce
Washington 25, D. C.

**ATOMIC POWER EQUIPMENT DEPARTMENT
GENERAL  ELECTRIC
SAN JOSE, CALIFORNIA**

APPROVED BY:



R. A. DuBridge
Project Engineer



H. H. Hendon, Manager
NEPS Advanced Development

TABLE OF CONTENTS

| | | <u>Page No.</u> |
|-------------|----------------------------------------------------|-----------------|
| | INTRODUCTION | 1 |
| SECTION I | ION CHAMBER DESIGNS AND EXPERIMENTAL SETUPS | 2 |
| SECTION II | MEAN SQUARE FLUCTUATION VOLTAGES FROM ION CHAMBERS | 8 |
| SECTION III | COUNTING WITH IN-CORE ION CHAMBERS | 27 |
| | BIBLIOGRAPHY | 83 |

LEGAL NOTICE

This report was prepared as an account of Government sponsored work. Neither the United States, nor the Commission, nor any person acting on behalf of the Commission:

- A. Makes any warranty or representation, expressed or implied, with respect to the accuracy, completeness, or usefulness of the information contained in this report, or that the use of any information, apparatus, method, or process disclosed in this report may not infringe privately owned rights; or*
- B. Assumes any liabilities with respect to the use of, or for damages resulting from the use of any information, apparatus, method, or process disclosed in this report.*

As used in the above, "person acting on behalf of the Commission" includes any employee or contractor of the Commission, or employee of such contractor, to the extent that such employee or contractor of the Commission, or employee of such contractor prepares, disseminates, or provides access to, any information pursuant to his employment or contract with the Commission, or his employment with such contractor.

LIST OF ILLUSTRATIONS

| <u>Figure No.</u> | <u>Title</u> | <u>Page No.</u> |
|---------------------|----------------------------------------------------------------------------------------------------------------------------------------|------------------|
| 1-1 | Long Ion Chamber | 3 |
| 1-2 | Short Ion Chamber | 4 |
| 1-3 | Upper End Connector | 5 |
| 1-4 | Horizontal Flux Traverse | 6 |
| 1-5 | Gamma Dose vs. Thermal Neutron Flux (Center of Horizontal Channel at NTR) | 7 |
| 2-1 | Mean Square Fluctuation Voltage Block Diagram | 17 |
| 2-2 | Detector - Amplifier Equivalent Circuit | 17 |
| 2-3 | RMS and D-c Sensitivities for Short Fully Enriched Ion Chamber | 18 |
| 2-4 | RMS Voltage vs. Neutron Flux Short Fully Enriched Ion Chamber Amplifier Bandwidth 0.5 - 13.6 KC, Gain of 72 | 19 |
| 2-5 | RMS Voltage vs. Neutron Flux Long Fully Enriched Ion Chamber, Bandwidth 0.63 - 228 KC, Gain 100 | 20 |
| 2-6 | RMS Voltage vs. Neutron Flux Long Fully Enriched Ion Chamber, Bandwidth 0.63 - 228 KC, Gain 100 | 21 |
| 2-7 | RMS Voltage vs. Neutron Flux Short Fully Enriched Ion Chamber, Bandwidth 0.63 - 228 KC, Gain 100 | 22 |
| 2-8 | RMS Voltage vs. Neutron Flux Short Fully Enriched Ion Chamber, Bandwidth 0.63 - 228 KC, Gain 100 | 23 |
| 2-9 | RMS Voltage vs. Neutron Flux, Short Fully Enriched Ion Chamber, with N ₂ , Amplifier Bandwidth of 0.5 - 13.6 KC, Gain of 72 | 24 |
| 2-10 | RMS Voltage vs. Neutron Flux, Short Fully Enriched Ion Chamber with He, Amplifier Bandwidth 0.5 - 13.6 KC, Gain of 72 | 25 |
| 2-11 | RMS Voltage and D-c Current Neutron Flux for Argon, P = 2.36 ATM, in a Short Fully Enriched Chamber | 26 |
| 3-1 | Average Energy to Ionize (W) | 30 |
| 3-2 | Ionization and Excitation Potentials | 30 |
| 3-3 | Electron + Positive Ion Mobilities, Velocities + Collection Times | 31 |
| 3-4 | Counting Experiments, Block Diagram | 32 |
| 3-5 thru 3-54 | Differential and Integral Bias Curves | 33 thru 82 |

INTRODUCTION

The objective of Project Agreement 22 is to determine the feasibility of covering the complete reactor neutron flux startup range from $10^3 - 5 \times 10^{13}$ nv by using in-core ion chambers. The counting mode of operation will be used at low neutron fluxes and the root mean square voltage fluctuation mode will be used at high neutron flux levels.

Experiments have been run utilizing various ion chambers, gases, gas pressures, voltages, and cables to measure sensitivities and ranges operating in the counting and RMS voltage modes. Theoretical discussions are presented showing how the RMS voltage is related to individual pulse at both amplifier input and output. Noise is also compared at amplifier output so that the optimum bandwidth can be selected. Spectral shifts with changes in applied voltage causing signal variations have been examined and can be eliminated by appropriate selection of amplifier bandwidth. In the counting mode, all experiments have been conducted with unterminated cable. The chamber has been designed with geometry, gas, and pressure to completely stop fission fragments in the gas and hence maximize the charge generated in the chamber. Cables have been selected to minimize capacity. Various gases, pressures, and voltages have been used to determine that an optimum design has been achieved.

SECTION I

ION CHAMBER DESIGNS AND EXPERIMENTAL SETUPS

The ion chambers designed for this study are shown in Figures 1-1 and 1-2. These basic designs were provided with various coatings for various experiments. Below is the nomenclature used throughout this report to identify the various chambers.

| <u>Ion Chamber</u> | <u>d₂</u> <u>(in.)</u> | <u>d₁</u> <u>(in.)</u> | <u>L</u> <u>(in.)</u> | <u>Coating</u> | <u>Enrichment</u> <u>Percent</u> | <u>Thickness</u> <u>(mgm/cm²)</u> | <u>Location</u> <u>of Coating</u> |
|------------------------------|--------------------------------------|--------------------------------------|--------------------------|-------------------------------|-------------------------------------|-------------------------------------------------|--------------------------------------|
| Long fully enriched | 0.210 | 0.194 | 9 | U ₃ O ₈ | 93 | 0.4 | Collector |
| Short fully enriched | 0.209 | 0.169 | 1 | U ₃ O ₈ | 93 | 2.0 | Case |
| Long 1.5 percent enriched | 0.210 | 0.194 | 9 | U ₃ O ₈ | 1.5 | 2.0 | Collector |
| Short gamma | 0.210 | 0.194 | 1 | None | 0 | 0 | None |

All chambers were equipped with a gas fill tube from the bottom end of the chamber so that the chamber gas and pressure could be changed while the chamber was in the reactor or isotopic source. The chambers were always evacuated and flushed at least three times before measurements were taken. Only the purest commercial gases were used.

The chambers have a number of noteworthy features. They are all exterior 304 stainless steel and welded construction. They are fabricated of materials which can be used in core to at least 1000 F for very long exposures. They employ upper (see Figure 103) and lower end seals which can be baked at 1000 F, thus permitting complete cable bakeout at that temperature. Long ion chambers were developed for average flux measurements.

The RMS Voltage experiments were all conducted at the General Electric Nuclear Test Reactor (NTR). The thermal and epithermal neutron fluxes are shown in Figure 1-4. The gamma dose rate versus neutron flux levels is shown in Figure 1-5. The counting experiments were all conducted at the Vallecitos Atomic Laboratory in a Pu-Be 10-curie neutron source.

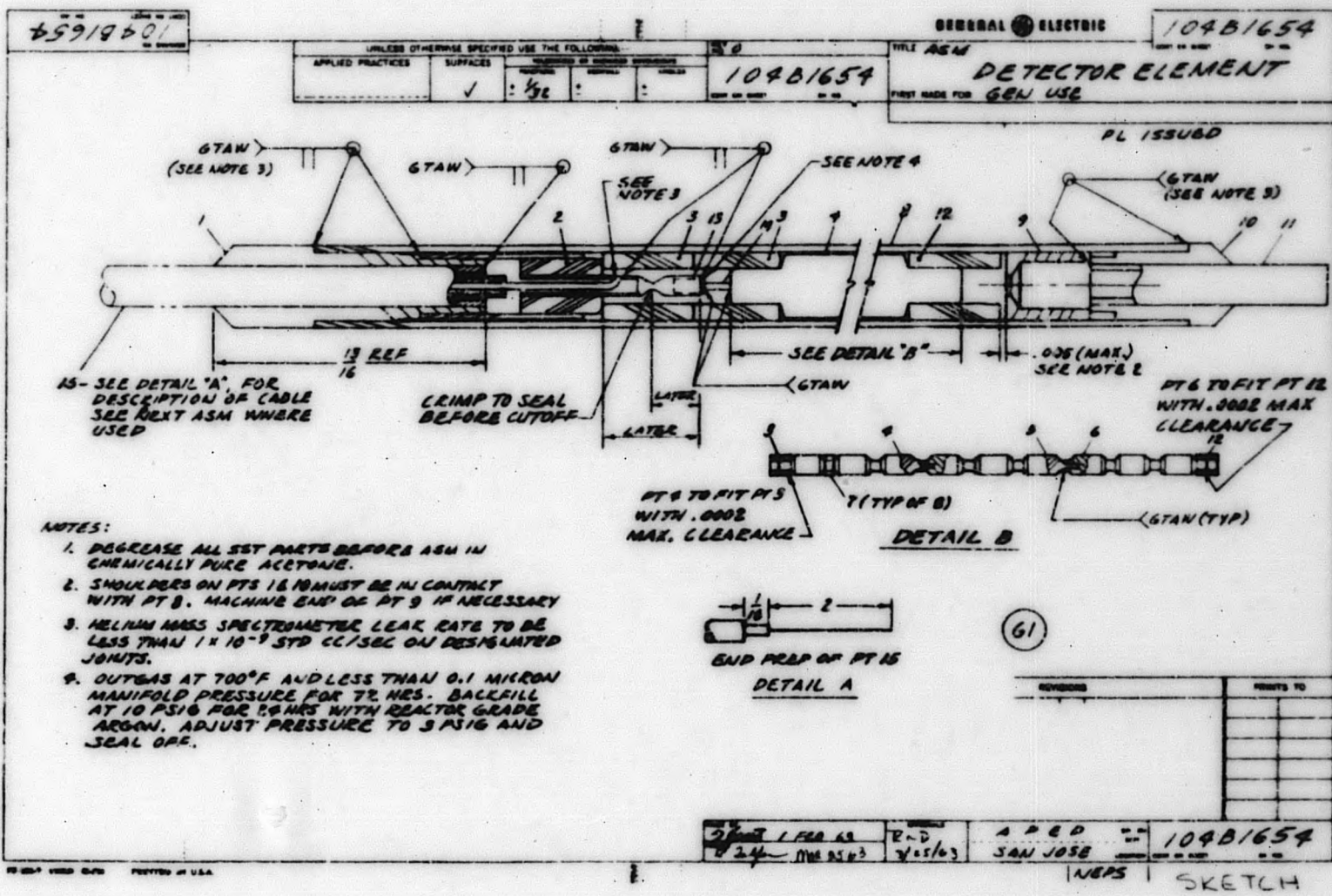


Figure 1-1. Long Ion Chamber

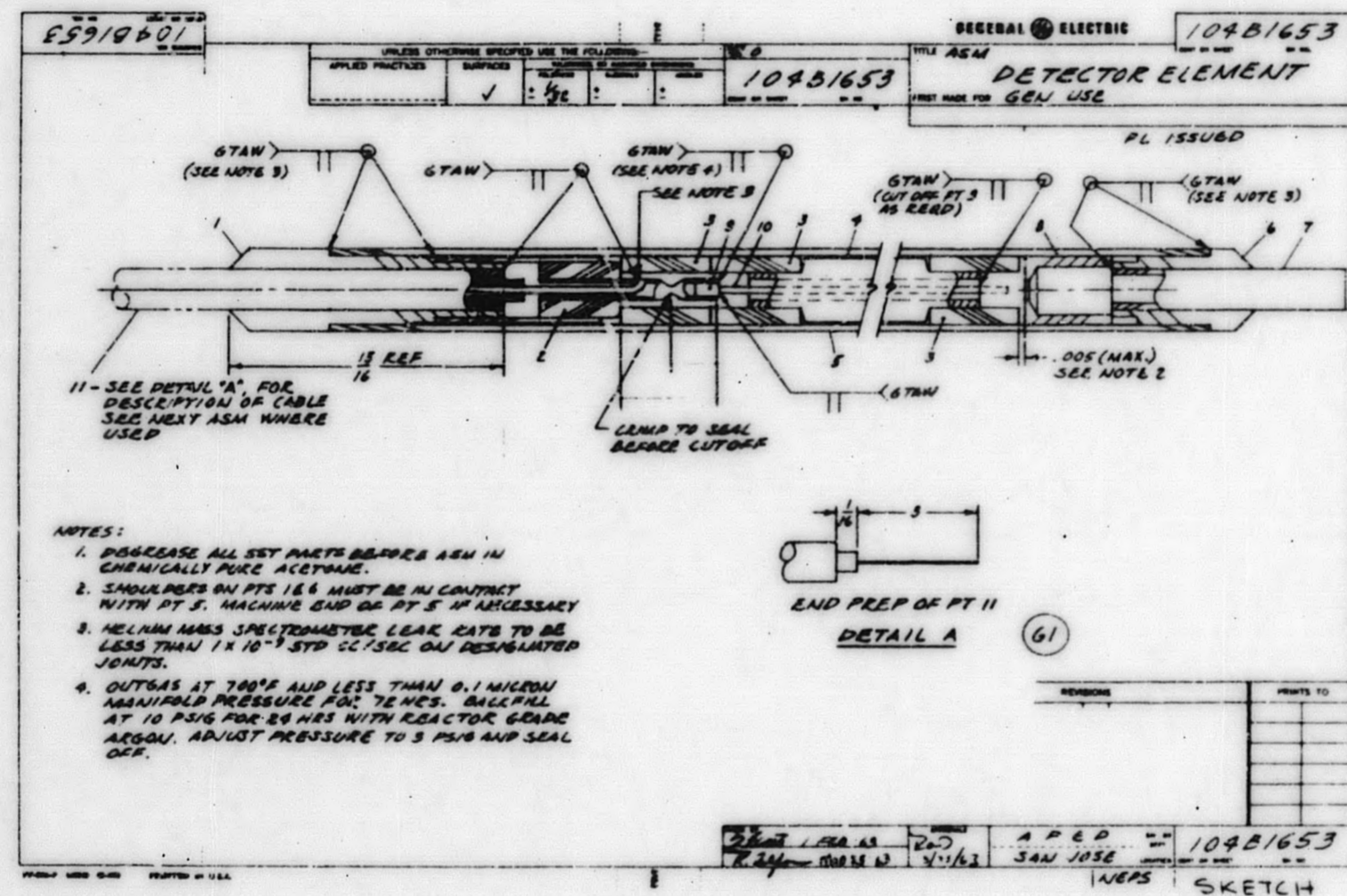
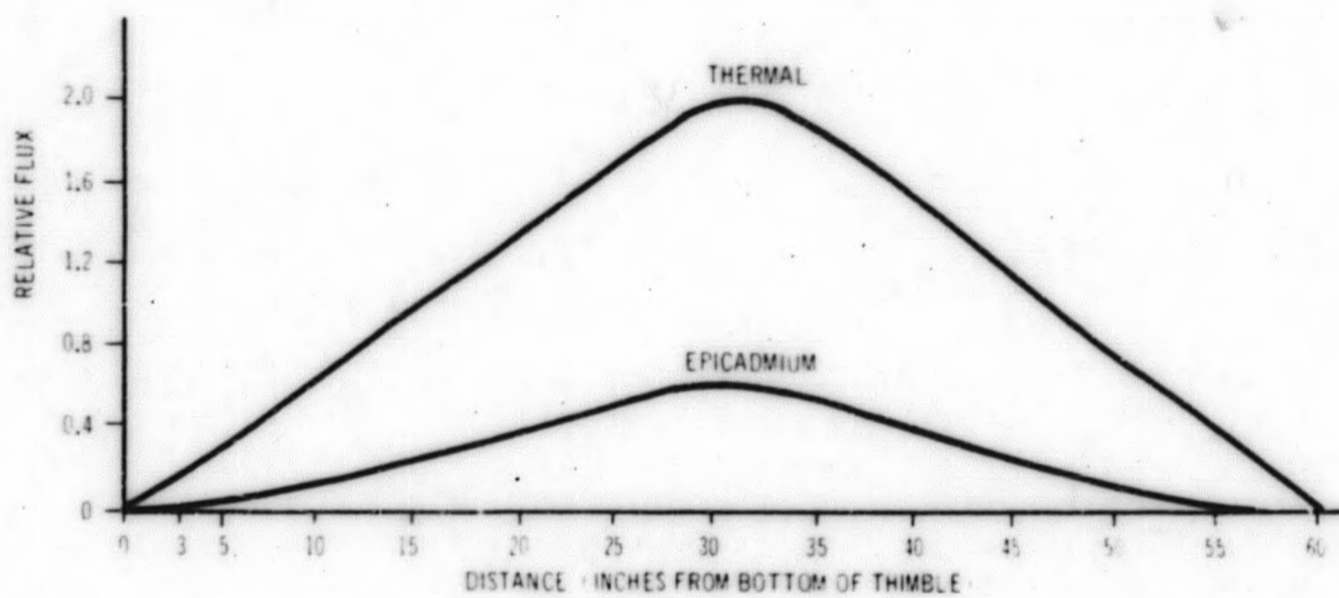
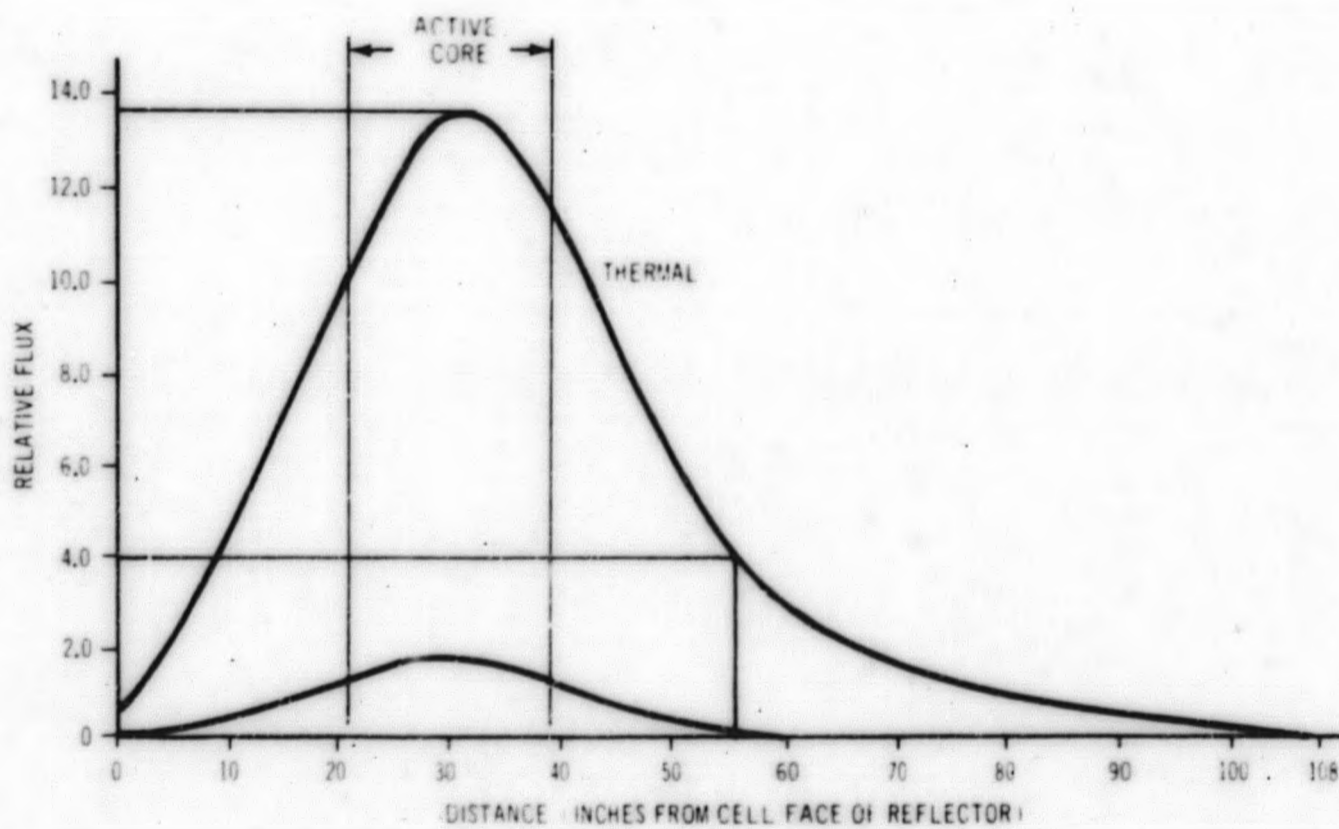


Figure 1-2. Short Ion Chamber

GEAP-4386



VERTICAL FLUX TRAVERSE



HORIZONTAL FLUX TRAVERSE

1169-1

Figure 1-4. Horizontal Flux Traverse

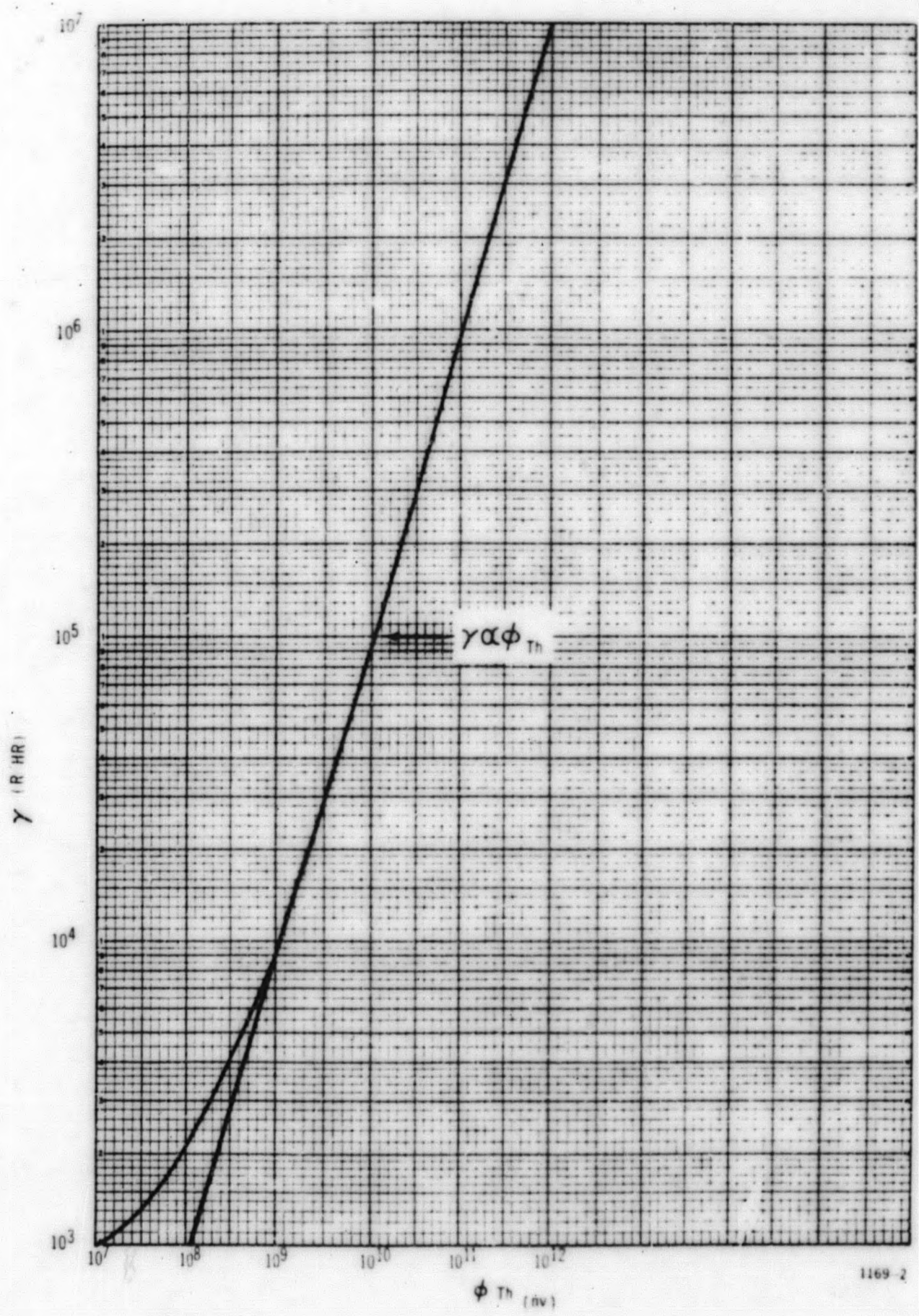


Figure 1-5. Gamma Dose vs Thermal Neutron Flux (Center of Horizontal Channel at NTR)

SECTION II

MEAN SQUARE FLUCTUATION VOLTAGES FROM ION CHAMBERS

The object of this study is to determine the feasibility of using in-core ion chambers to cover the complete reactor neutron flux startup range. Two modes of operation are envisioned, a counting mode for low flux levels (see Section III) and the mean square fluctuation voltage mode at intermediate and high flux levels (Section II). D-c operated ion chambers cannot be used at intermediate flux levels because of gamma and d-c leakage interference currents; hence, mean square fluctuation voltage must be measured to circumvent these two problems.

D-c current interferences at any neutron flux level can be calculated from the following equations.

$$\begin{aligned} i_o &= S_o o \\ i_\gamma &= S_\gamma \gamma \\ i_L &= \frac{V_p}{R_L} \end{aligned}$$

In this section, the mean square fluctuation voltage mode of operation will be analyzed and experimental results to date given.

It can be shown ⁽¹⁾ that the mean square fluctuation voltage ($\langle U^2 \rangle - \langle U \rangle^2$) at the output of the detector and cable is related to the individual pulse ($v(t)$) and the average rate of pulse occurrence (\bar{N}) by

$$\langle U^2 \rangle - \langle U \rangle^2 = \bar{N} \int_0^\infty [v(t)]^2 dt$$

This subtraction can be performed electronically by blocking $\langle U \rangle^2$ with a capacitor and shunting it to ground and measuring the remainder ($\langle V^2 \rangle$). This is shown in Figure 2-1. The obvious advantage to measuring $\langle V^2 \rangle$ rather than $\langle i \rangle$ is that it is an a-c measurement and hence avoids d-c leakage current interferences and also that the larger pulses (e. g. , fission) are magnified with respect to smaller pulses (e. g. , gamma) by the ratio

$$\frac{\int_0^\infty [v(t)]_o^2 dt}{\int_0^\infty [v(t)]_\gamma^2 dt}$$

Comparing the d-c current output ($\langle i \rangle$) as related to rate of pulse occurrence (\bar{N}) and pulse shape ($i(t)$)

$$\langle i \rangle = \bar{N} \int_0^{\infty} i(t) dt$$

we get a discrimination per pulse of only

$$\frac{\int_0^{\infty} [i(t)]_{\phi} dt}{\int_0^{\infty} [i(t)]_{\gamma} dt}$$

Given various forms of $v(t)$ out of the detector and cable assembly, we can calculate the total mean square fluctuation voltage. Common forms of the individual pulse shape are:

- a. $v(t) = \frac{Q_f}{C} e^{-\omega_1 t}$
- b. $v(t) = \frac{Q_f}{C} (\omega_1 + \omega_2) t e^{-\omega_3 t}$
- c. $v(t) = \frac{Q_f}{C} e^{-\omega_1 t} (1 - e^{-\omega_2 t})$

Q_f is the total charge collected per pulse and C is the total input capacity of the detector, cable and amplifier input. The corresponding values of $\langle U^2 \rangle - \langle U \rangle^2 = \langle V^2 \rangle$ are

- a. $\langle V^2 \rangle = \bar{N} \frac{Q_f^2}{2\omega_1 C^2}$
- b. $\langle V^2 \rangle = \frac{1}{4} \bar{N} \frac{Q_f^2}{C^2} \frac{(\omega_1 + \omega_2)^2}{\omega_3^3}$
- c. $\langle V^2 \rangle = \bar{N} \frac{Q_f^2}{C^2} \left[\frac{1}{2\omega_1} - \frac{2}{2\omega_1 + \omega_2} + \frac{1}{2(\omega_1 + \omega_2)} \right]$

To simplify the notation, the mean square fluctuation voltage will be denoted $\langle V^2 \rangle$ with the understanding it equals $\langle U^2 \rangle - \langle U \rangle^2$ and is measured by the circuit shown in Figure 2-1.

The mean square fluctuation voltage out of the amplifier (Figure 2-2) is given by

$$\langle V^2 \rangle = \int_0^{\infty} \langle [V(\omega)]^2 \rangle |g(\omega)|^2 d\omega$$

$$\langle [V(\omega)]^2 \rangle = \frac{N}{\pi} F[v(t)] F^*[v(t)]$$

where

$F[v(t)] =$ Fourier transform of $v(t)$

$F^*[v(t)] =$ Complex conjugate of $F[v(t)]$

Assume a pulse

$$v(t) = \frac{Q_f}{C} e^{-\omega_1 t}$$

$$F[v(t)] = \frac{Q_f}{C} \int_0^{\infty} e^{-\omega_1 t} e^{-j\omega t} dt$$

$$= \frac{Q_f}{C} \frac{1}{\omega_1 + j\omega}$$

$$F^*[v(t)] = \frac{Q_f}{C} \frac{1}{\omega_1 - j\omega}$$

$$\langle [V(\omega)]^2 \rangle = \frac{N}{\pi} \frac{Q_f^2}{C^2} \frac{1}{(\omega_1 + j\omega)(\omega_1 - j\omega)}$$

$$= \frac{N}{\pi} \frac{Q_f^2}{C^2} \frac{1}{\omega_1^2 + \omega^2}$$

$$= \frac{N}{\pi} \frac{Q_f^2}{C^2} \frac{T_1^2}{1 + T_1^2 \omega^2}$$

Assume the differentiating and integrating time constants (T_2) of the amplifier are equal. The transfer function of the amplifier is

$$g(\omega) = \frac{j\omega T_2}{(1 + j\omega T_2)^2}$$

$$|g(\omega)|^2 = \frac{T_2^2 \omega^2}{(1 + \omega^2 T_2^2)^2}$$

Hence the total output signal is

$$\begin{aligned} \langle v^2 \rangle &= \int_0^{\infty} \left(\frac{N}{\pi} \frac{Q_f^2}{C^2} \frac{T_1^2}{1 + T_1^2 \omega^2} \right) \left(\frac{T_2^2 \omega^2}{(1 + \omega^2 T_2^2)^2} \right) d\omega \\ &= N \frac{T_1^2 Q_f^2}{\pi C^2} \left[\int_0^{\infty} \frac{T_2^2 \omega^2 d\omega}{(1 + T_1^2 \omega^2)(1 + T_2^2 \omega^2)^2} \right] \\ &= N \frac{T_1^2 Q_f^2}{\pi C^2} \left[\frac{\pi}{4} \frac{T_2}{(T_1 + T_2)^2} \right] \\ &= \frac{N}{4} \frac{Q_f^2}{C^2} \frac{T_1^2 T_2}{(T_1 + T_2)^2} \end{aligned}$$

Other sources add to the total mean square fluctuation voltage at the amplifier input; e. g., thermal, grid current, and shot noise. These are calculated following the derivation of Gillespie (2).

Thermal noise per unit bandwidth is represented by

$$\frac{d\langle v^2 \rangle}{df} = 4 KTR_1$$

where R_1 is the detector load resistor. The transfer function of input circuit for thermal noise is given by

$$g_{\text{input}}(\omega) = \frac{1}{1 + j\omega T_1}$$

$$|g_{\text{input}}(\omega)|^2 = \frac{1}{1 + \omega^2 T_1^2}$$

$\langle v_{th}^2 \rangle$ out of the input circuit is given by

$$\begin{aligned} \frac{d\langle v_{th}^2 \rangle}{df} &= 4KTR_1 |g_{input}(\omega)|^2 \\ &= \frac{4KTR_1}{1 + (\omega T_1)^2} \\ \int_{Tot} d\langle v_{th}^2 \rangle &= \frac{4KTR_1}{2\pi} \int_0^\infty \frac{d\omega}{1 + (\omega T_1)^2} \\ \langle v_{th}^2 \rangle &= \frac{KT}{C_1} \end{aligned}$$

$\langle v_{th}^2 \rangle$ out of the amplifier is given by

$$\begin{aligned} \int_{Tot} d\langle v_{th}^2 \rangle &= \frac{4KTR_1}{2\pi} \int_0^\infty |g_A(\omega)|^2 |g_{th}(\omega)|^2 d\omega \\ &= \frac{4KTR_1}{2\pi} \int_0^\infty \left(\frac{T_2^2 \omega^2}{[1 + (\omega T_2)^2]^2} \right) \left(\frac{1}{1 + (\omega T_1)^2} \right) d\omega \\ &= \frac{KTR_1}{2} \frac{T_2}{(T_1 + T_2)^2} \end{aligned}$$

The shot noise (for a triode) per unit band width is given by

$$\begin{aligned} \frac{d\langle v_S^2 \rangle}{df} &= 4KT \left(\frac{2.5}{gm} \right) \\ &= 4KT (Req) \end{aligned}$$

The mean square voltage out of the amplifier is thus

$$\begin{aligned}
 \langle V_S^2 \rangle &= \frac{4KT \text{Req}}{2\pi} \int_0^{\infty} |g(\omega)|^2 d\omega \\
 &= \frac{2KT \text{Req}}{\pi} \int_0^{\infty} \frac{T_2^2 \omega^2 d\omega}{[1 + (\omega T_2)^2]^2} \\
 &= \frac{KT \text{Req}}{2T_2}
 \end{aligned}$$

The grid current noise per unit band width is

$$\frac{d \langle V_g^2 \rangle}{df} = 2e (\sum I_g) \frac{R_1^2}{1 + \omega^2 T_1^2}$$

Hence the mean square voltage out of the amplifier is

$$\begin{aligned}
 \langle V_g^2 \rangle &= \frac{2e(\sum I_g) R_1^2}{2\pi} \int_0^{\infty} \frac{|g(\omega)|^2 d\omega}{1 + \omega^2 T_1^2} \\
 &= \frac{e(\sum I_g) R_1^2}{\pi} \left[\int_0^{\infty} \left(\frac{1}{1 + \omega^2 T_1^2} \right) \left(\frac{\omega^2 T_2^2}{(1 + \omega^2 T_2^2)^2} \right) d\omega \right] \\
 &= \frac{e(\sum I_g) R_1^2}{\pi} \left[\frac{\pi T_2}{4(T_1 + T_2)^2} \right] \\
 &= \frac{e(\sum I_g) R_1^2}{4} \frac{T_2}{(T_1 + T_2)^2}
 \end{aligned}$$

The spectral distribution of mean square fluctuation voltage depends upon electron and positive ion collection, which in turn depend on the gas used, the gas pressure, the neutron flux level, applied voltage, and system bandwidth. It is important to recognize how variations in these parameters affect spectral distribution and hence output signal. The spectral distribution $V(s)$ is the LaPlace transform of $v(t)$:

$$V(s) = \int_0^{\infty} v(t) e^{-st} dt$$

An ion chamber pulse may be assumed of the shape

$$v(t) = (\omega_1 + \omega_2) t e^{-\omega_3 t}$$

where $\omega_1 t$ and $\omega_2 t$ represent linear voltage rise due to electron and positive ion collection, and $e^{-\omega_3 t}$ is the decay factor of the system.

$$\begin{aligned} \text{Thus } V(s) &= (\omega_1 + \omega_2) \int_0^{\infty} t e^{-\omega_3 t} e^{-st} dt \\ &= \frac{\omega_1 + \omega_2}{(s + \omega_3)^2} \end{aligned}$$

The spectral distribution thus depends upon electron and positive ion collection times $\left(\frac{1}{\omega_1}, \frac{1}{\omega_2}\right)$, which in turn depend upon the applied voltage across the chamber. If we make the amplifier rise and decay times $\left(\frac{1}{\omega_4}, \frac{1}{\omega_5}\right)$ long compared to positive ion collection time out pulse shape may be represented as:

$$\begin{aligned} v(t) &= e^{-\omega_5 t} (1 - e^{-\omega_4 t}) \\ V(s) &= \int_0^{\infty} e^{-\omega_5 t} (1 - e^{-\omega_4 t}) e^{-st} dt \\ &= \frac{1}{s + \omega_5} \left(1 - \frac{1}{1 + \frac{\omega_4}{s + \omega_5}} \right) \end{aligned}$$

Here, spectral dependence is independent of electron and positive ion collection times and hence independent of applied voltage across the chamber and depends only on the system bandwidth.

This spectral dependence has been demonstrated experimentally and the results are described in GEAP-4304, p. 101f. Essentially, however, for the 0.5 - 13.6 kc amplifier used throughout this study, the same shapes of saturation curves were obtained in the RMS voltage and d-c current modes of operation. Even for the worst bandwidths, the shape of the saturation curve is not severe and with a stable polarizing voltage supply, measurement errors are small.

For any chamber, it is desirable to define a set of numbers such that by simple multiplication one can obtain the signals developed for any combination neutron flux, gamma dose rate, and noise, to ascertain whether other sources of signals are significant in comparison to that caused by the neutron flux. For the d-c mode of operation, this is done by three equations

$$\begin{aligned}\bar{i}_\phi &= S_\phi \phi \\ \bar{i}_\gamma &= S_\gamma \gamma \\ \bar{i}_L &= \frac{V_p}{R_L}\end{aligned}$$

Analogously, we can define three equations for the RMS voltage mode of operation.

$$\begin{aligned}\sqrt{\langle V_\phi^2 \rangle} &= S_\phi \sqrt{V_\phi} \\ \sqrt{\langle V_\gamma^2 \rangle} &= S_\gamma \sqrt{V_\gamma} \\ \sqrt{\langle V_N^2 \rangle} &= N\end{aligned}$$

One point must be emphasized. For the RMS voltage mode, sensitivities depend on system bandwidth, i. e., the bandwidth of the particular amplifier used. Gamma and thermal neutron sensitivities are shown for a short, fully enriched chamber for various gases, gas pressures, and amplifier bandwidths and gains in Figure 2-3. System noise figures are also given. With these sets of numbers, the designer can ascertain the signals developed for any application.

Plots of RMS voltage vs. neutron flux are shown in Figures 2-4 through 2-10. These plots show that depending on the chamber, gas, gas pressure, and amplifier used, it is possible with an in-core ion chamber to measure down to $10^6 - 10^7$ nv operating in the RMS voltage mode. (On the basis of d-c sensitivities, it is apparent this is not possible in the d-c mode.) The upper

limit of these experiments was 6×10^{11} nv since this was the maximum thermal neutron flux attainable at NTR. These chambers can go to higher fluxes if the amplifier gain is reduced so that it is not saturated and the upper limit is limited only by saturation of the ion chamber. Ion chambers of the type used with 1 atmosphere of argon can saturate below 200 volts up to a thermal neutron flux of 5×10^{13} nv. A comparison between the low limit of neutron flux measurable with the same chamber using RMS voltage and d-c current measurements is shown in Figure 2-11.

For completeness it should be noted that higher power signals can be measured with a corresponding increase of gamma discrimination. These have not been investigated in detail during this study since greater gamma discrimination than can be achieved with mean square measurements is not required. Assuming that the amplifier determines the pulse shape i.e., the rise time is determined by the circuit rather than charge collection in the chamber (which condition is easily met and which has been met with the 0.5 - 13.6 kc up to 2.36 atmospheres of argon), the relative outputs of pulses $A = 1$ to $A = N$ are represented for the d-c case by

$$\langle W \rangle = K_0 \sum_{A=1}^N r_A Q_A$$

where

| | |
|---------------------|---------------------------------------|
| $\langle W \rangle$ | is average current |
| K_0 | is constant |
| r_A | is average rate of pulse A occurrence |
| Q_A | is charge for pulse A |

The mean square fluctuation voltage is

$$\langle W^2 \rangle - \langle W \rangle^2 = K_1 \sum_{A=1}^N r_A Q_A^2$$

The higher power signals can be shown to be (3)

$$\begin{aligned} \langle W^3 \rangle - 3\langle W^2 \rangle \langle W \rangle + 2\langle W \rangle^3 &= K_2 \sum r_A Q_A^3 \\ \langle W^4 \rangle - 4\langle W^3 \rangle \langle W \rangle - 3\langle W^2 \rangle^2 + 12\langle W^2 \rangle \langle W \rangle^2 - 6\langle W \rangle^4 \\ &= K_3 \sum r_A Q_A^4 \end{aligned}$$

$$\begin{aligned} \langle W^5 \rangle &= 5 \langle W^4 \rangle \langle W \rangle - 10 \langle W^3 \rangle \langle W^2 \rangle + 20 \langle W^3 \rangle \langle W \rangle^2 \\ &+ 30 \langle W^2 \rangle^2 \langle W \rangle - 60 \langle W^2 \rangle \langle W^3 \rangle + 24 \langle W \rangle^5 \\ &= K_4 \sum r_A Q_A^5 \end{aligned}$$

It is noted that if $\langle W \rangle = 0$, $\langle W^3 \rangle = K_2 \sum r_A Q_A^3$

However, for $\langle W \rangle = 0$, the higher powers do not simplify to simply $\langle W^n \rangle$.

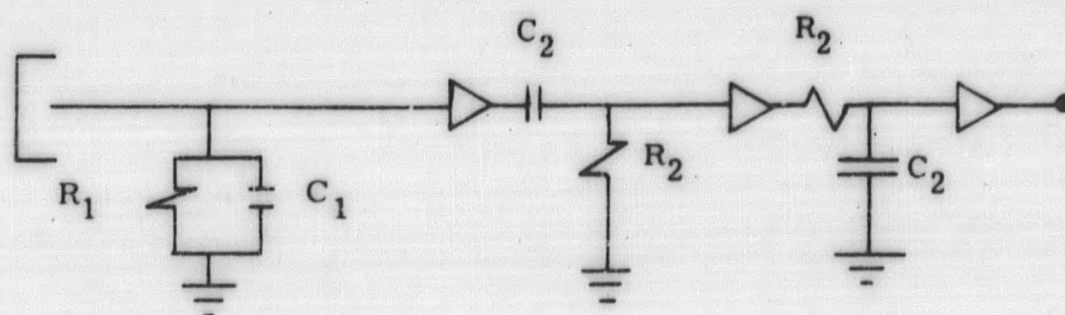
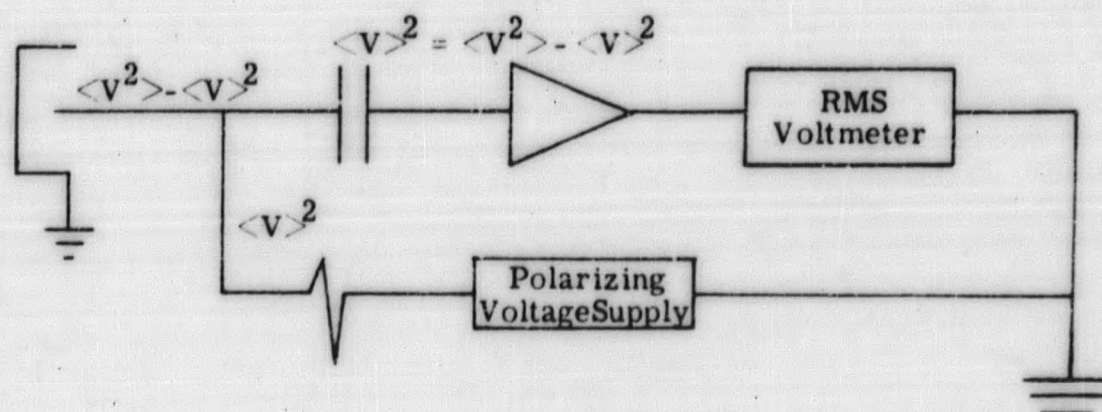


Figure 2-2. Detector - Amplifier Equivalent Circuit

| Chamber | Gas | Pressure | RMS | | | | | DC | | |
|----------------|------|------------|------------|------|-------------------------------------|-----------------------------------------|------------------------|------------------------|------------------------|--------------------|
| | | | BW (KC) | Gain | S_{ϕ} ($\mu v/\sqrt{nv}$) | S_{γ} ($\mu v/\sqrt{R/hr}$) | N (mv) | S_{ϕ} (a/nv) | S_{γ} | R_L^* (700 F) |
| Short fully | A | 0.84 | 0.86 - 165 | 115 | 3.24 | <10 | 5 | 4.16×10^{-17} | 1.83×10^{-14} | 10^9 |
| | A | 0.84 | 0.5 - 52 | 90 | 3.24 | <10 | 3 | | | |
| | A | 0.84 | 0.5 - 13.6 | 72 | 2.75 | <10 | 3 | | | |
| | A | 0.84 | 2.4 - 100 | 90 | 2.50 | <10 | 2 | | | |
| | A | 0.84 | 15 - 220 | 75 | 1.00 | <10 | 4 | | | |
| | A | 0.84 | 0.4 - 2.7 | 2 | 0.085 | <10 | 0.7 | | | |
| | A | 1.34 | 0.5 - 52 | 90 | 5.75 | <10 | 3 | 8.18×10^{-17} | 3.65×10^{-14} | 10^9 |
| | A | 1.34 | 0.86 - 165 | 115 | 5.75 | <10 | 5 | | | |
| | A | 1.34 | 0.5 - 13.6 | 72 | 4.5 | <10 | 3 | | | |
| | A | 1.34 | 2.4 - 100 | 90 | 4.5 | <10 | 2 | | | |
| | A | 1.34 | 15 - 220 | 75 | 1.88 | <10 | 4 | | | |
| | A | 1.34 | 0.4 - 2.7 | 2 | 0.145 | <10 | 0.7 | | | |
| | A | 2.36 | 0.5 - 52 | 90 | 7.5 | <10 | 3 | 14.2×10^{-17} | 6.3×10^{-14} | 10^9 |
| | A | 2.36 | 0.86 - 165 | 115 | 7.5 | <10 | 5 | | | |
| | A | 2.36 | 0.5 - 13.6 | 72 | 6.25 | <10 | 3 | | | |
| | A | 2.36 | 2.4 - 100 | 90 | 6.25 | <10 | 2 | | | |
| | A | 2.36 | 15 - 220 | 75 | 2.75 | <10 | 4 | | | |
| | A | 2.36 | 0.4 - 2.7 | 2 | 0.20 | <10 | 0.7 | | | |
| | He | 0.84 | 0.5 - 13.6 | 72 | 0.53 | <10 | 9 | 0.87×10^{-17} | 0.89×10^{-14} | 10^9 |
| | He | 1.34 | 0.5 - 13.6 | 72 | 1.02 | <10 | 9 | 1.67×10^{-17} | 1.01×10^{-14} | 10^9 |
| | He | 2.36 | 0.5 - 13.6 | 72 | 1.88 | <10 | 9 | 3.0×10^{-17} | 1.42×10^{-14} | 10^9 |
| N ₂ | 0.84 | 0.5 - 13.6 | 72 | 2.12 | <10 | 9 | 3×10^{-17} | 1.32×10^{-14} | 10^9 | |
| N ₂ | 1.34 | 0.5 - 13.6 | 72 | 3.68 | <10 | 9 | 6.18×10^{-17} | 2.55×10^{-14} | 10^9 | |
| N ₂ | 2.36 | 0.5 - 13.6 | 72 | 5.30 | <10 | 9 | 9.5×10^{-17} | 4.77×10^{-14} | 10^9 | |

*35 feet M/I cable.

Figure 2-3 RMS and D-C Sensitivities for Short Fully Enriched Ion Chamber

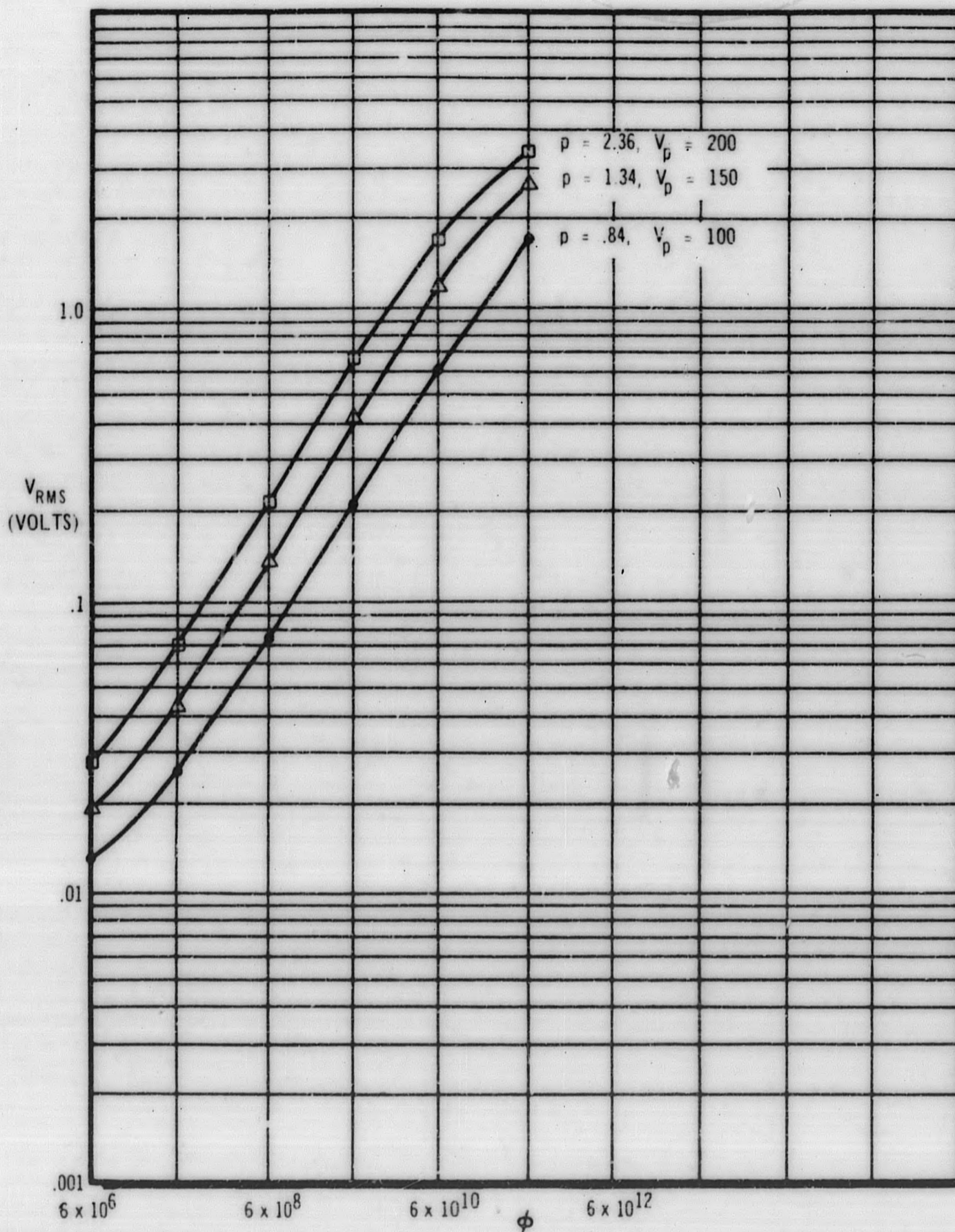


Figure 2-4. RMS Voltage vs. Neutron Flux Short Fully Enriched Ion Chamber, Amplifier Bandwidth 0.5 - 13.6 KC, Gain of 72

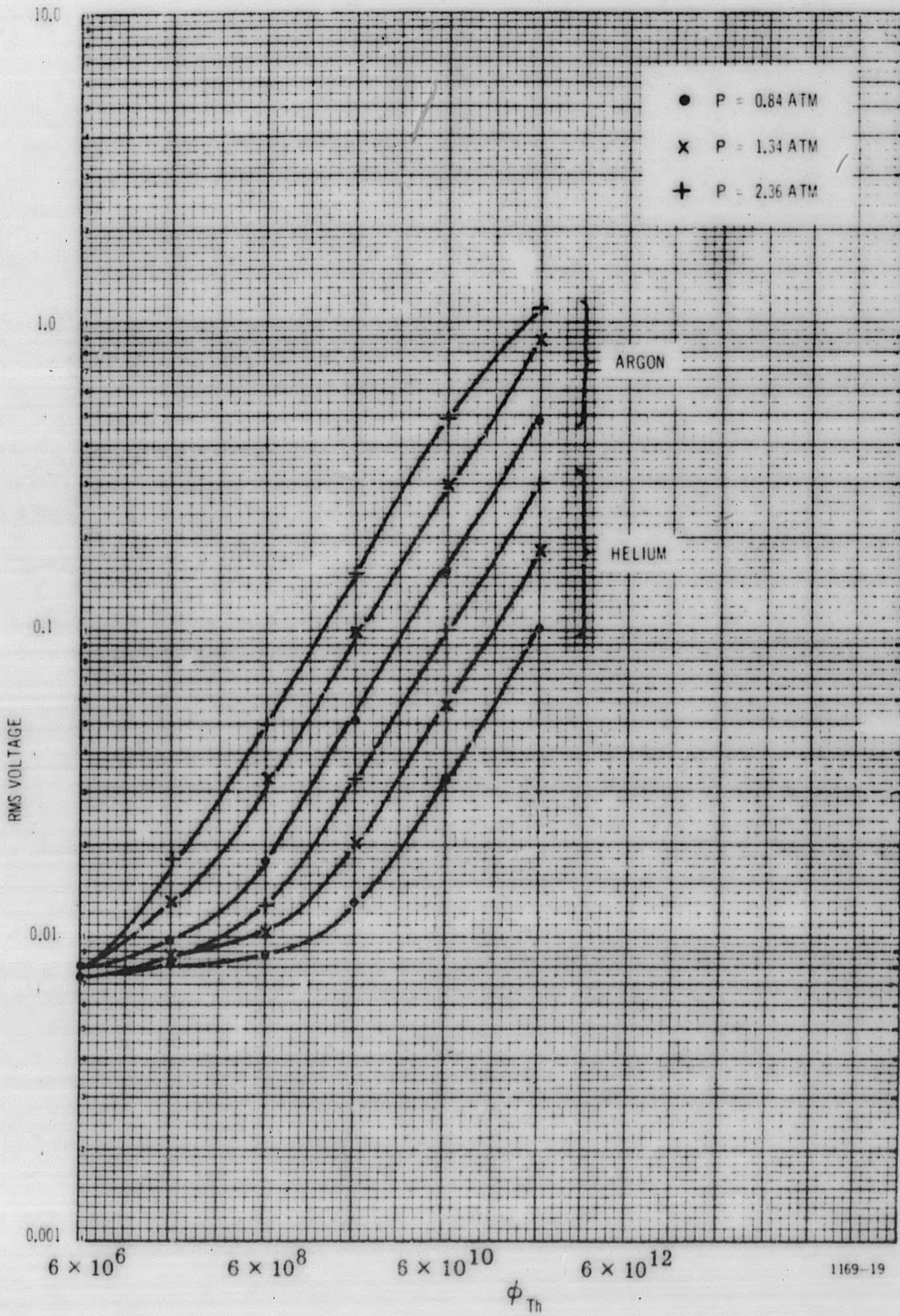


Figure 2-5. RMS Voltage vs. Neutron Flux Long Fully Enriched Ion Chamber, Bandwidth 0.63 - 228 KC, Gain 100

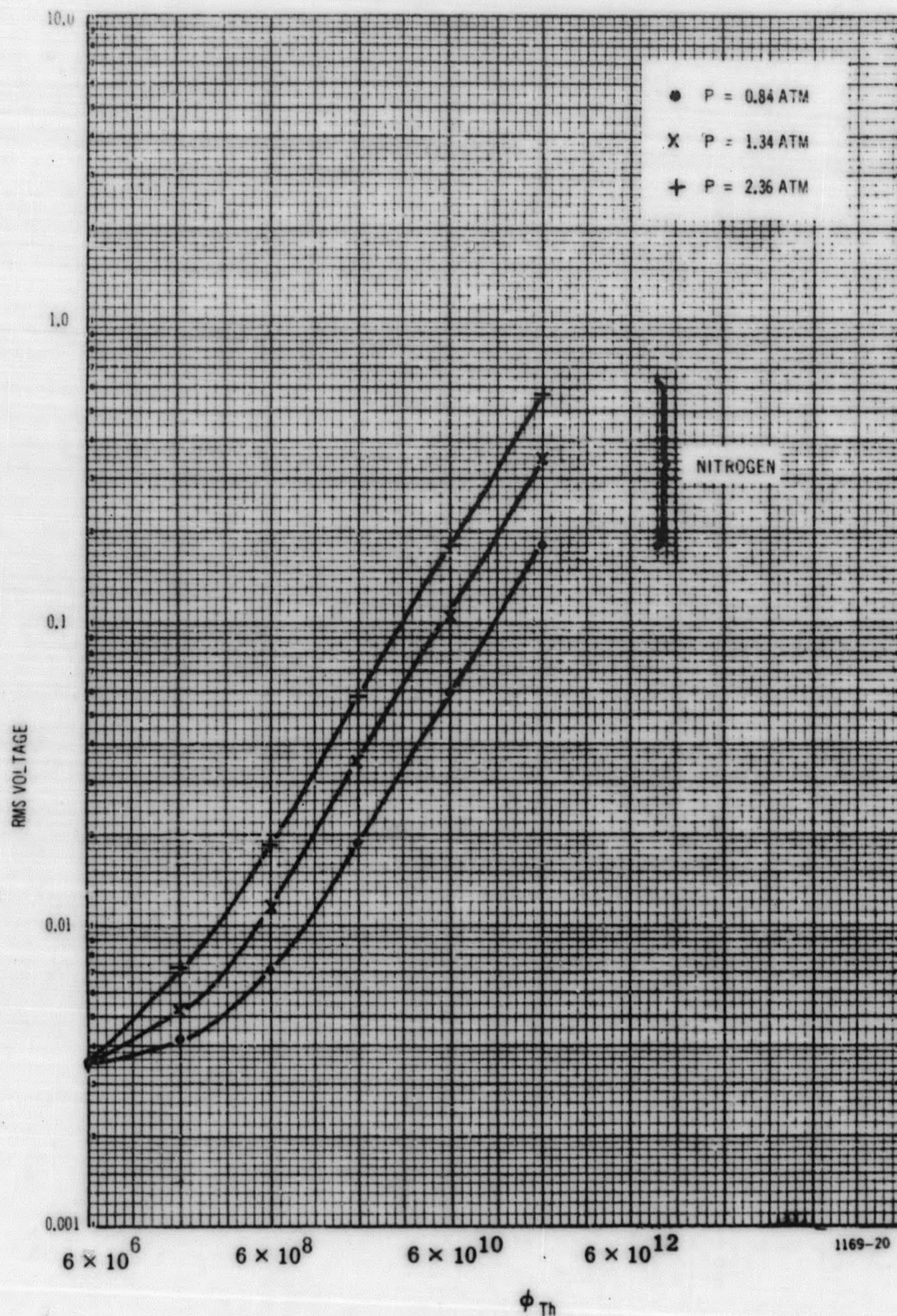


Figure 2-6. RMS Voltage vs. Neutron Flux Long Fully Enriched Ion Chamber, Bandwidth 0.63 - 228 KC, Gain 100

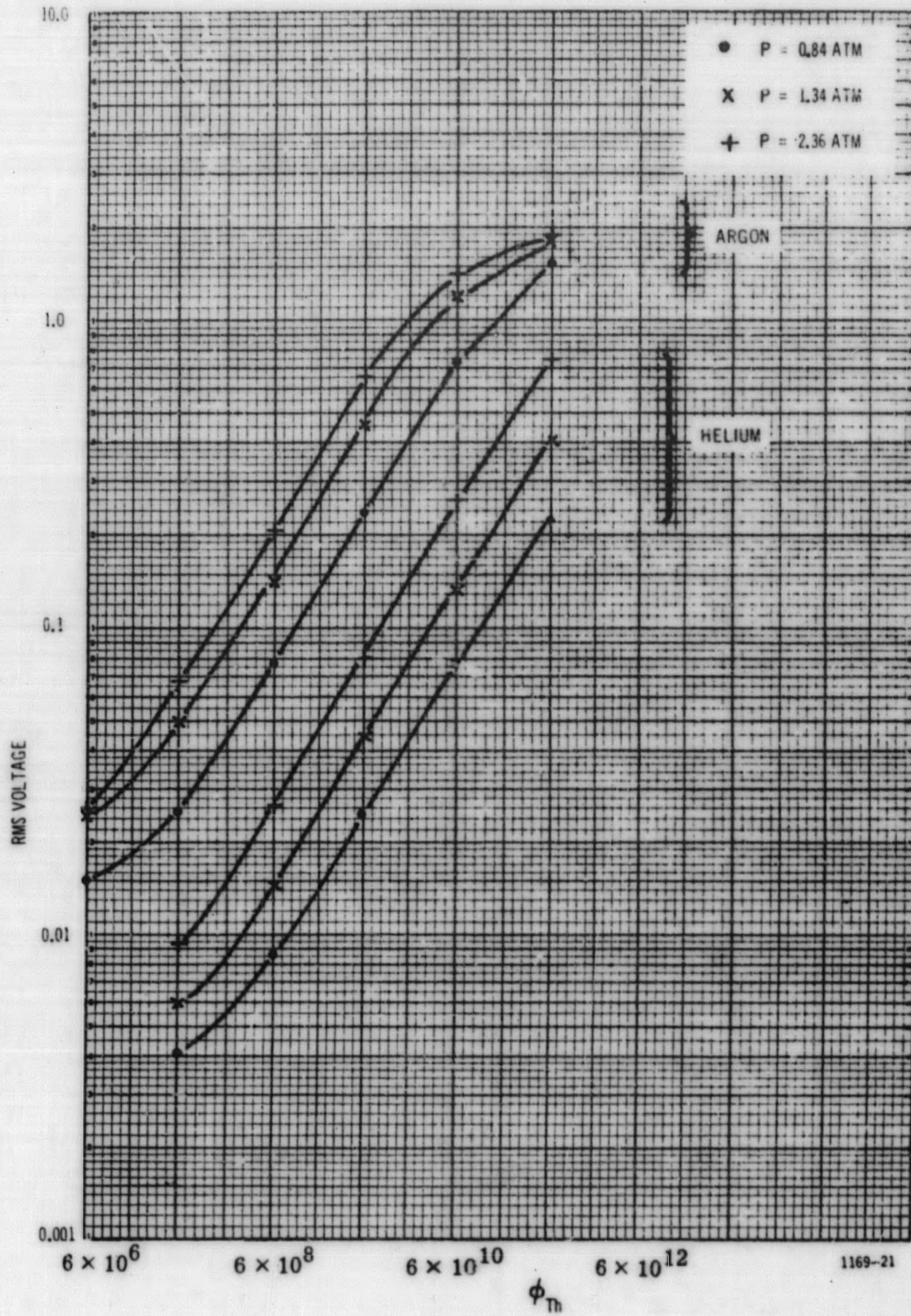


Figure 2-7. RMS Voltage vs. Neutron Flux Short Fully Enriched Ion Chamber, Bandwidth 0.63 - 228 KC, Gain 100

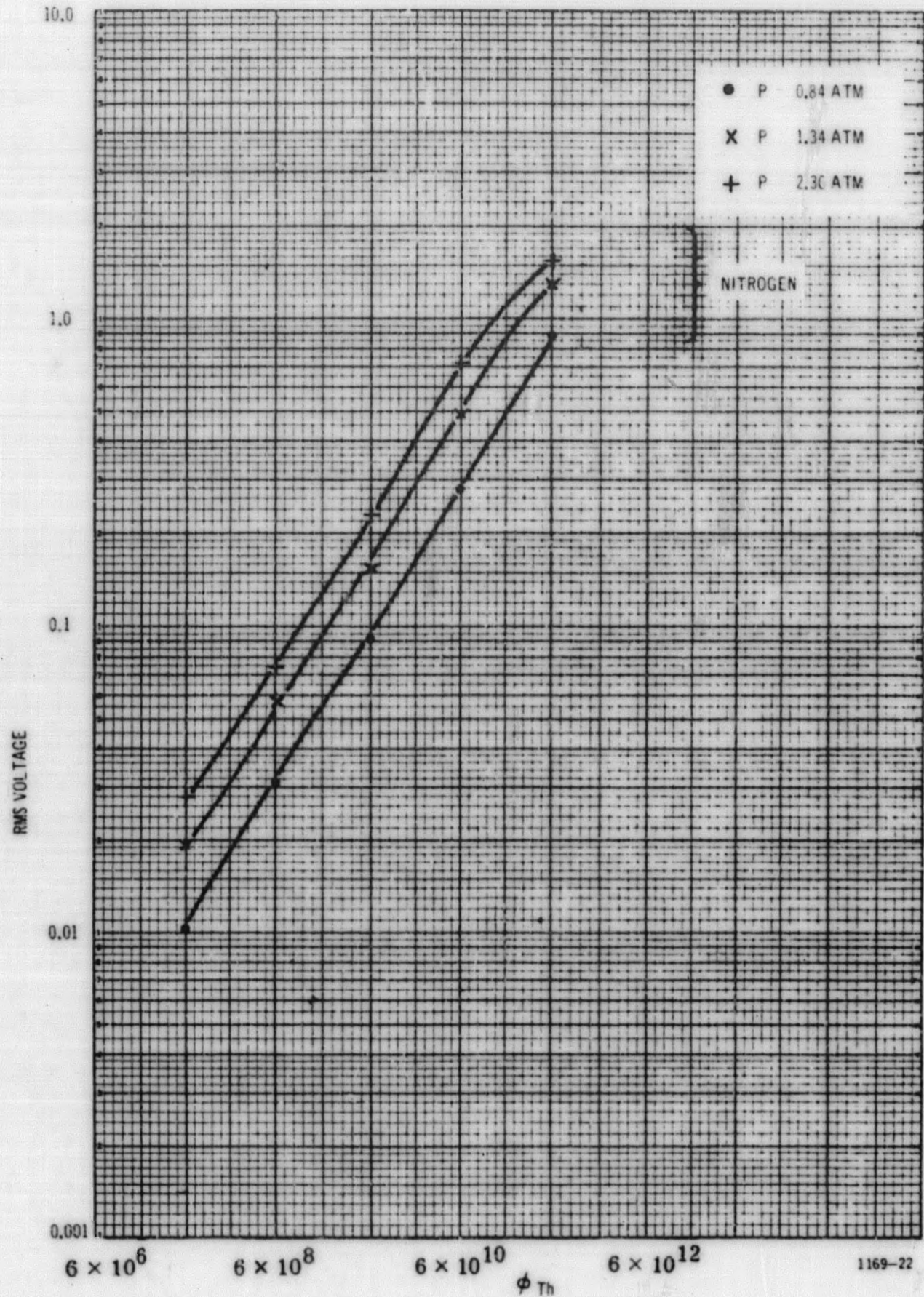


Figure 2-8. RMS Voltage vs. Neutron Flux. Short Fully Enriched Ion Chamber, Bandwidth 0.63 - 228 KC, Gain 100

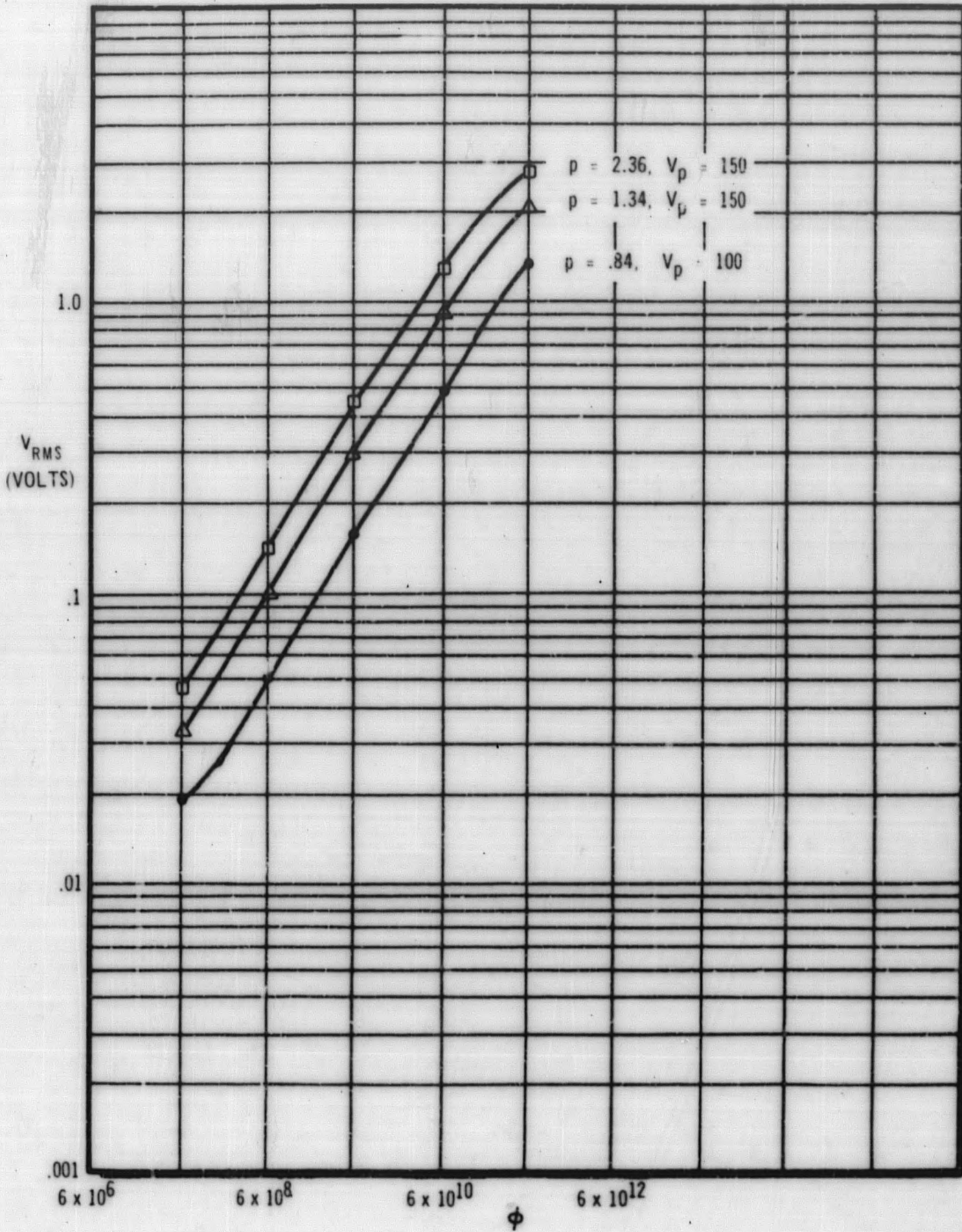


Figure 2-9. RMS Voltage vs Neutron Flux, Short Fully Enriched Ion Chamber with N_2 , Amplifier Bandwidth of 0.5 - 13.6 KC, Gain of 72

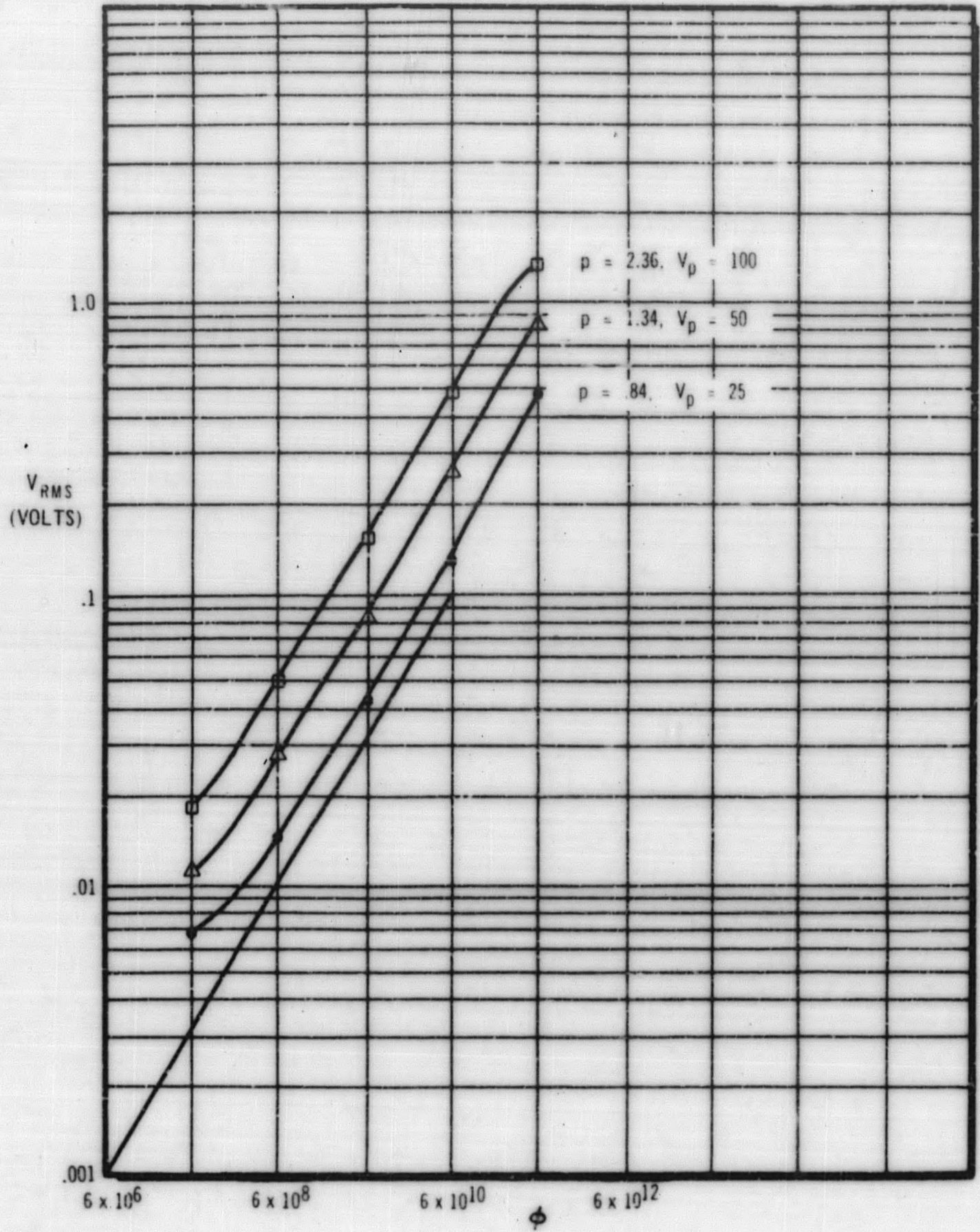


Figure 2-10. RMS Voltage vs Neutron Flux. Short Fully Enriched Ion Chamber with He, Amplifier Bandwidth 0.5 - 13.6 KC, Gain of 72

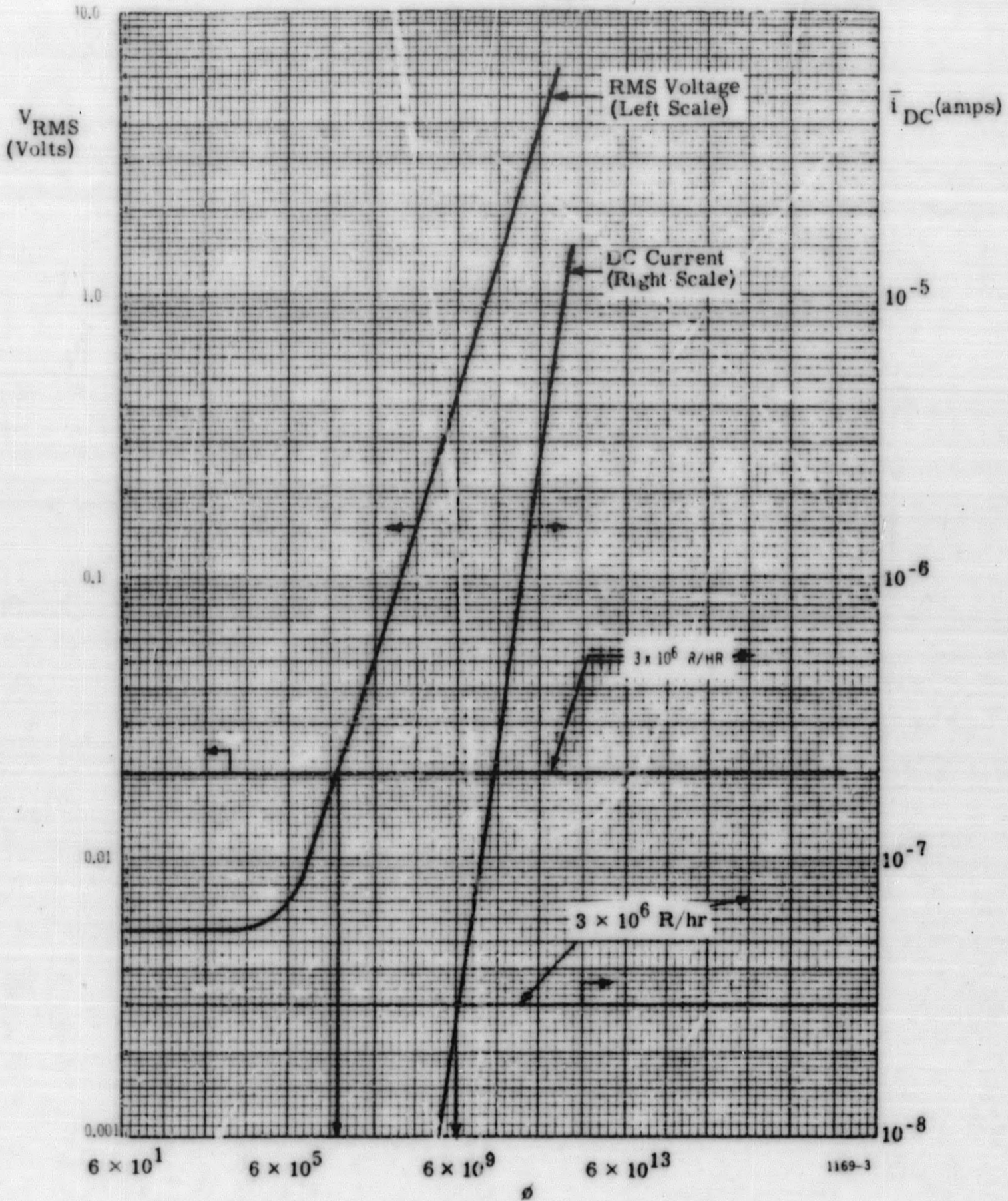


Figure 2-11. RMS Voltage and DC Current Neutron Flux for Argon. P = 2.36 ATM, in a Short Fully Enriched Chamber

SECTION III

COUNTING WITH IN-CORE ION CHAMBERS

The RMS voltage mode of operation can measure neutron fluxes down to the point where system noise RMS voltage interferes with neutron caused RMS voltage. For the type of systems used, this begins to be a problem in the $10^6 - 10^7$ nv region. In order to measure lower neutron fluxes, the chambers must be operated in the counting mode.

The first problem with using in-core ion chambers in the counting mode in large power reactors is caused by the distance required between the ion chamber and the preamplifier. Assuming a chamber and cable assembly not terminated in its characteristic impedance, the pulse from a fission fragment at the amplifier input can be represented by

$$v(t) = \frac{q_f}{C} e^{-\omega_1 t}$$

With long cables, C becomes large and hence $v(t)$ small. The problem then is simply to maximize q_f and minimize C.

A number of calculations may prove useful to determine the maximum charge which can be developed by a fission fragment ionizing a gas. At fission, two major fission fragments are generated with most probable energies of 97 and 65 mev. For gases, the average energy required to form an ion-electron pair is 30 ev although it varies from 22 ev for Kr to 41 ev for He. Assuming 30 ev per electron-ion pair we can at most generate 3.2×10^6 ion-electron pairs (6.1×10^{-13} coulombs). This amounts to 0.97 mv for the short fully enriched ion chamber with 7-foot Al_2O_3 insulated cable ($6.3 \times 10^{-10} f$). Since most fission fragments will have lost some energy before entering the gas, the average pulse will be smaller.

The range of the two fission fragments in argon at 1 atmosphere pressure is 2.6 cm for the light and 1.9 cm for the heavy or about 0.26 cm and 0.19 cm at 10 atmospheres. The short fully enriched ion chamber has a gap of 0.05 cm and sensitive length of 2.5 cm. Hence there are some fission fragments which do not expend all of the energy available in ionizing the gas at 10 atmospheres. Fission fragments formed at the surface and traveling in a normal direction from the chamber wall do not form as many ion-electron pairs as is theoretically possible. Most fission fragments, however, do form as many electron-ion pairs as is theoretically possible at this pressure.

To maximize the electron-ion pair formation, a gas must be chosen with the lowest average energy to ionize. As long as the fission fragments are being totally stopped, it is not necessary to choose a gas on the basis of specific ionization. There are considerable discrepancies in the literature on the average energy to ionize values (w). Jesse and Sadauskis^(1,2) have shown that small impurities in helium drastically affect this value. They added 0.13 percent argon to the purest helium used and this changed w from 41.3 ev to 29.7 ev. The results of these experiments are shown in Figure 3-1. The reason for this can be explained by Figure 3-2. Argon has an ionization potential of 15.7 ev compared to helium which has an ionization potential of 24.5 ev and an excitation potential of 19.77 ev. Hence the more efficient conversion of energy to ion-electron pairs with argon present. At best, of course, in argon-helium mixtures is the conversion efficiency of pure argon. Hence, the best gas from the point of view of the conversion of energy to charge, is the gas with the lowest w . These values are shown in Figure 3-2.

A second consideration relative to choice of gas is the recombination coefficient. Again there exists a considerable number of discrepancies in the literature. The theoretical model of Yaffe of ion-electron pairs formed columnly with a radial density given by a Gaussian distribution at time zero which subsequently both diffuse and drift across an electric field is conceptually helpful but does not permit accurate calculations to be made.

Trace impurities can significantly affect recombination. Ultrapure noble gases have been used at very high pressures with no recombination^(3,4). Since the ion chamber is to be used in a reactor core for substantial periods of time, fission gases will build up in the chamber. This will amount almost totally to Xe and Kr buildup. However, since this effect cannot be analytically predicted with confidence, this approach will be pursued only as a last resort.

Facchini and Malvicini⁽⁵⁾ have reported the addition of N_2 to argon reduces recombination caused by traces of oxygen. This is attributed to the large attachment cross section of oxygen at higher electron energies (i. e., in pure argon) and the lower cross section at lower electron energies (i. e., in a mixture of argon and nitrogen) for the particular geometry and applied voltages in their chamber. Ion and electron mobilities for various gases are shown in Figure 3-3.

Selection of pulse width for a particular set of values for gas, gas pressure, and applied voltage must also be considered. Here some balance must be achieved between obtaining maximum pulse

height (i. e. , a pulse sufficiently long to collect all charges) and capability of fast counting (i. e. , a short pulse). The charge collection time of course depends on the gas used, pressure, applied voltage, and gap in the chamber. Mobilities of various gases are given in Figure 3-3 and from these collection times can be computed knowing the gap pressure and applied voltage.

Experiments have been conducted utilizing xenon, argon, neon, and krypton as fill gases at various pressures with an applied voltage of 275 volts and a pulse width of about 4 microseconds with a short, fully enriched ion chamber. The block diagram of the experiment is shown in Figure 3-4. Gases are of the highest purity available and no effort was made to further purify. Before each experiment the chamber was evacuated to less than 30 microns and flushed at least three times with the gas to be used. During some experiments considerably more flushing was required to eliminate oxygen and water vapor. Failure to eliminate these impurities resulted in obvious loss of pulse height. This is shown by comparing the pulse spectra of the short fully enriched ion chamber with 60 and 125 psig of argon properly flushed (Figures 3-5 and 3-6) to the spectra at 60 and 125 psig of argon improperly flushed (Figures 3-8 and 3-9).

Pulse height spectra versus applied voltage are shown for the short fully enriched ion chamber with argon at 5 psig (Figures 3-10 through 3-13), 10 psig (Figures 3-14 through 3-17), 20 psig (Figures 3-18 through 3-21), 40 psig (Figures 3-22 through 3-26), 60 psig (Figures 3-27 through 3-31), and 125 psig (Figures 3-32 through 3-37). Pulse height spectrum changes with applied voltage are due to the pulse width chosen (about 4 microseconds). The positive ion collection time is considerably longer than this, and hence as voltage is increased, more and more positive ions can be collected during the 4 microseconds. At 125 psig recombination offsets this effect. It should thus be remembered that when the pulse is clipped off while the positive ions are being collected, that if the noise level is higher than some of the smaller neutron pulses, that for a given discriminator setting, count rate will depend on voltage. As long as the neutron pulses are larger than noise and the discriminator is set below the neutron pulses, then spectrum shifts with applied voltage will not affect count rates.

Pulse spectra changes with pressure using the short, fully enriched ion chambers are shown for argon (Figures 3-5 through 3-37), krypton (Figures 3-38 through 3-43), neon (Figures 3-44 through 3-50) and xenon (Figures 3-51 through 3-54). The spectrum shifts due to increased pressure of course are simply caused by the fact that a greater portion of the fission fragment energy is expended in the gas at higher pressures than at lower pressures. For most fragments at 10 atmospheres (126 psig), all of the energy is expended and increase in pressure will yield no greater pulse height and indeed charges begin to recombine resulting in a loss of pulse height.

The conclusions can be drawn that for this chamber operating in a thermal neutron flux of 6.38×10^4 nv, that all these gases provide good pulse spectrums at about 125 psig. At lower pressures the fission fragments are not totally stopped, and at higher pressures recombination begins.

The chamber and cable capacity is governed chiefly by the cable from the chamber to the preamplifier. The lowest capacity cable for use outside the reactor core found was RG114 with 6.5 pf/ft. Inside the core ceramic insulation is required to protect against radiation damage. The lowest capacity found was quartz fiber with a capacity of 30 pf/ft.

Average Energy to Ionize (W)

| <u>Gas</u> | <u>Reference 1</u> | <u>Reference 2</u> | <u>Reference 3</u> | <u>Reference 4</u> | <u>Reference 5</u> |
|--------------|--------------------|--------------------|--------------------|--------------------|--------------------|
| He | 41.3 | -- | 31.7 | 30.86 | 42.7 |
| He + 0.13% A | 29.7 | -- | -- | -- | -- |
| Ne | 36.3 | -- | -- | -- | 36.8 |
| Ne + 0.12% A | 26.1 | -- | -- | -- | -- |
| A | 26.4 | 26.3 | 25.9 | 26.25 | 26.4 |
| Kr | 24.1 | -- | -- | -- | 24.1 |
| Xe | 21.9 | -- | -- | -- | 21.9 |

- Reference 1: Jesse and Sadauskis, Phys. Rev. 88, 417
- Reference 2: Sharpe, J., Proc. Phys. Soc. London A65, 859 (1952)
- Reference 3: Valentine, J. M. and Curran, S. C., Phil. Mag. 43, 964 (1952)
- Reference 4: Haeberli, Huber and Boldinger, Helv. Phys. Acta 25, 467 (1952)
- Reference 5: Jesse and Sadauskis, Phys. Rev. 90, 1120

Figure 3-1

Ionization and Excitation Potentials

| <u>Gas</u> | <u>E_{-excite}</u> | <u>E_{-ionize}</u> | <u>E/Ion Pair (W)</u> |
|------------|----------------------------|----------------------------|-----------------------|
| A | 11.57 | 15.7 | 26 |
| Ne | 16.6 | 21.5 | 28 |
| He | 19.77 | 24.5 | 30 |
| Kr | 9.98 | 13.94 | 22 |
| Xe | 8.39 | 12.08 | -- |

Sharpe, J., Nuclear Radiation Detectors, p. 58 (1958)

Figure 3-2

ELECTRON + POSITIVE ION MOBILITIES,
VELOCITIES + COLLECTION TIMES

| Gas | μ_e ($\frac{\text{Cm}^2, \text{ mm Hg}}{\text{Volt} \cdot \text{Sec}}$) | V_e ($\frac{\text{Cm}}{\text{Sec}}$) | t_e sec | μ_{I+} | V_{I+} | t_{I+} |
|----------------|----------------------------------------------------------------------------------|---------------------------------------------|-----------------------|--------------------|--------------------|-----------------------|
| N ₂ | 0.58×10^6 | 1.5×10^6 | 3.33×10^{-8} | 0.98×10^3 | 2.6×10^3 | 1.92×10^{-5} |
| He | 0.65×10^6 | 1.7×10^6 | 2.94×10^{-8} | 7.6×10^3 | 19.7×10^3 | 0.24×10^{-5} |
| A | 0.31×10^6 | 0.8×10^6 | 6.25×10^{-8} | 1.04×10^3 | 2.6×10^3 | 1.92×10^{-5} |
| H ₂ | 0.58×10^6 | 1.5×10^6 | 3.33×10^{-8} | 4.30×10^3 | 11.2×10^3 | 0.44×10^{-5} |
| O ₂ | 1.15×10^6 | 3.0×10^6 | 1.67×10^{-8} | — | — | — |
| Air | 0.77×10^6 | 2.0×10^6 | 2.50×10^{-8} | 1.07×10^3 | 2.6×10^3 | 1.92×10^{-5} |
| Ne | 1.15×10^6 | 3.0×10^6 | 1.67×10^{-8} | — | — | — |

Assume $V_p = 100$ volts, gap = 0.05 cm, $p = 1$ ATM

V_e Taken from American Institute of Physics Handbook, p 7-205 ff (1957).

μ_e, t_e Calculated from V_e

μ_{I+} (Except He) taken from Price, W. J., Nuclear Radiation Detection, p. 69 (1958).

μ_{I+} (He) taken from Sharpe, J., Nuclear Radiation Detectors, p. 57 (1955).

V_{I+}, t_{I+} Calculated from μ_{I+}

Figure 3-3.

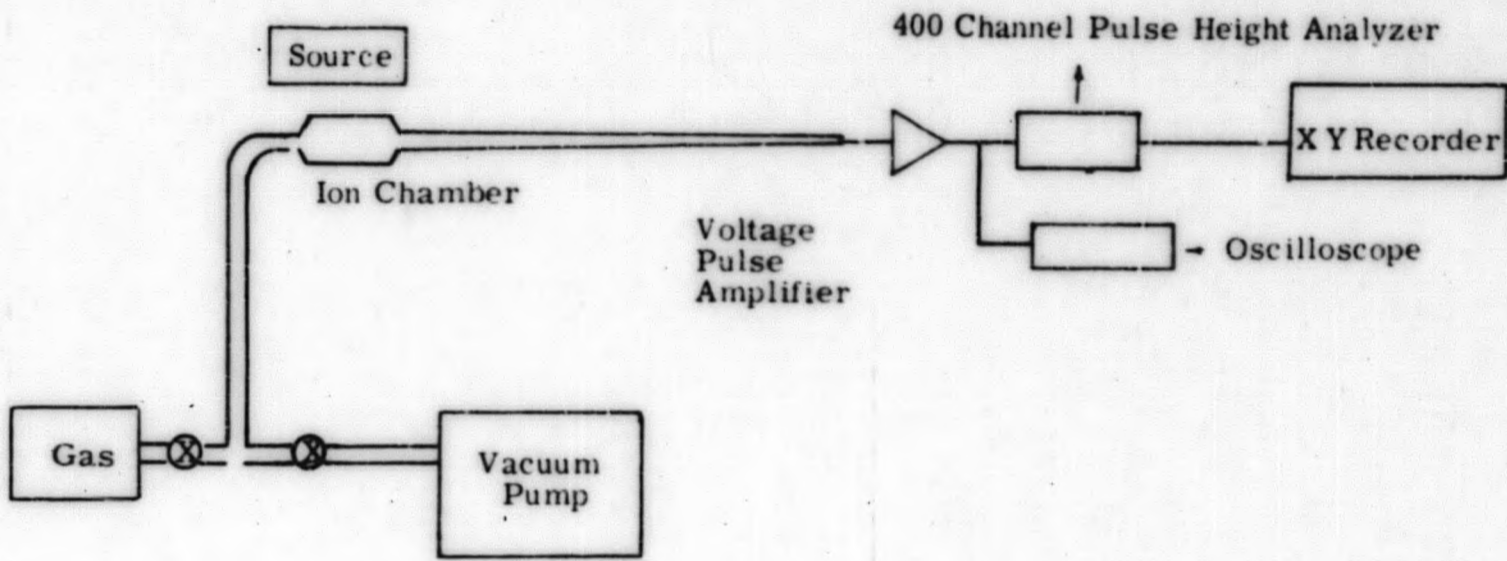


Figure 3-4. Counting Experiments, Block Diagram

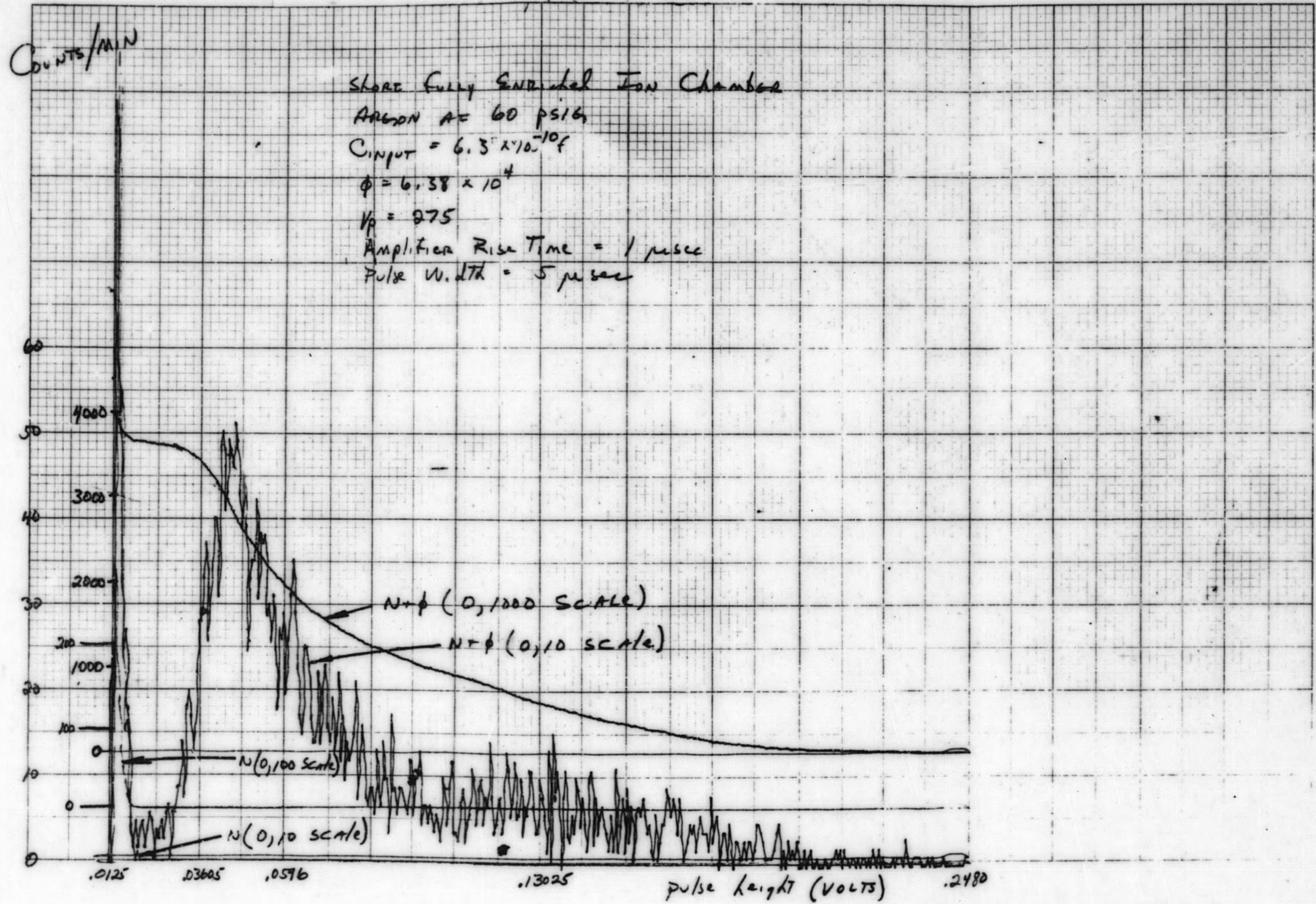


Figure 3-5. Differential and Integral Bias Curves

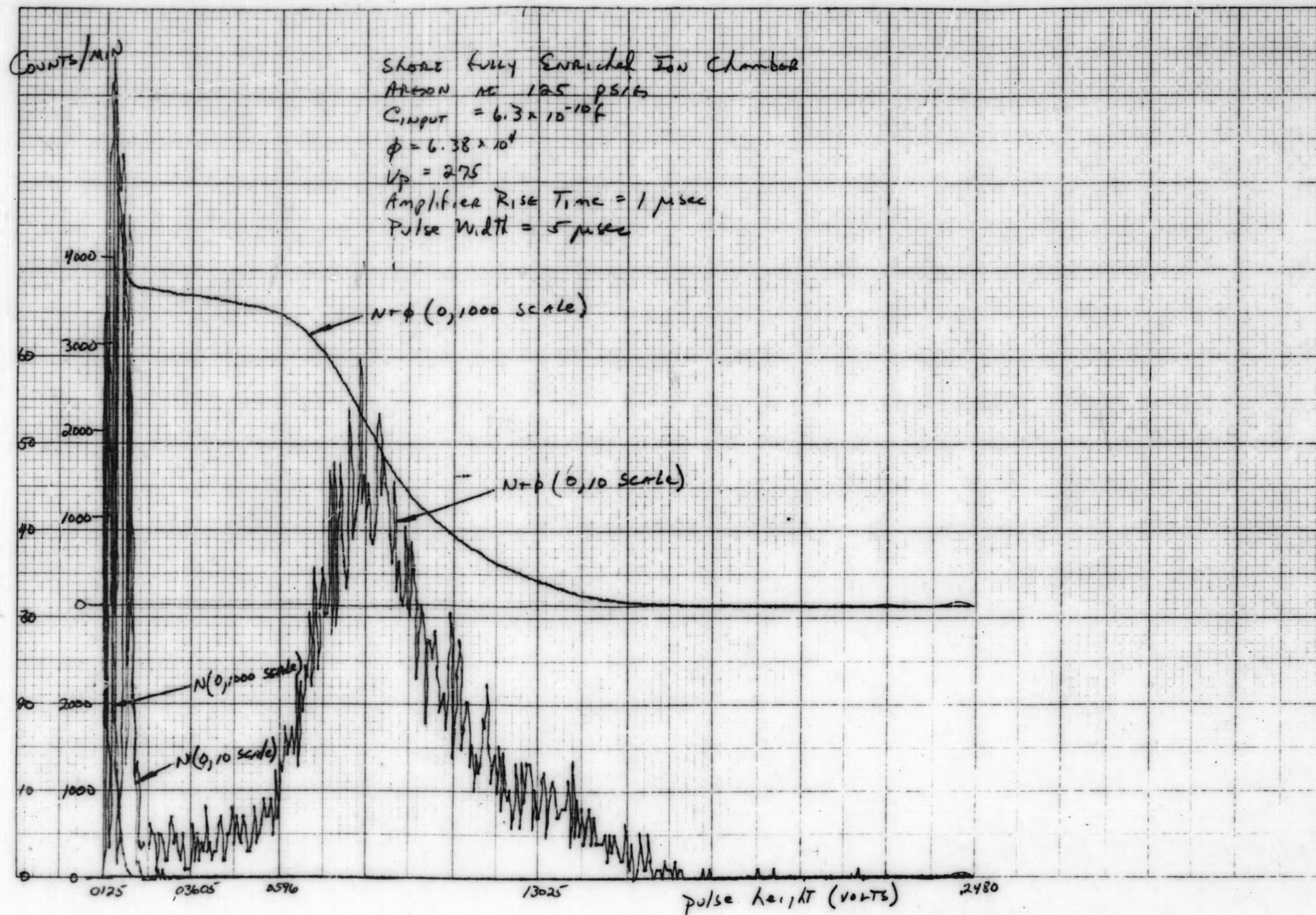


Figure 3-6. Differential and Integral Bias Curves

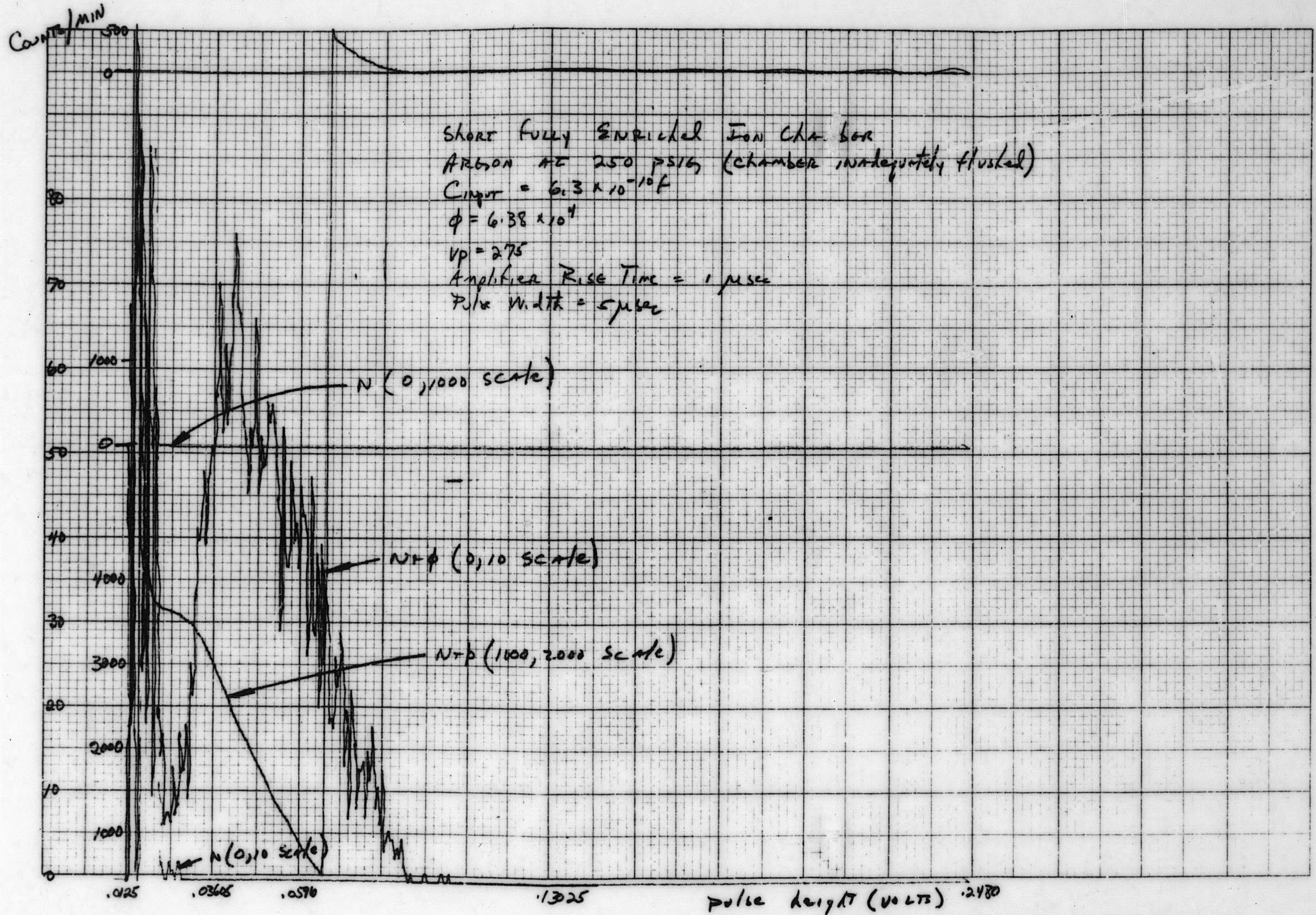


Figure 3-7. Differential and Integral Bias Curves

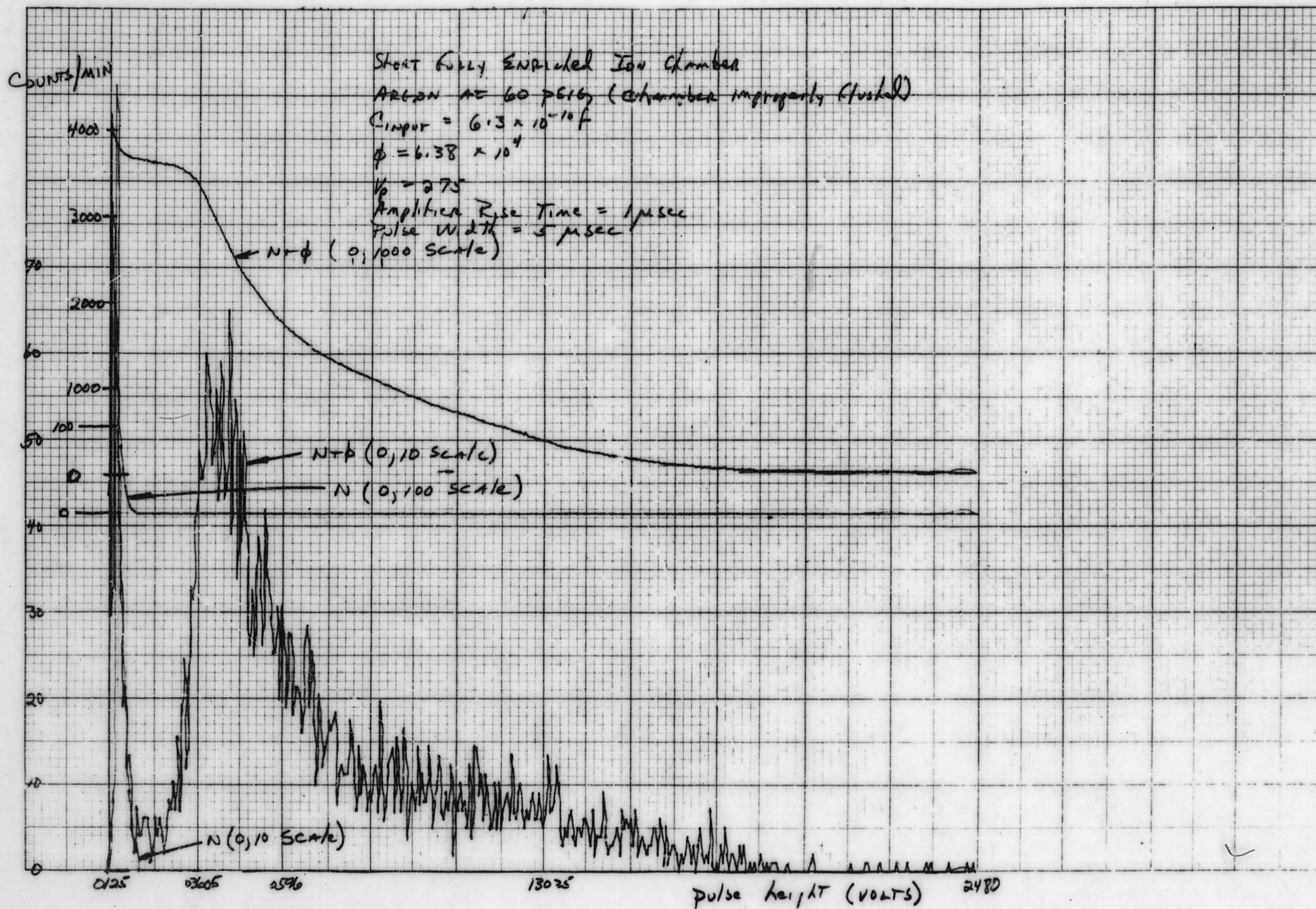


Figure 3-8. Differential and Integral Bias Curves

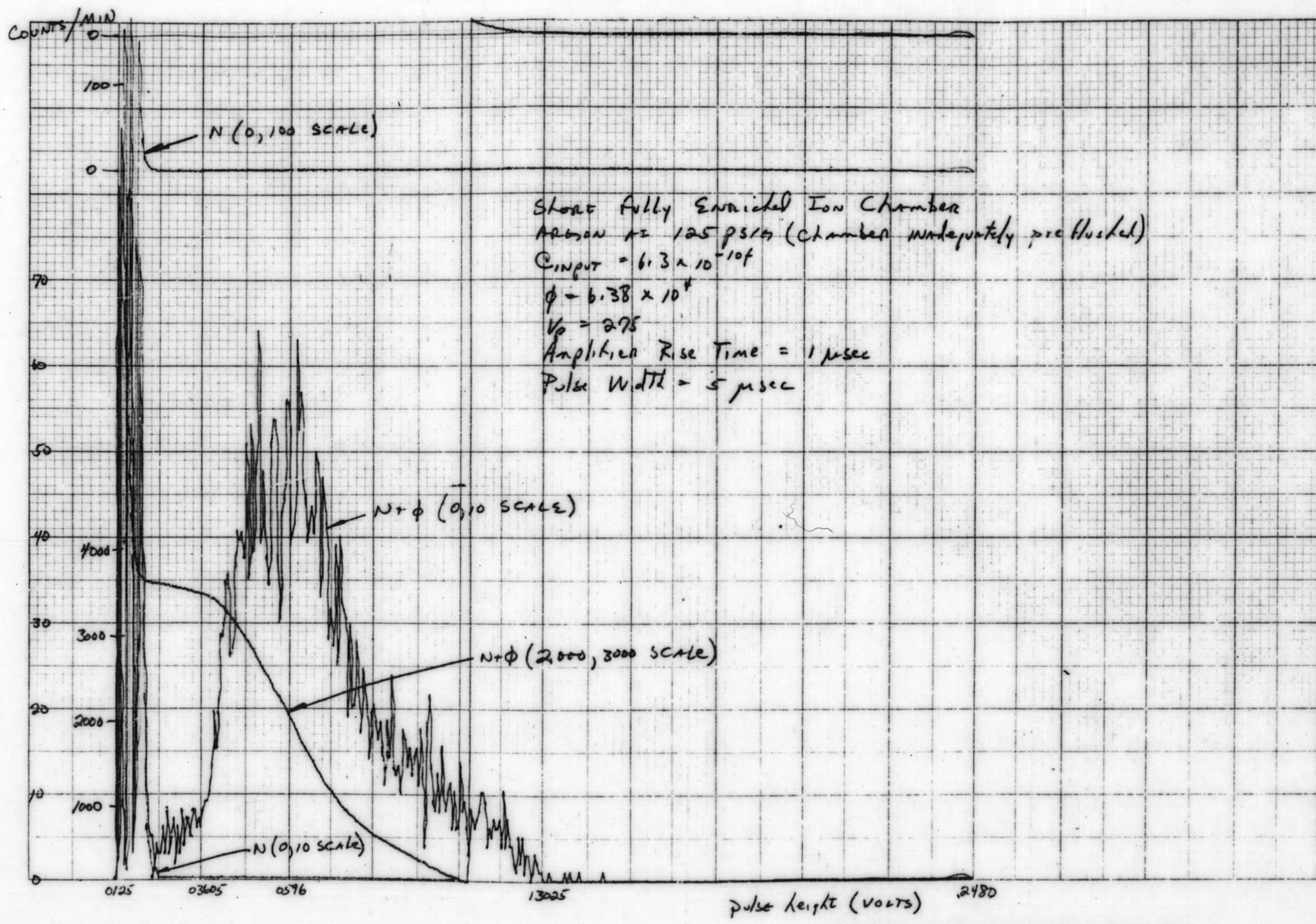


Figure 3-9. Differential and Integral Bias Curves

9-20-67

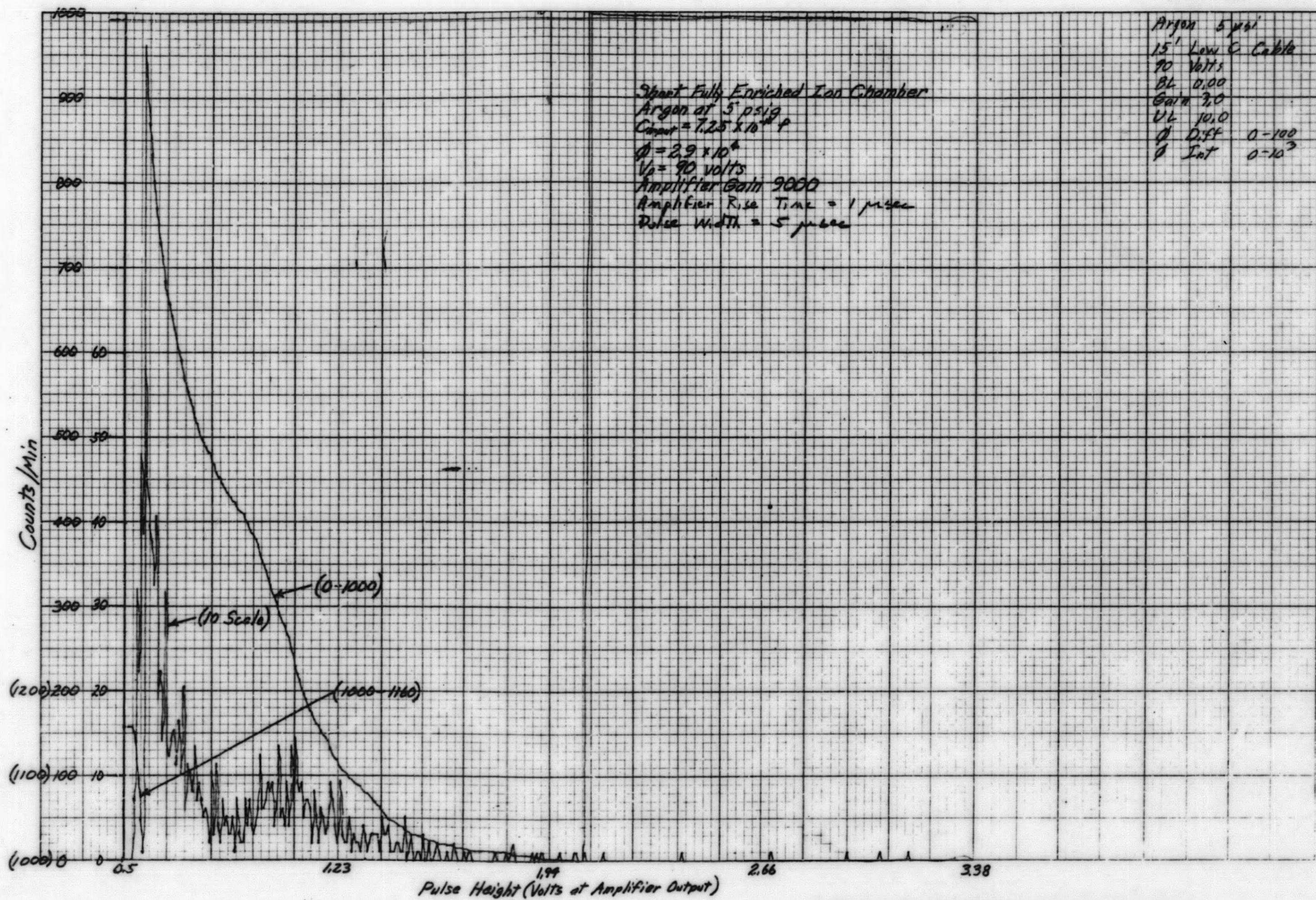


Figure 3-10. Differential and Integral Bias Curves

9-20-67

2

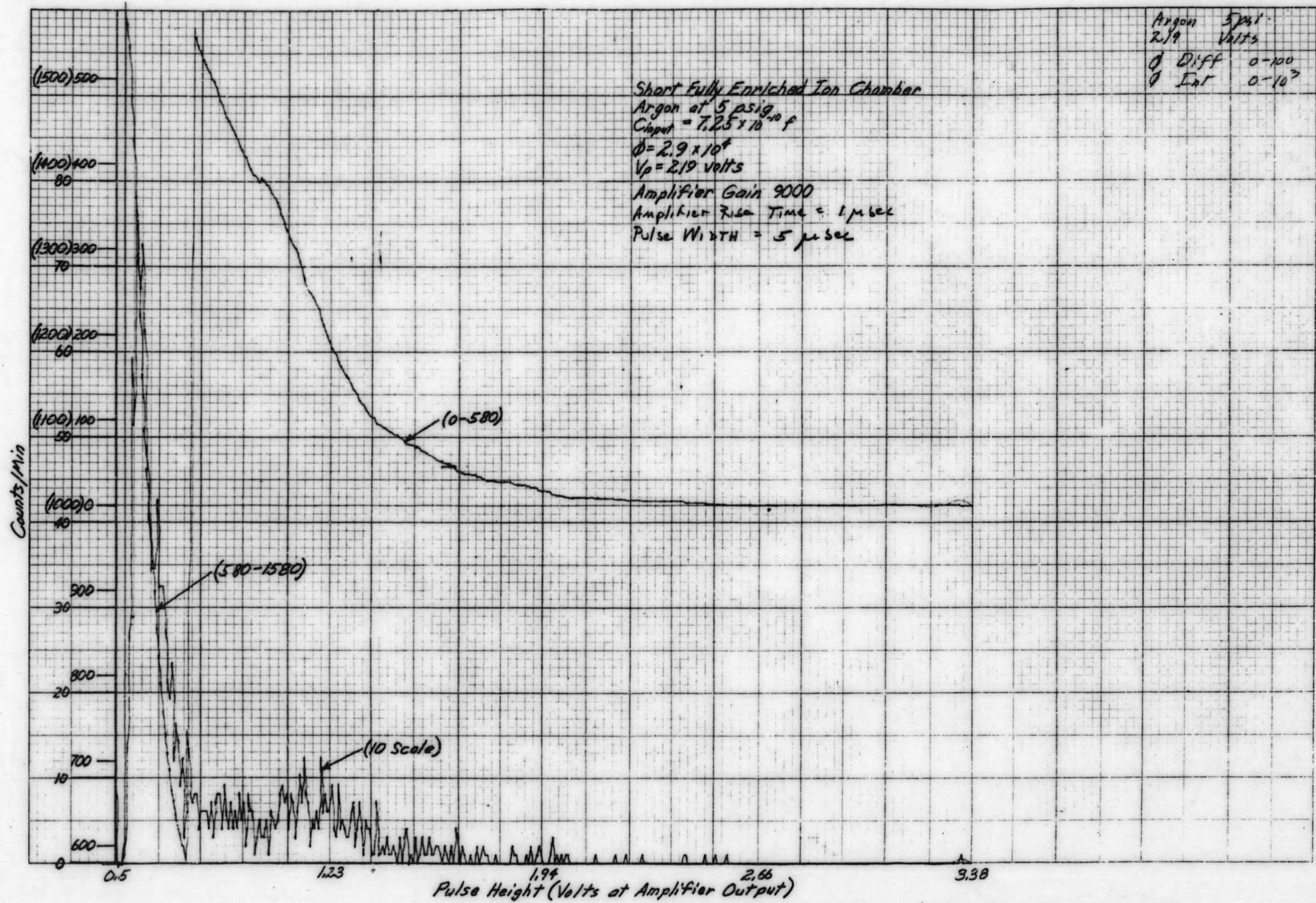


Figure 3-11. Differential and Integral Bias Curves

9-20-63

3

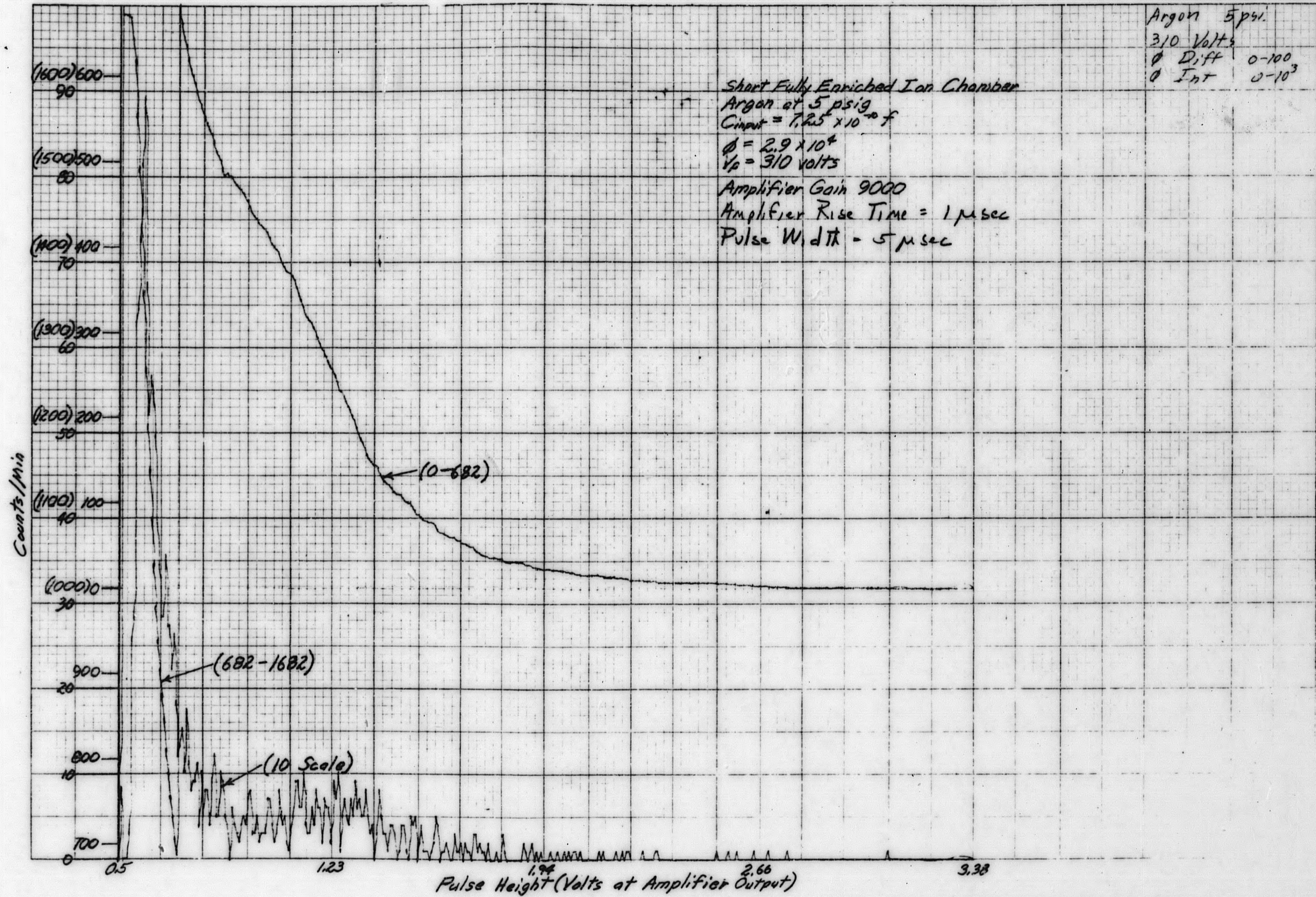


Figure 3-12. Differential and Integral Bias Curves

9-20-67

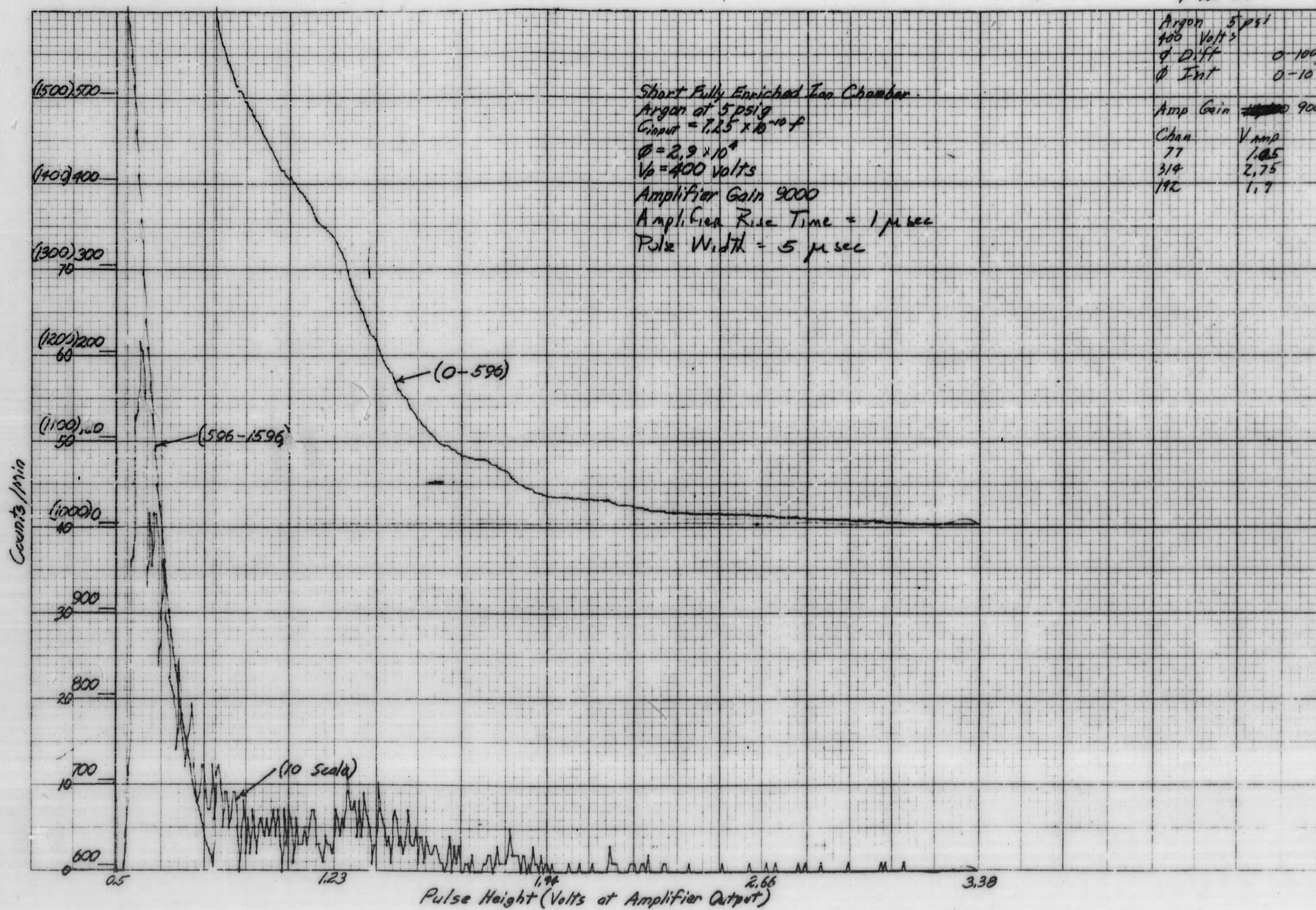


Figure 3-13. Differential and Integral Bias Curves

9-20-63

8

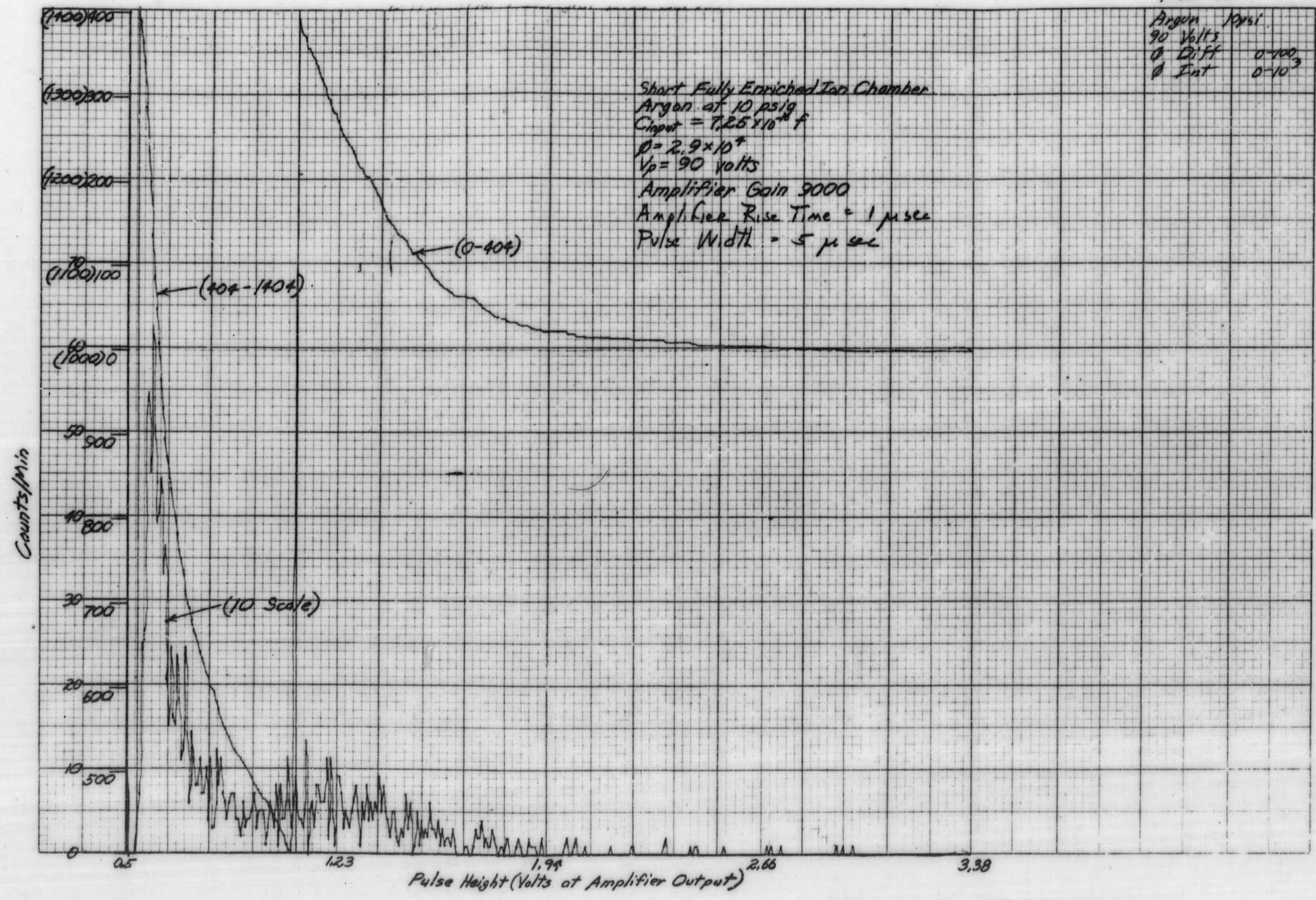


Figure 3-14. Differential and Integral Bias Curves

9-20-63

7

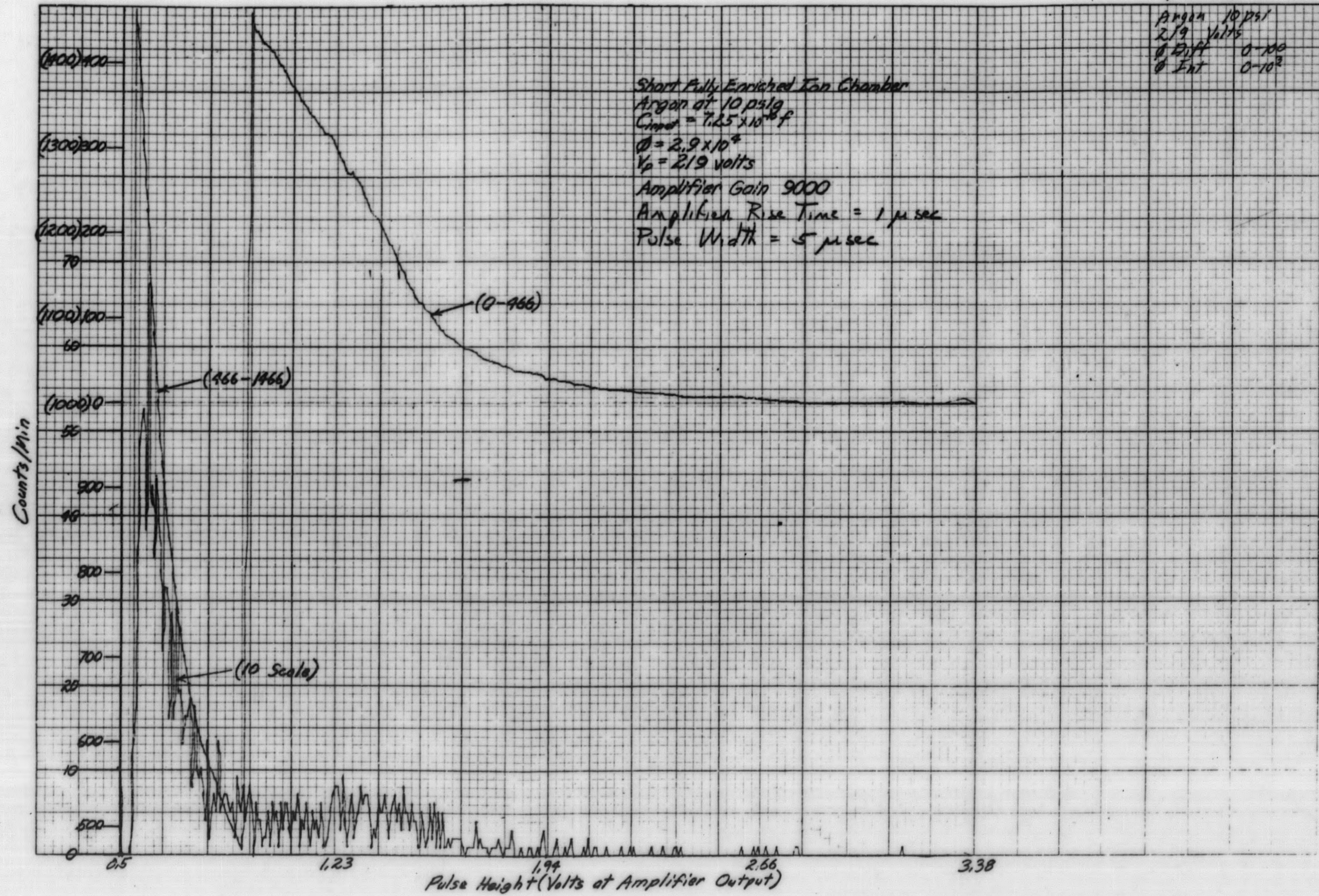


Figure 3-15. Differential and Integral Bias Curves

9-20-67

6

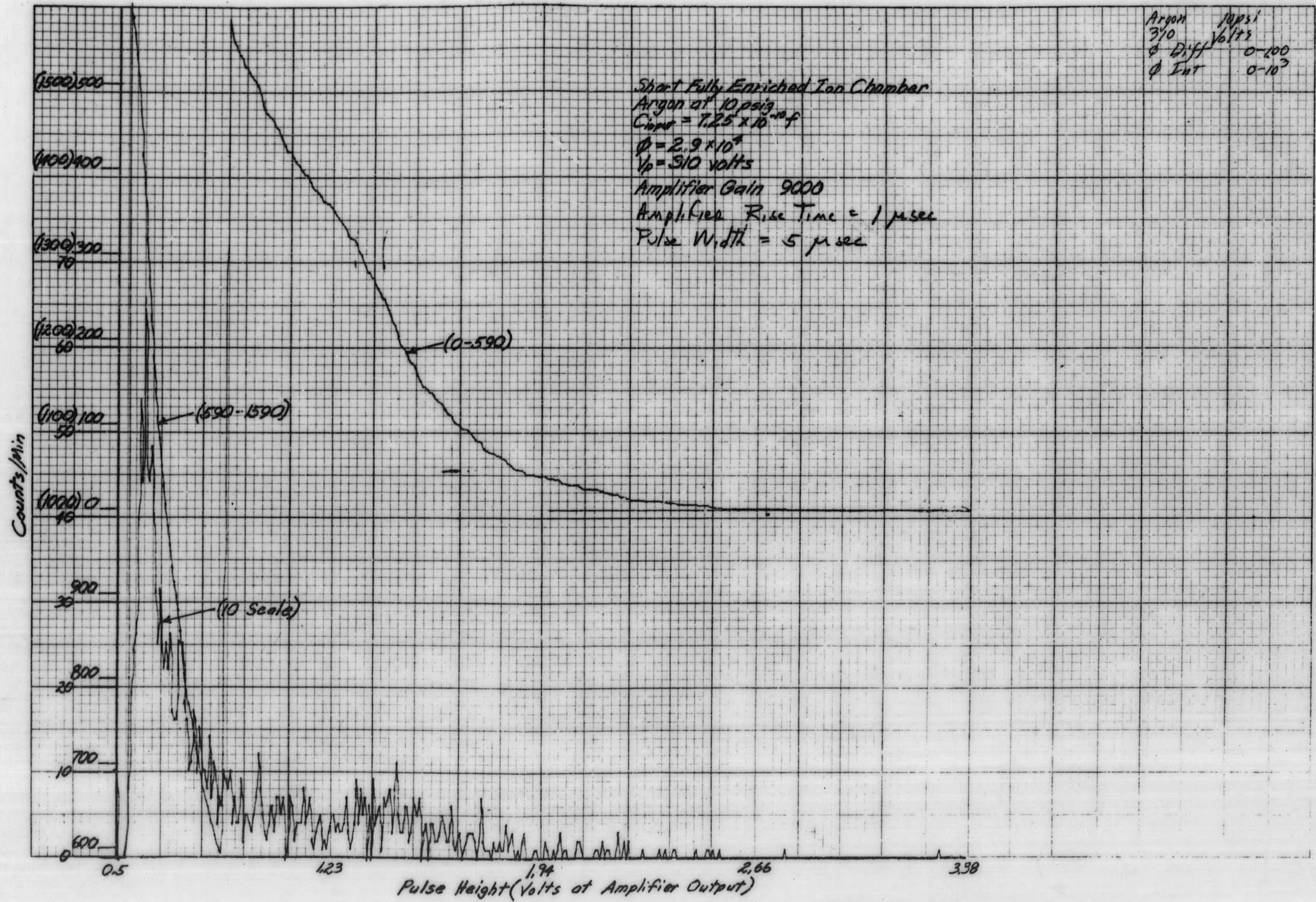


Figure 3-16. Differential and Integral Bias Curves

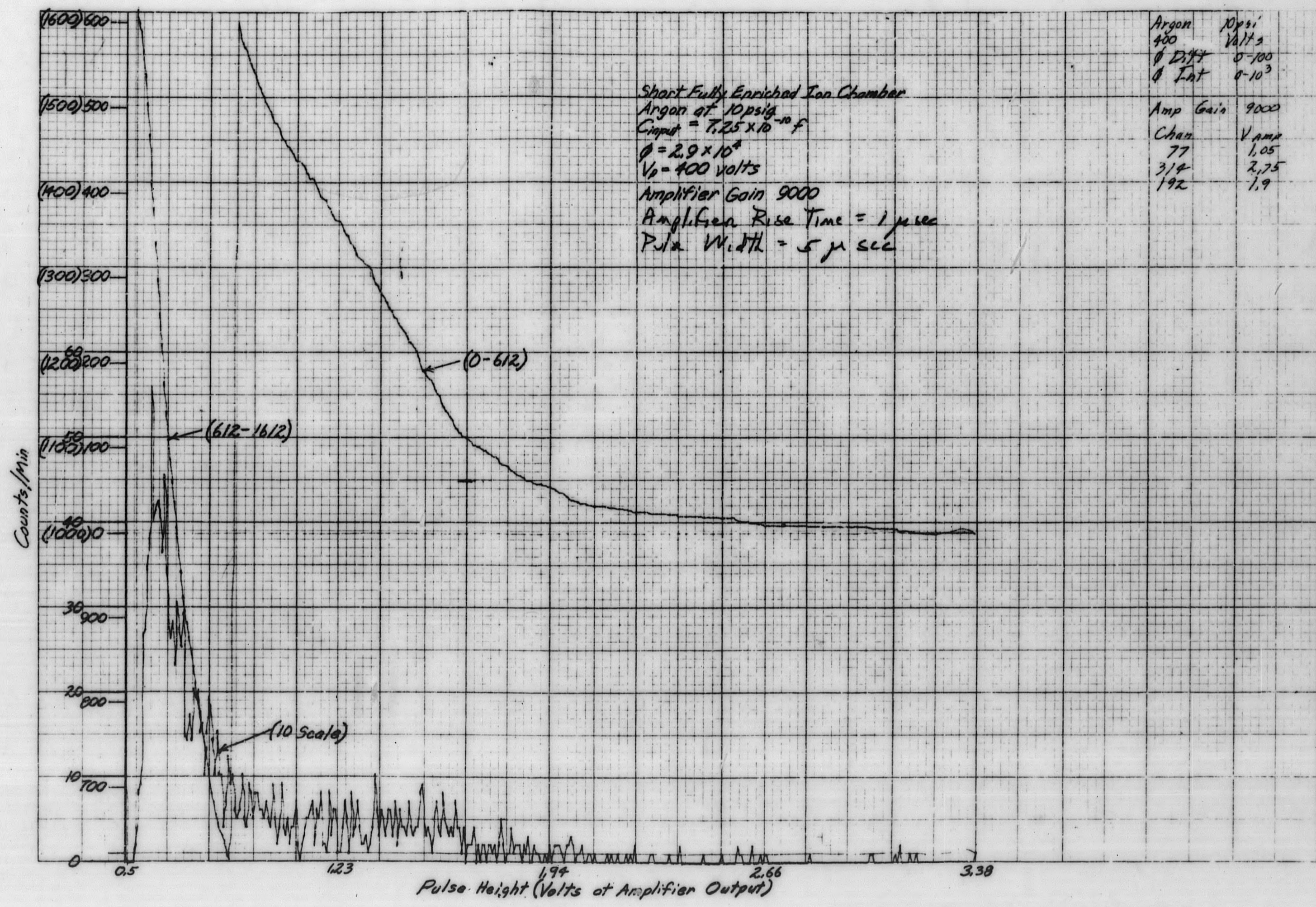


Figure 3-17. Differential and Integral Bias Curves

4-20-63

9

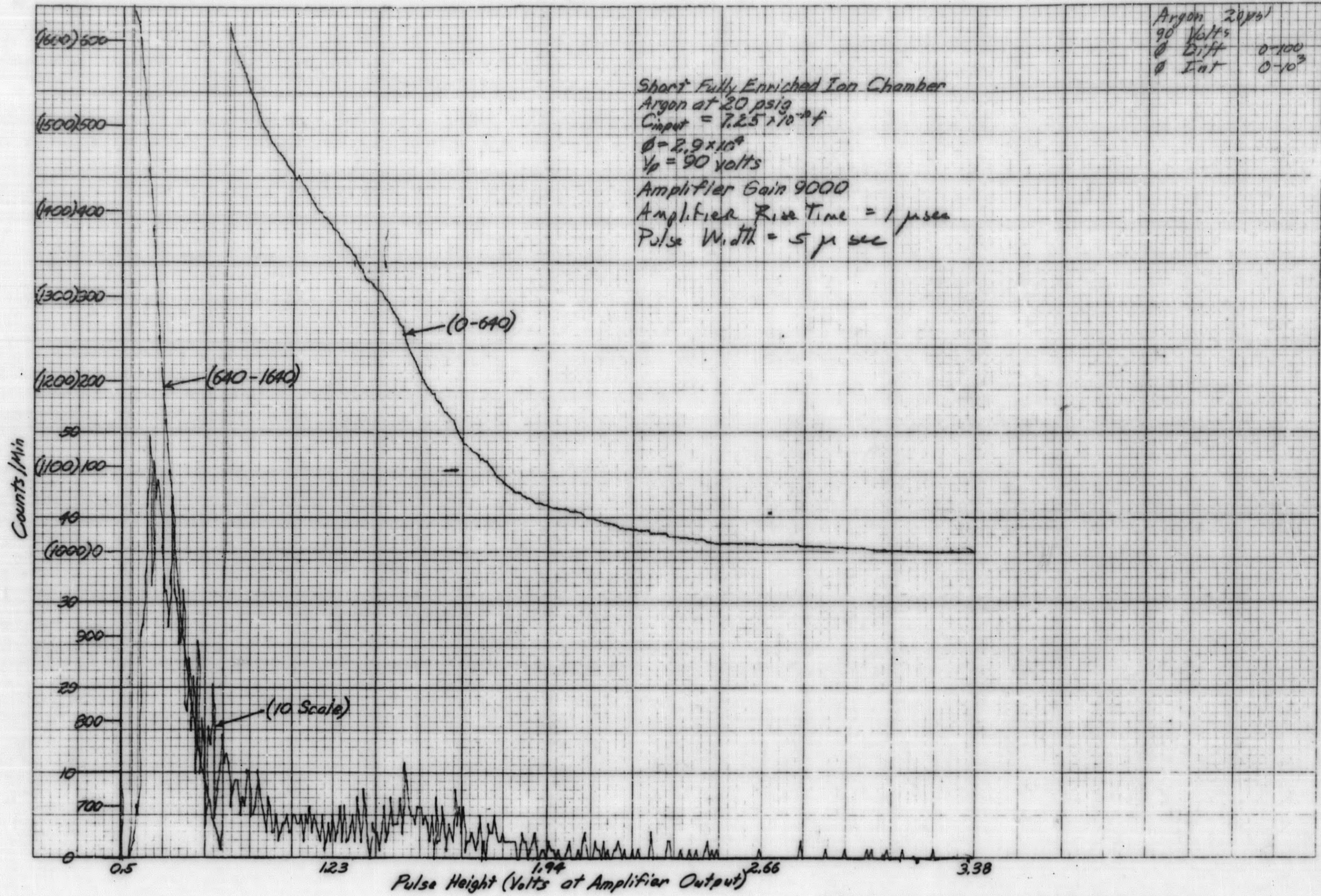


Figure 3-18. Differential and Integral Bias Curves

9-20-63

10

Argon 20psi
 V_b 219 Volts
 Φ Diff 0-100
 Φ Int 0-10³

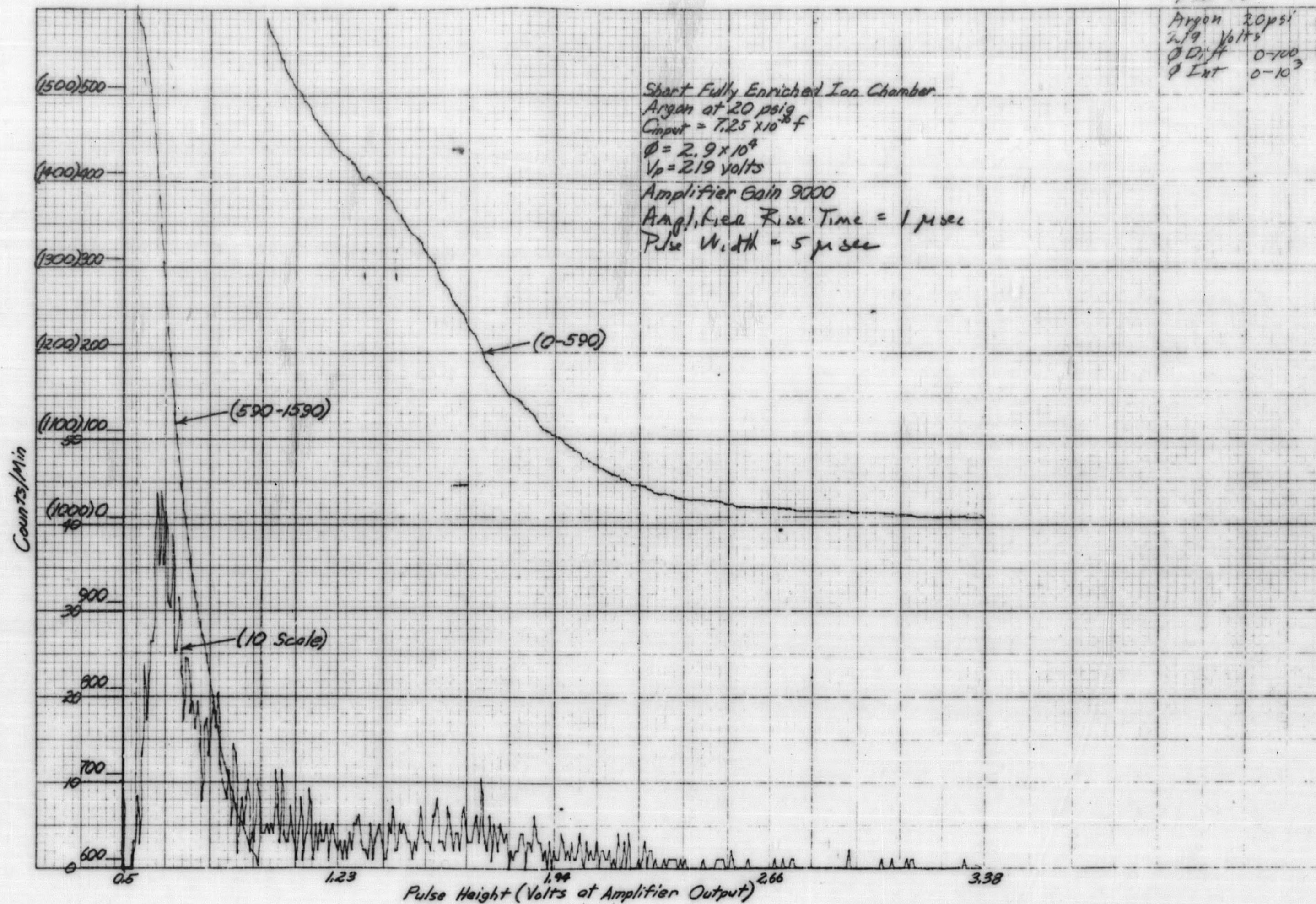


Figure 3-19. Differential and Integral Bias Curves

9-20-63

11

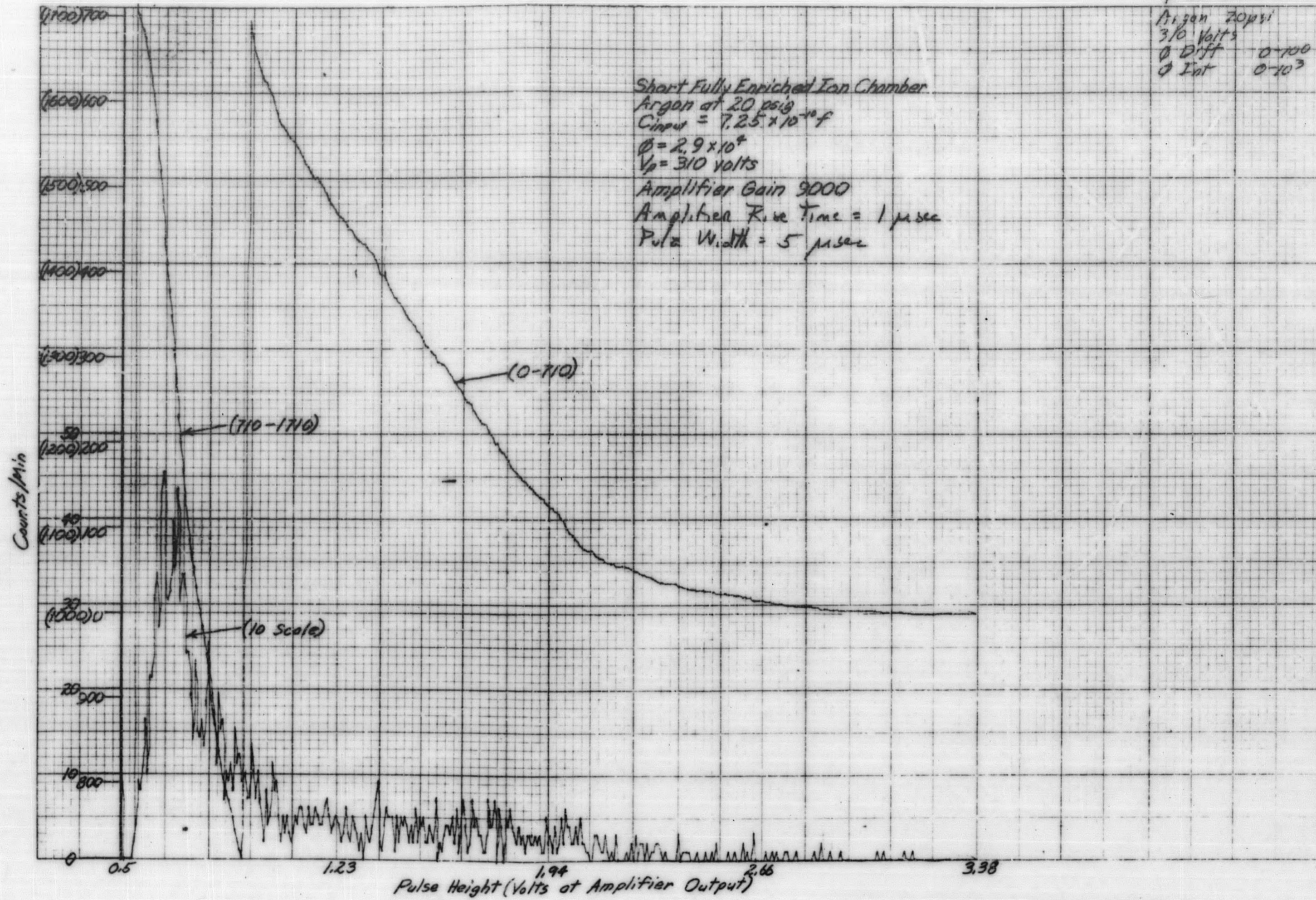


Figure 3-20. Differential and Integral Bias Curves

9-20-63 12

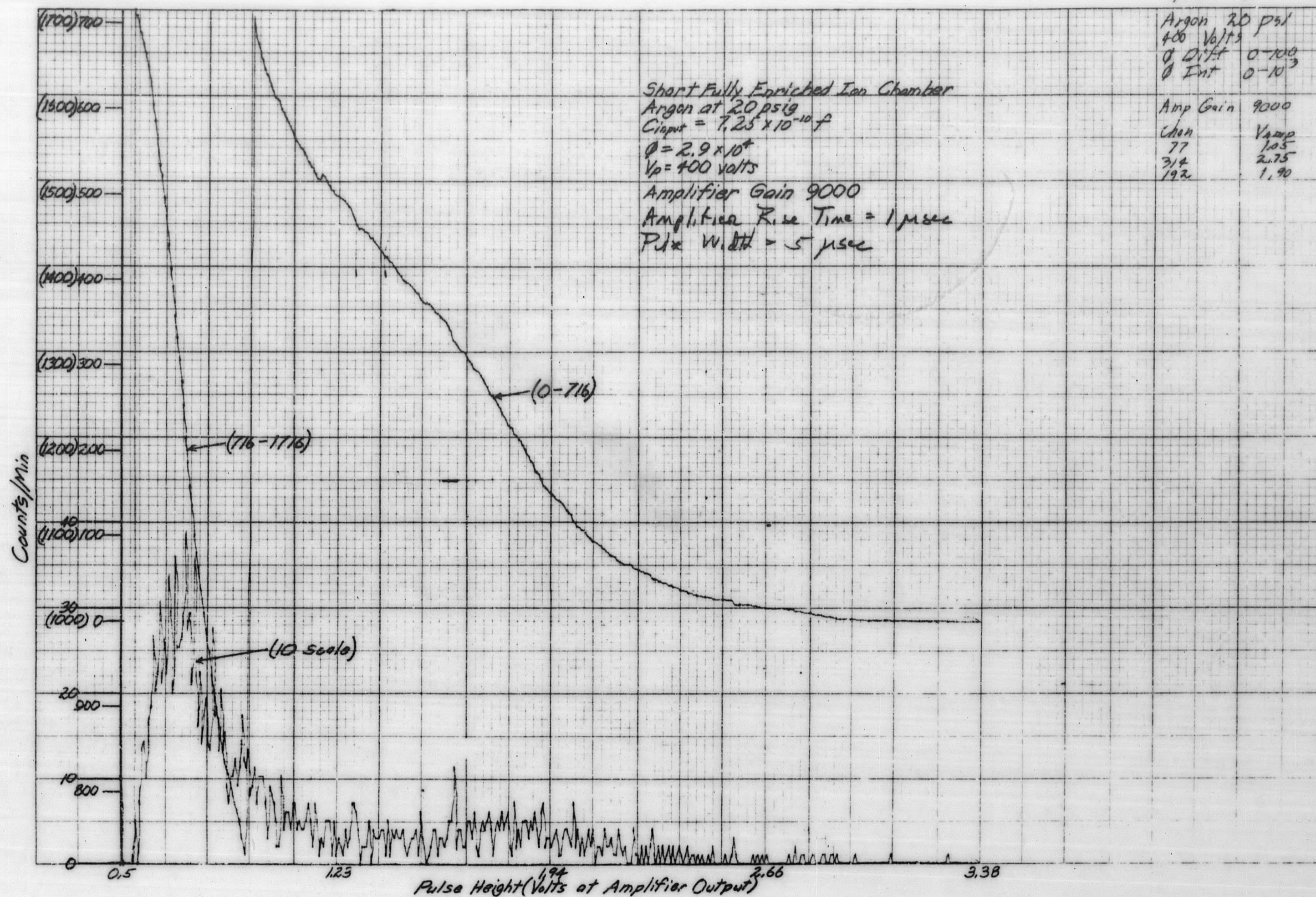


Figure 3-21. Differential and Integral Bias Curves

9-20-63

17

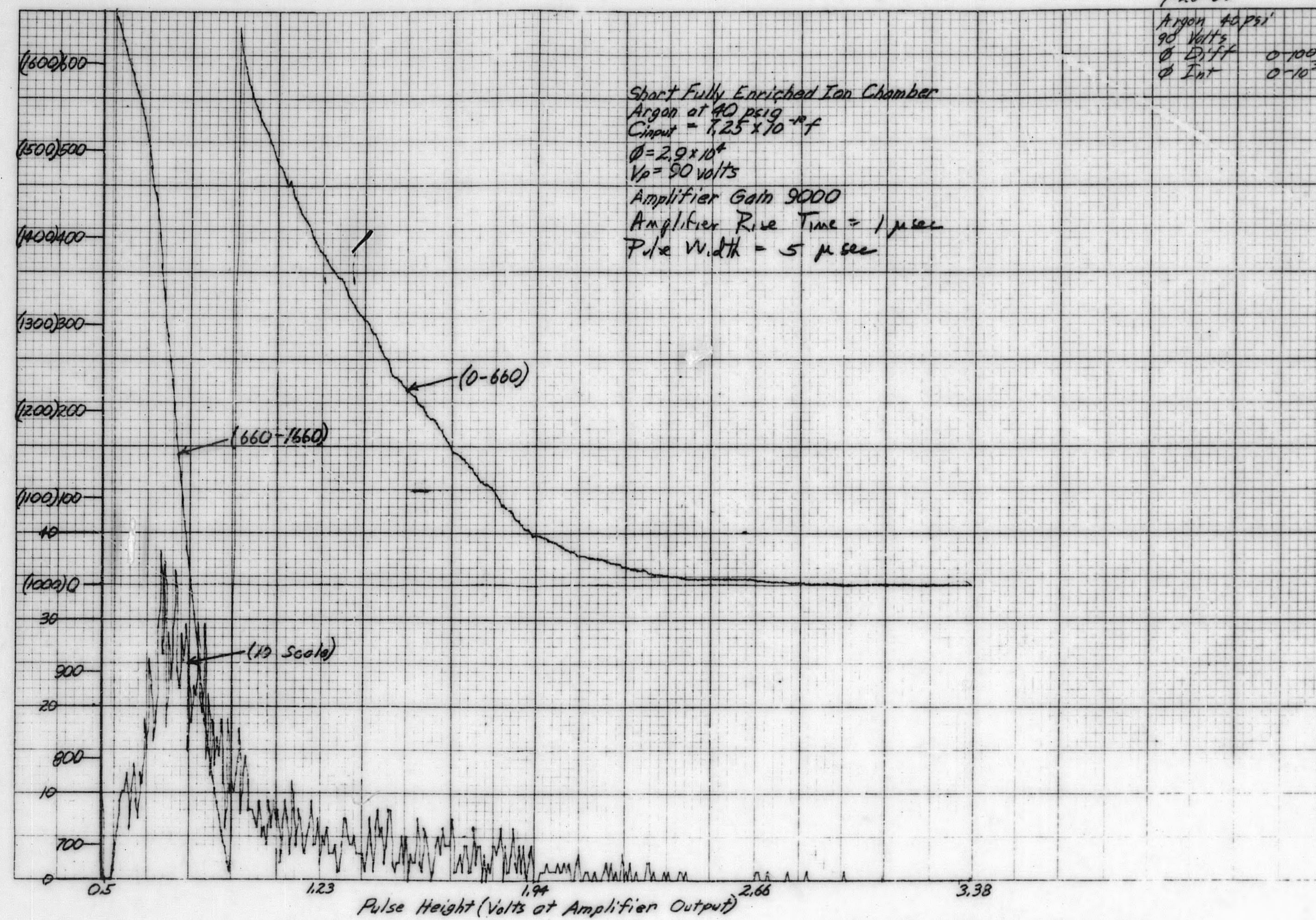
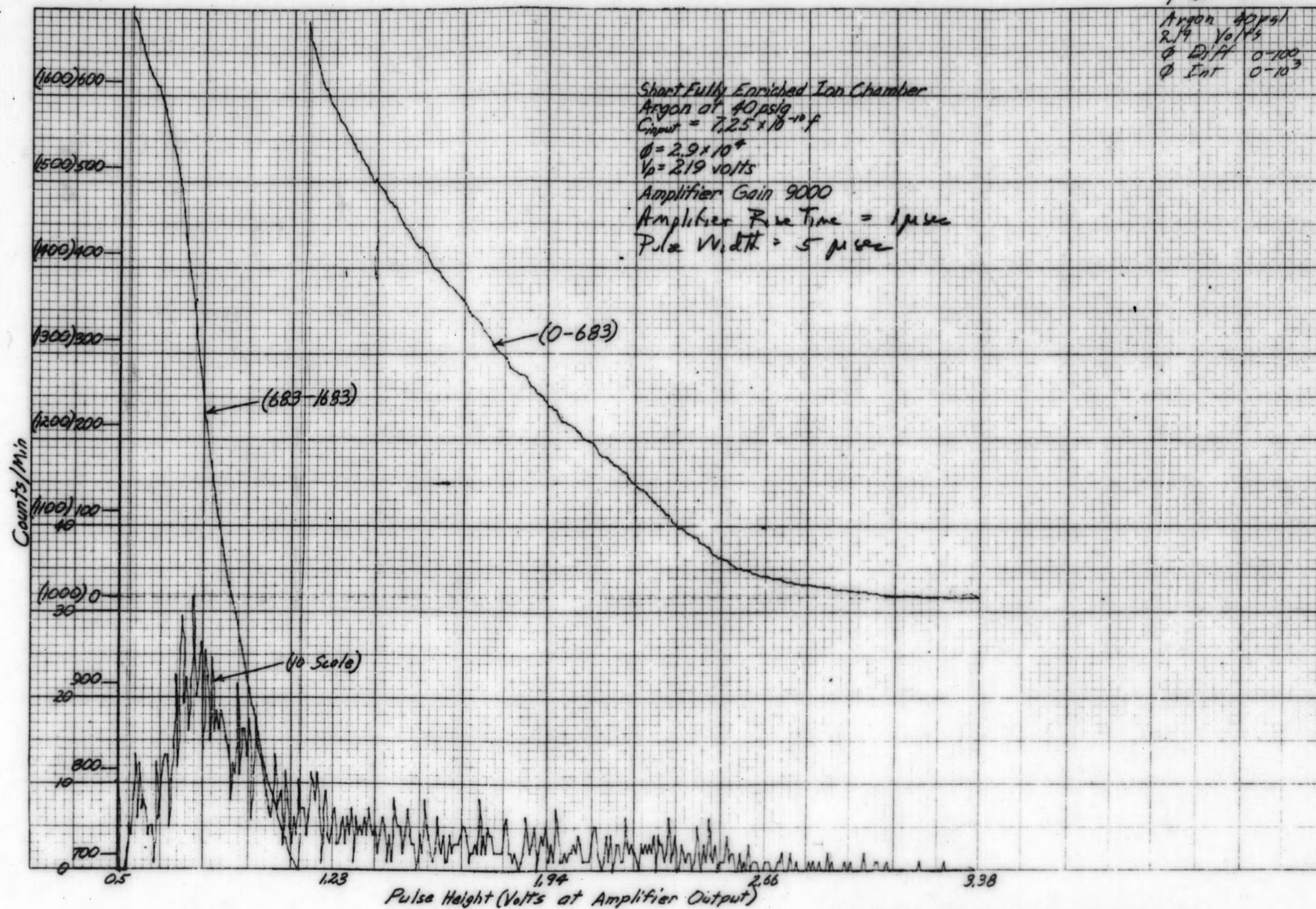


Figure 3-22. Differential and Integral Bias Curves

4-20-63

16



Argon 40 psig
 R. 19 Volts
 Q Diff 0-100
 Q Int 0-10³

Figure 3-23. Differential and Integral Bias Curves

9-20-67 15
 Argon at 40 psig
 V_p = 310 volts
 ϕ Diff 0-100
 ϕ Int 0-10³

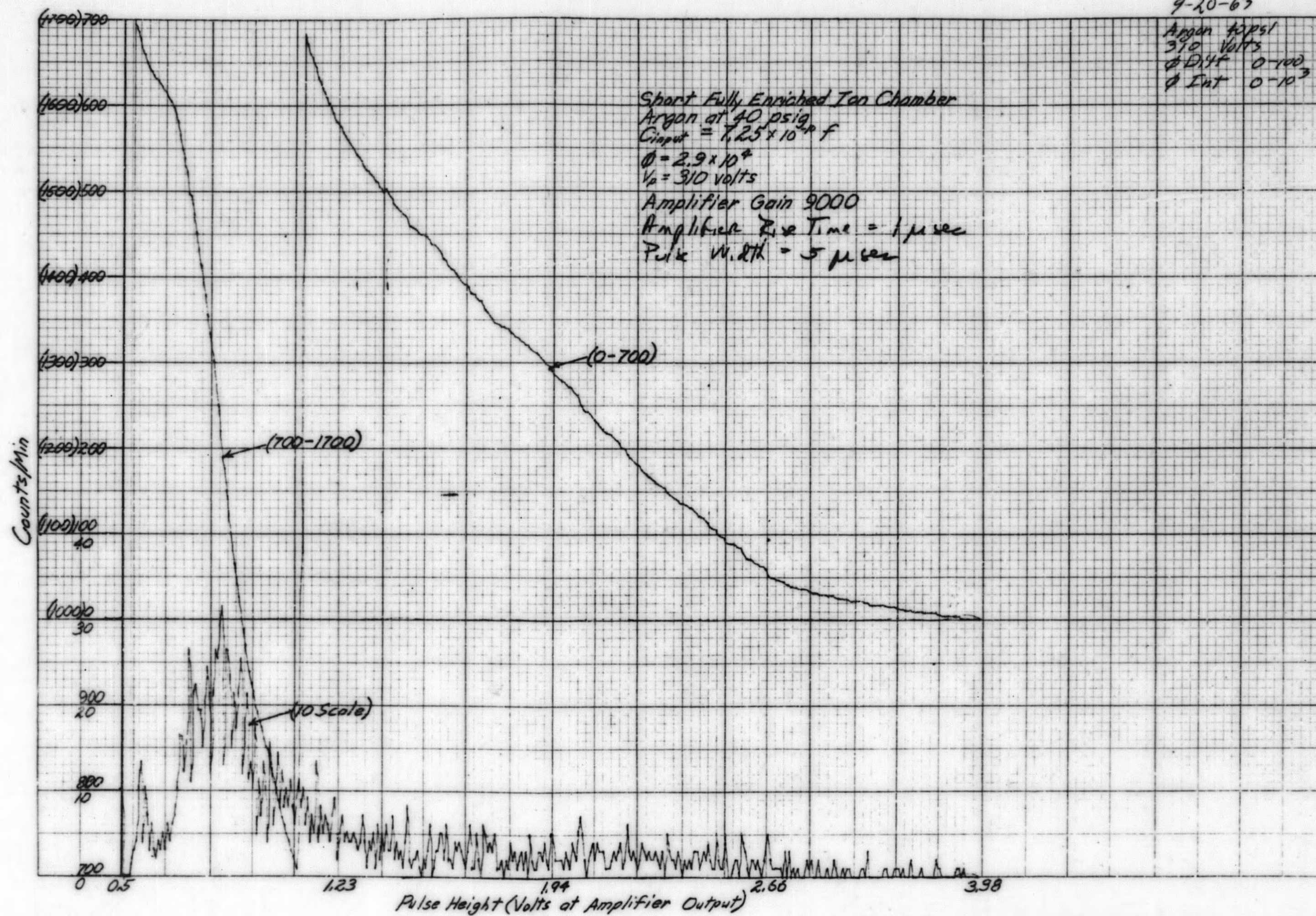


Figure 3-24. Differential and Integral Bias Curves

9-20-63

14

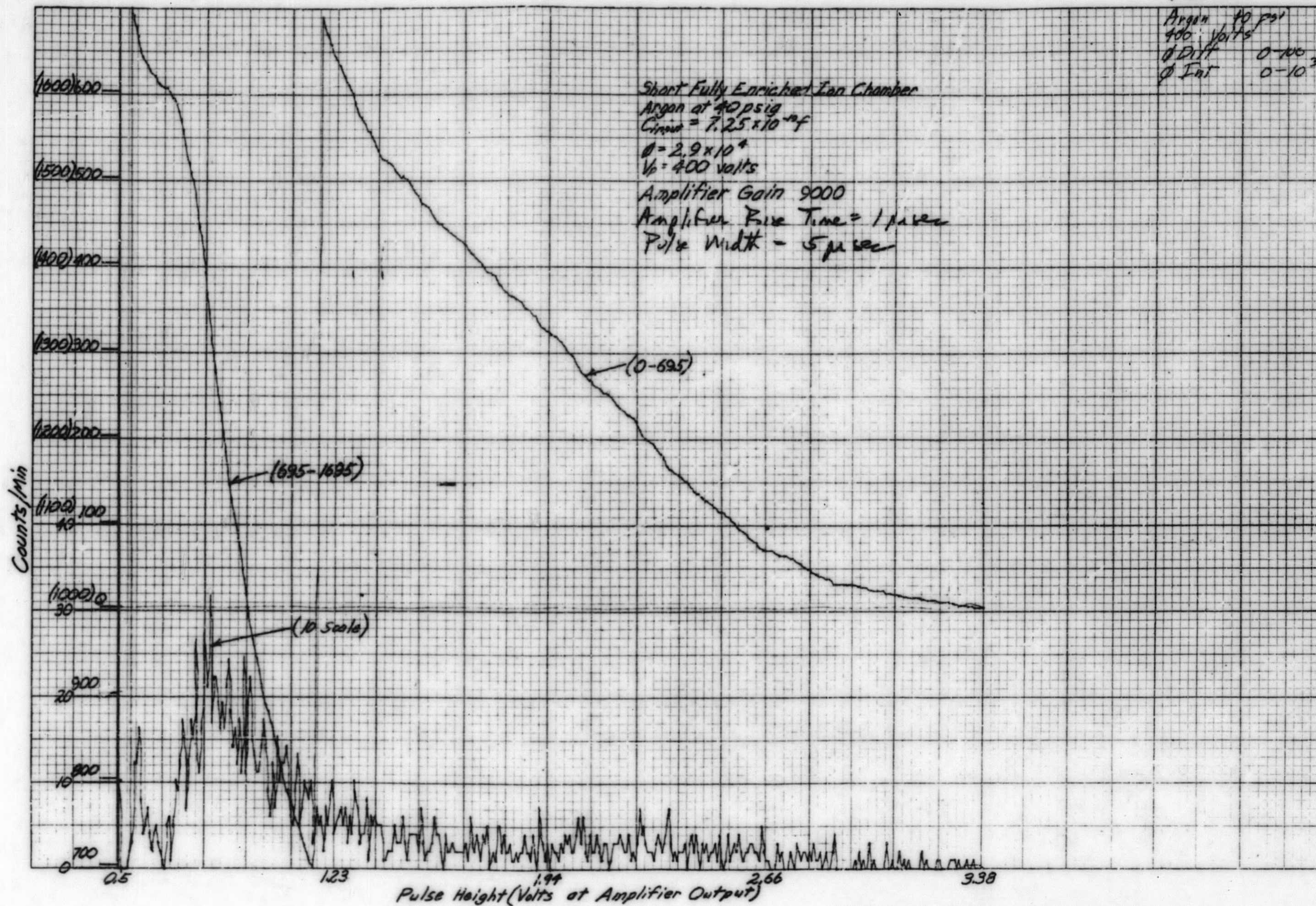


Figure 3-25. Differential and Integral Bias Curves

9-20-67

13

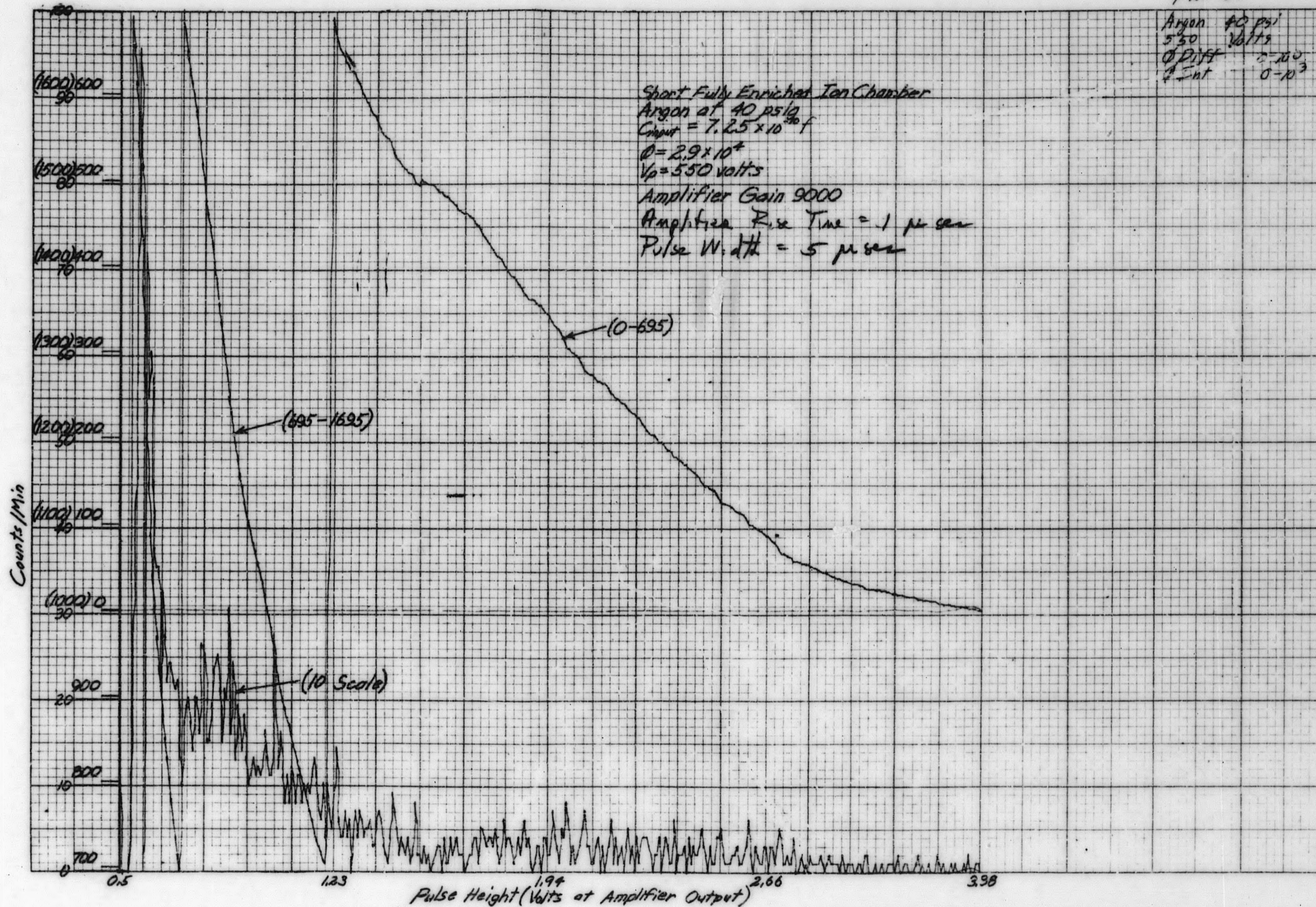


Figure 3-26. Differential and Integral Bias Curves

9-20-63 22

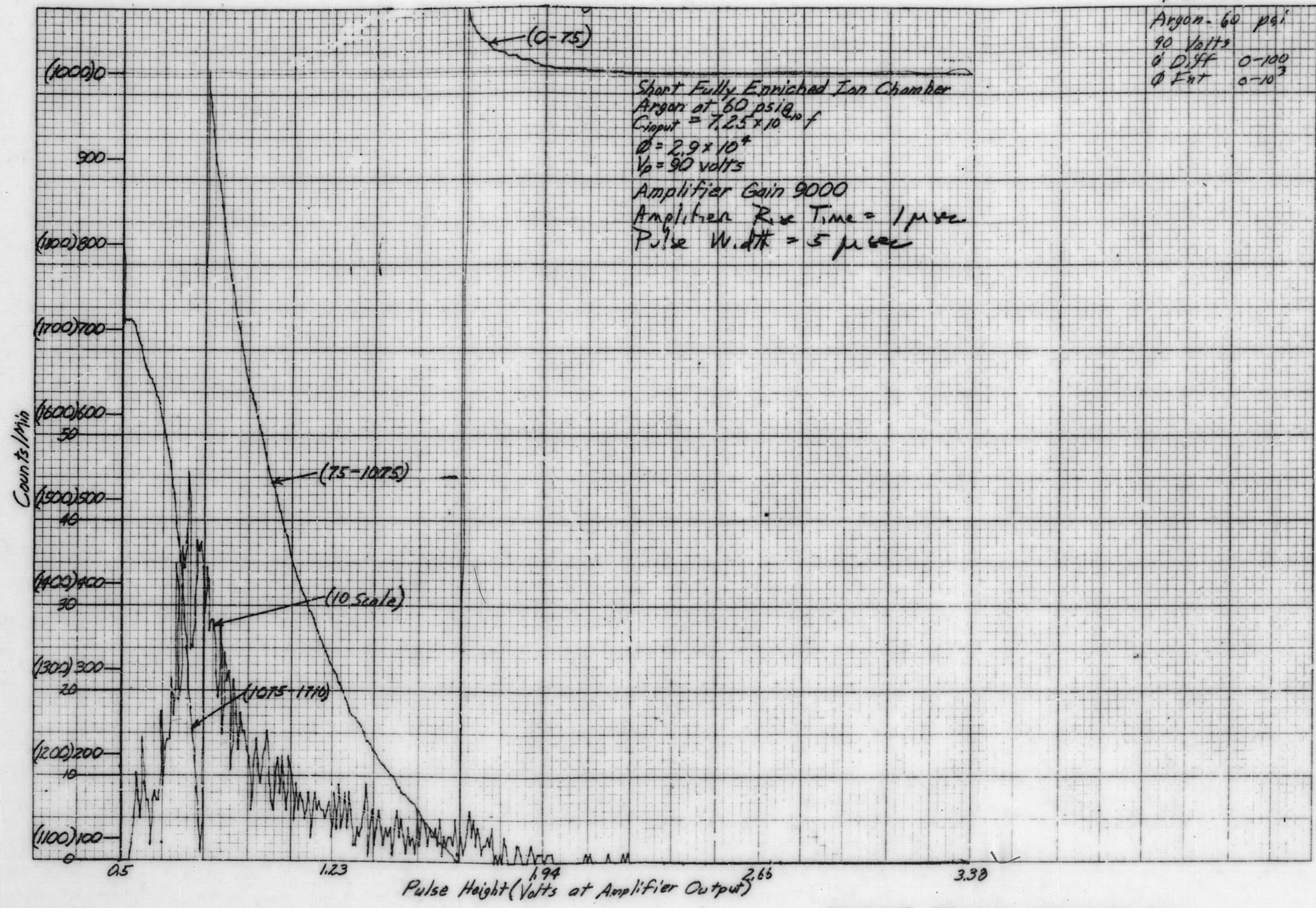


Figure 3-27. Differential and Integral Bias Curves

4-20-63 21
 Argon 60 psi
 2.99 Volts
 ϕ Diff. $0-10^3$
 ϕ Int. $0-10^3$

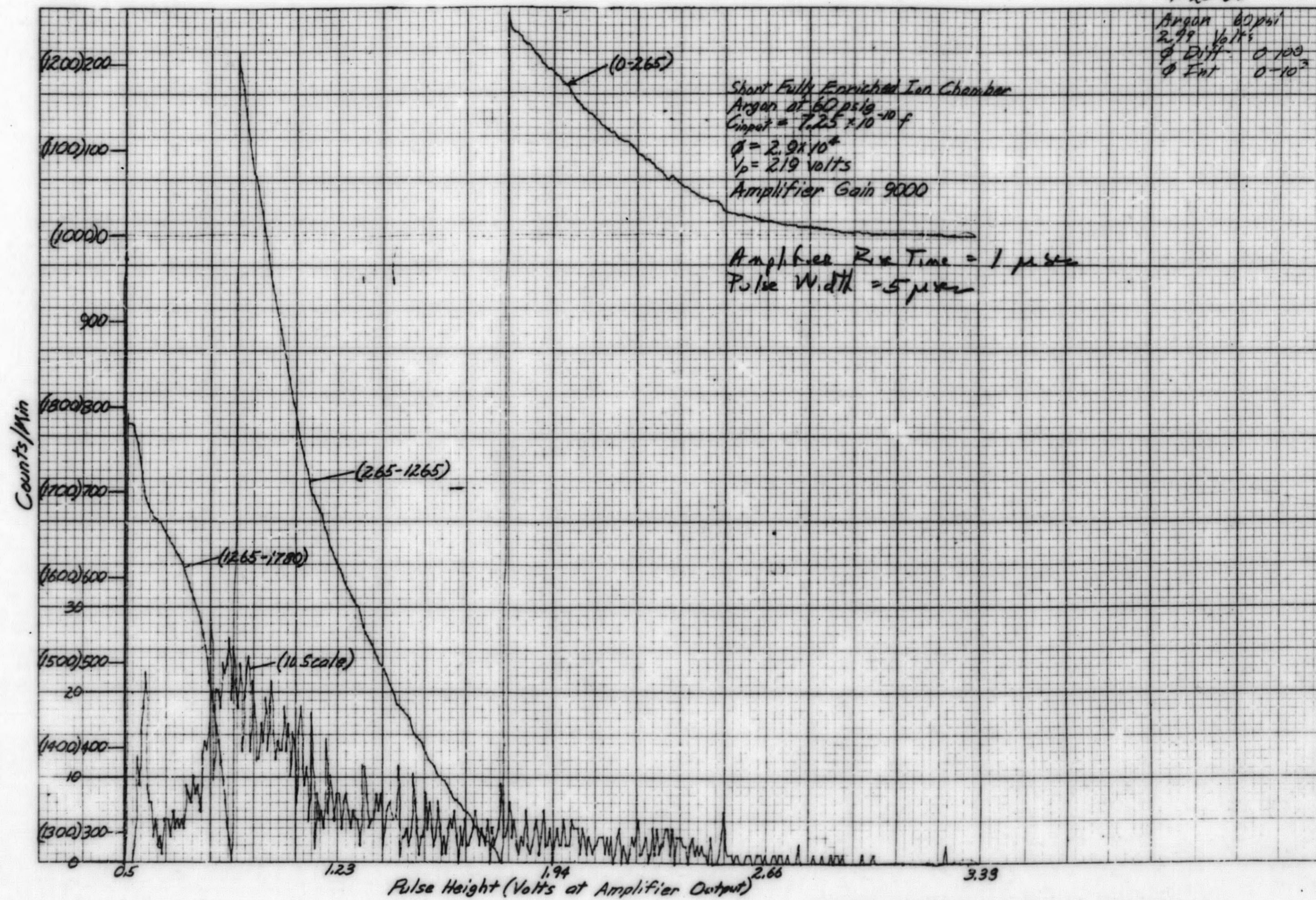


Figure 3-28. Differential and Integral Bias Curves

9-20-63

20

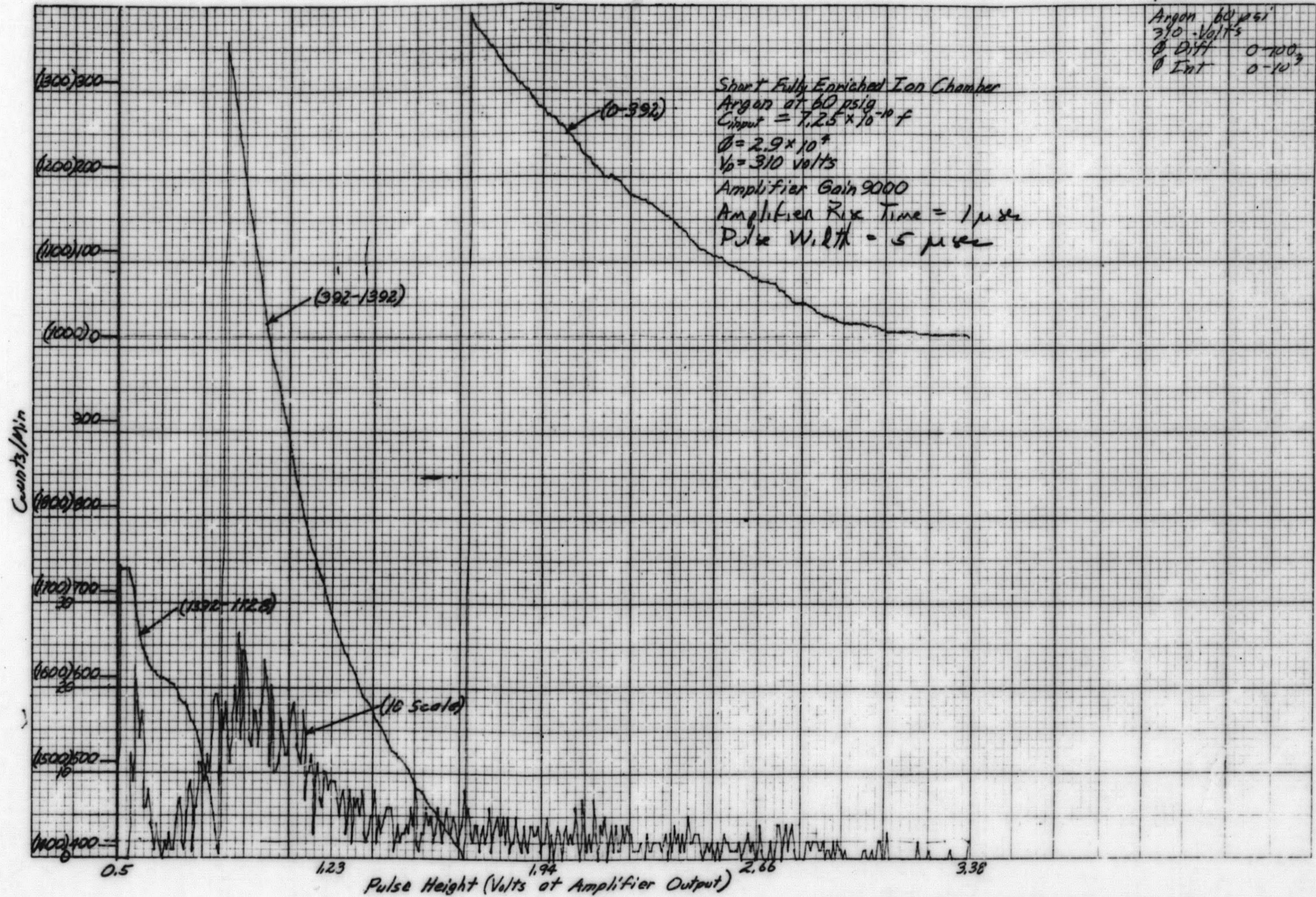


Figure 3-29. Differential and Integral Bias Curves

9-20-63

19

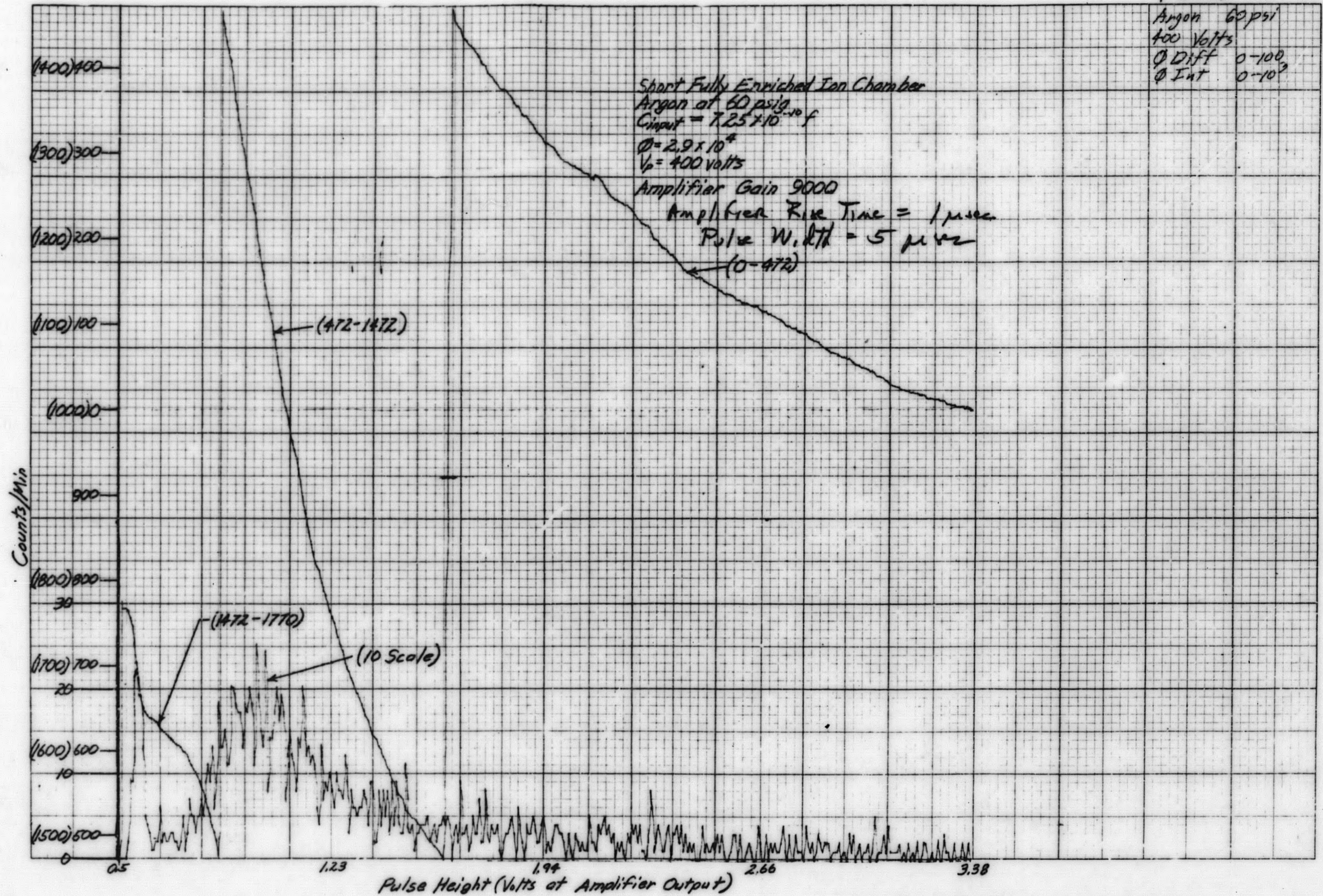


Figure 3-30. Differential and Integral Bias Curves

9-20-63

18

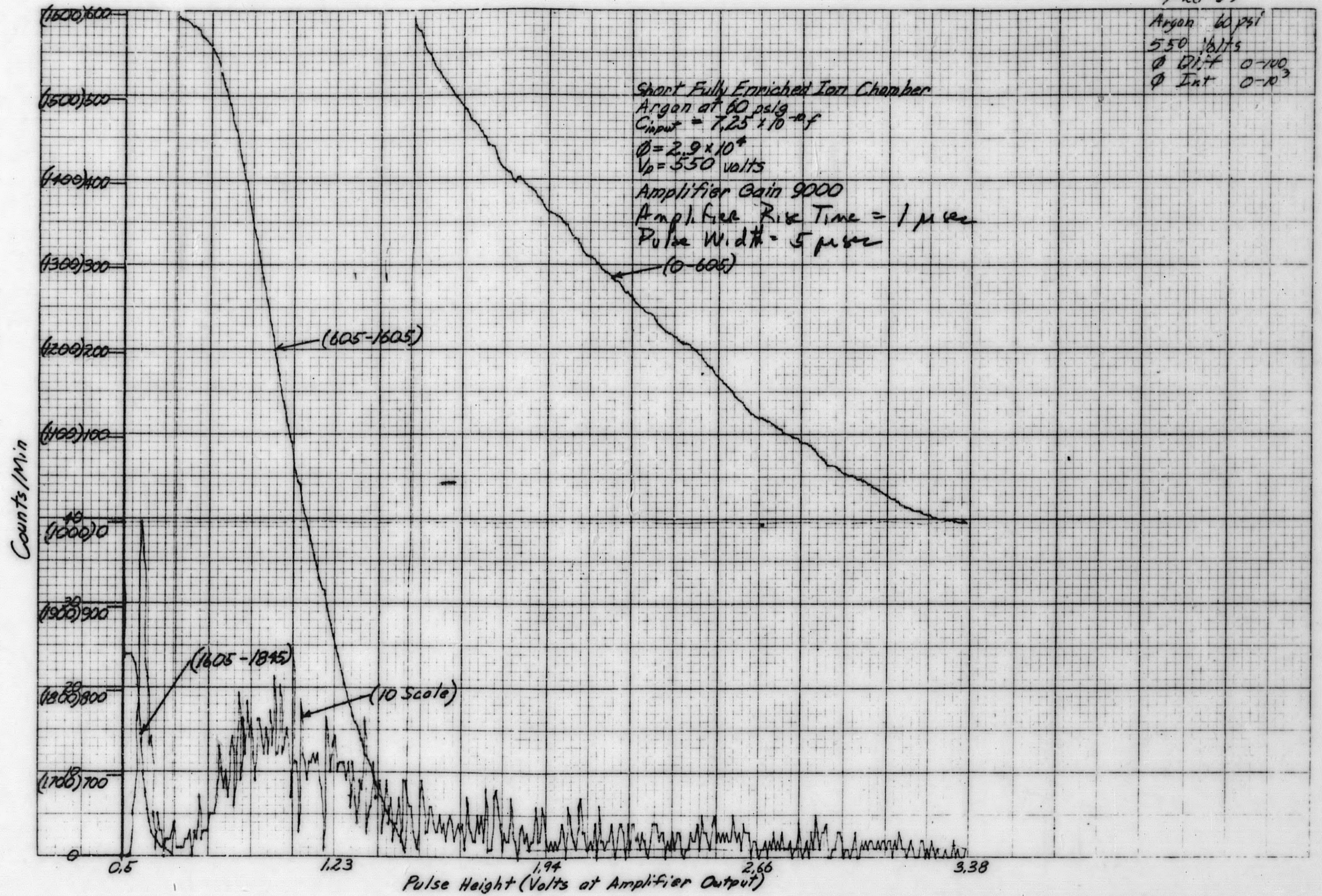


Figure 3-31. Differential and Integral Bias Curves

9-25-67

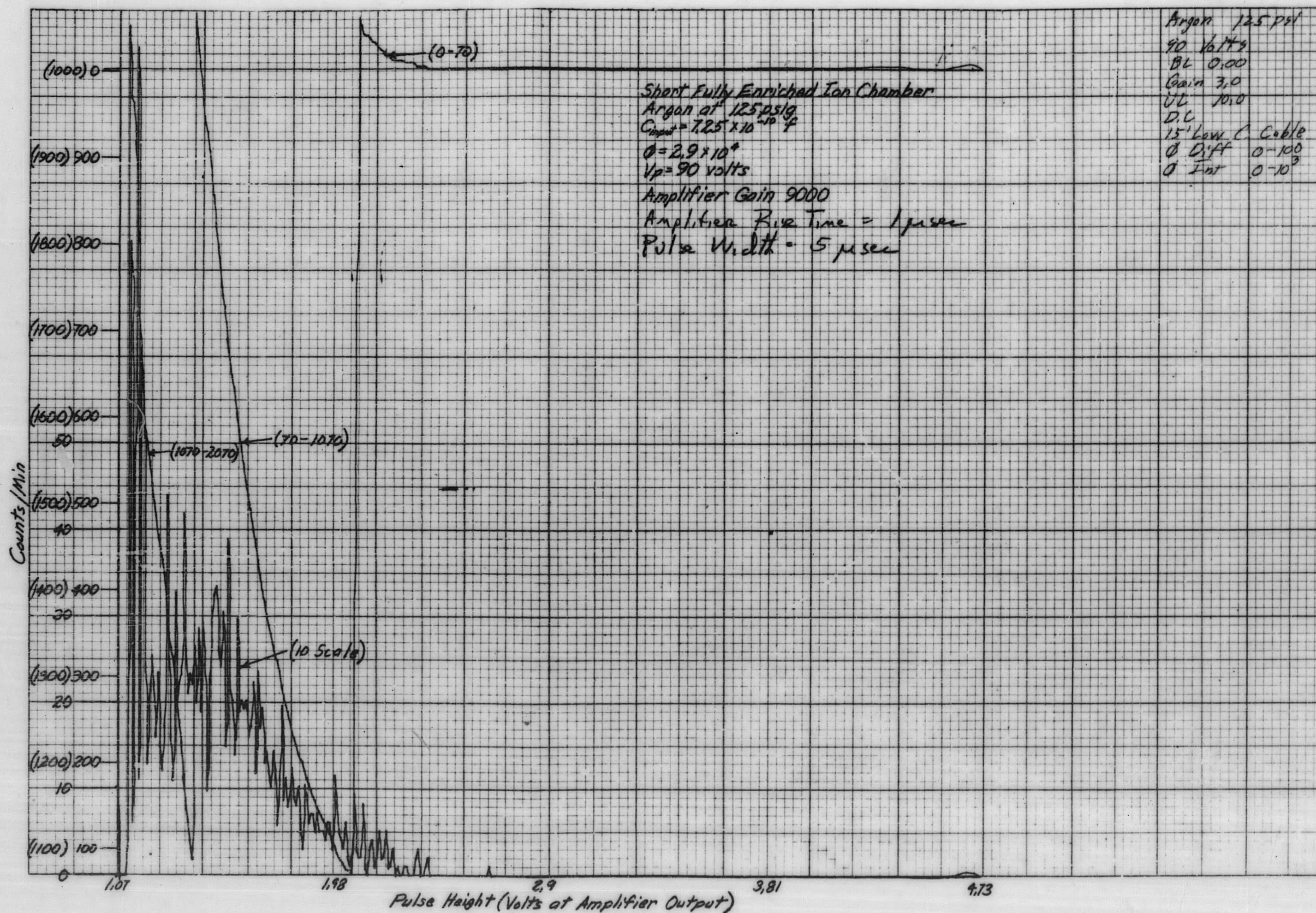


Figure 3-32. Differential and Integral Bias Curves

9-25-63

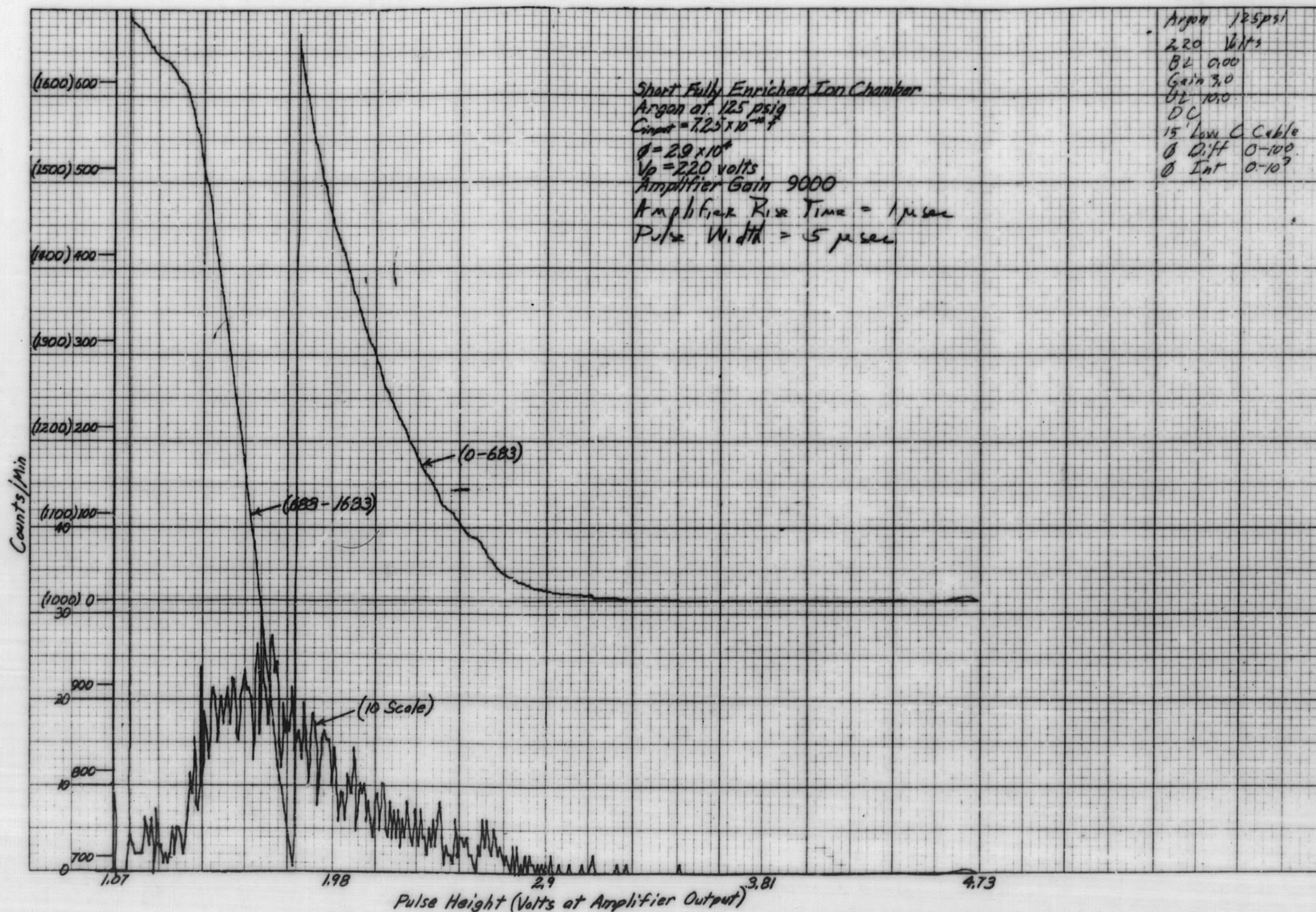


Figure 3-33. Differential and Integral Bias Curves

9-25-67

f

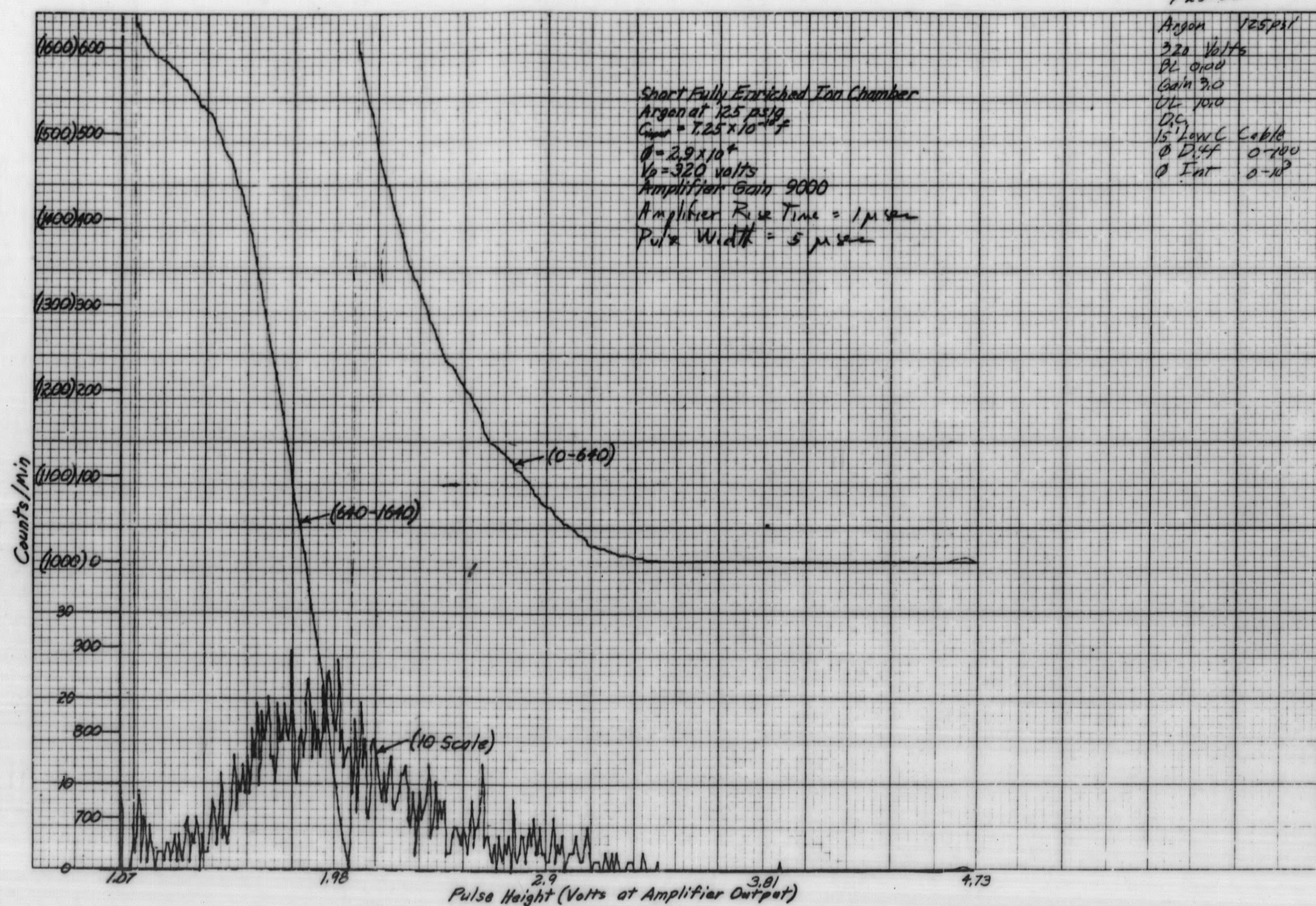


Figure 3-34. Differential and Integral Bias Curves

9-25-67

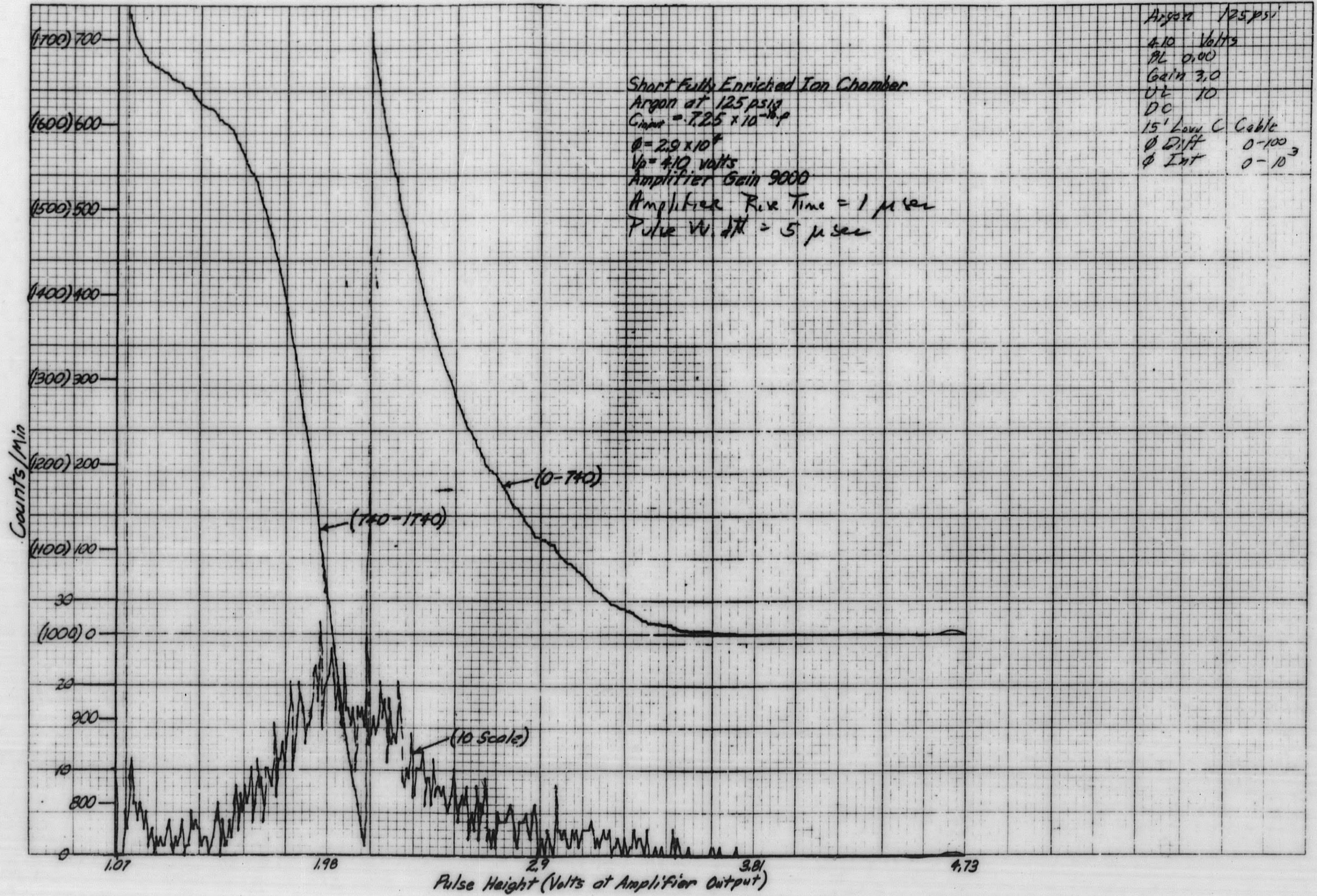


Figure 3-35. Differential and Integral Bias Curves

9-25-63

2

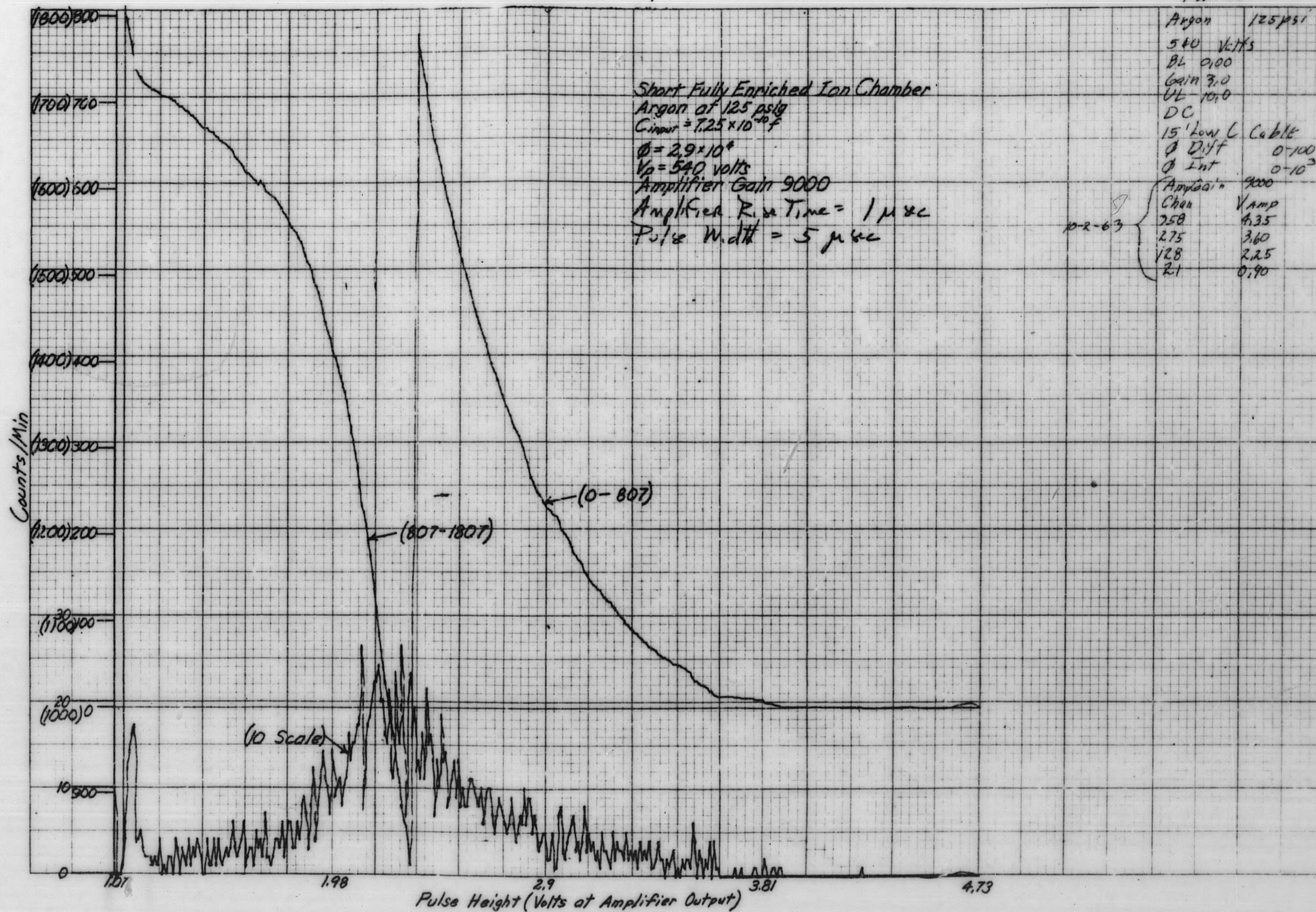


Figure 3-36. Differential and Integral Bias Curves

9-25-63 1

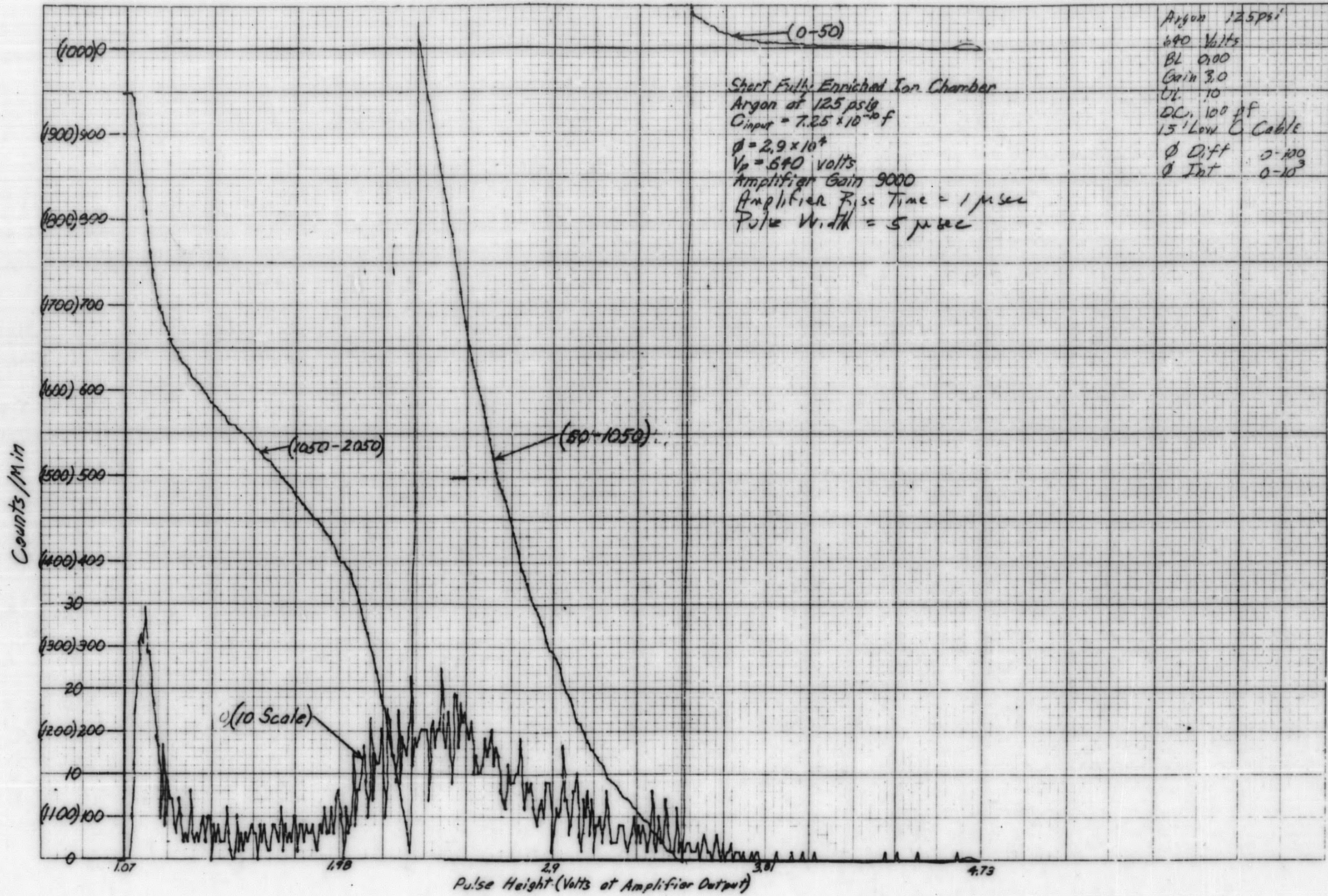


Figure 3-37. Differential and Integral Bias Curves

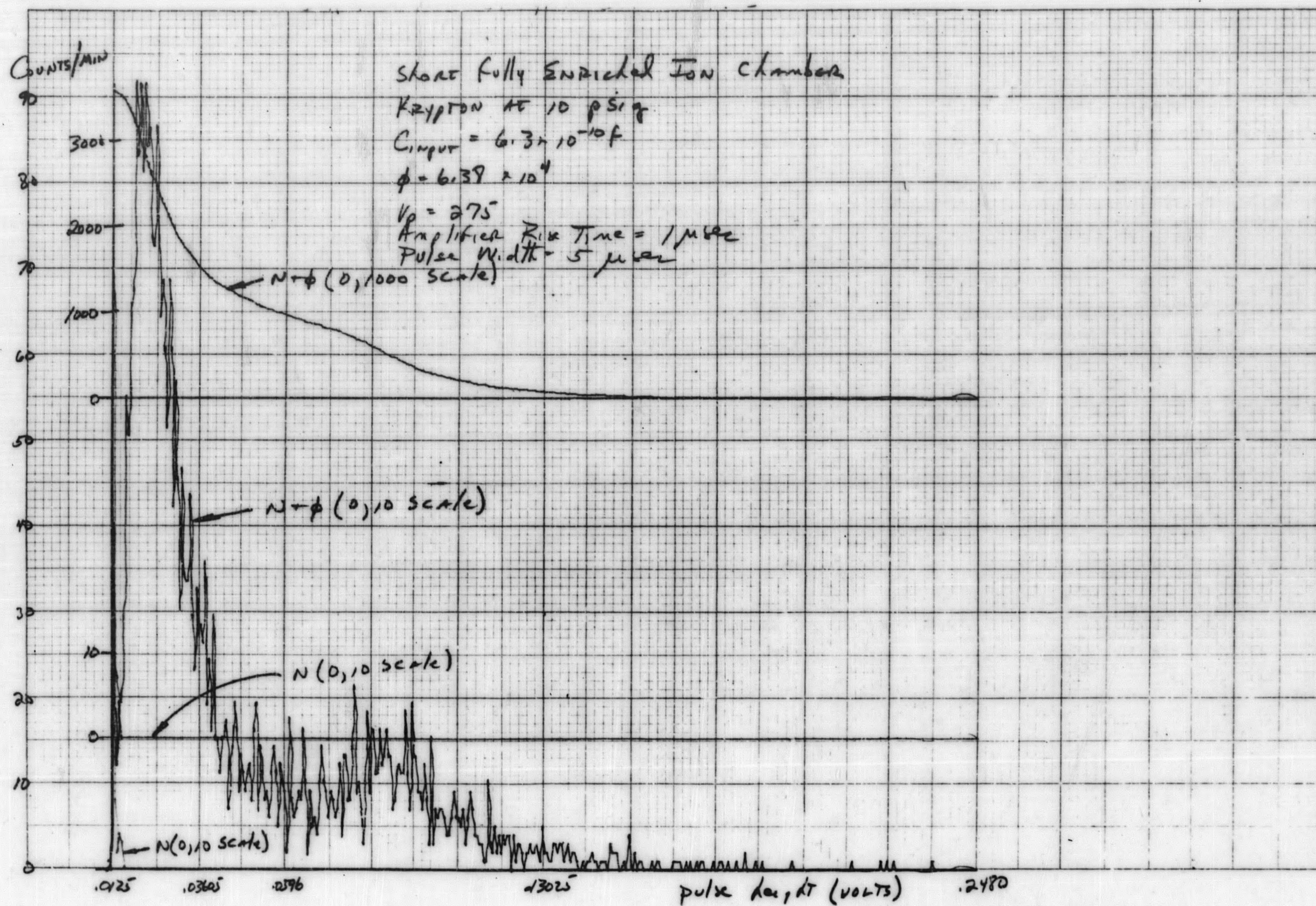


Figure 3-38. Differential and Integral Bias Curves

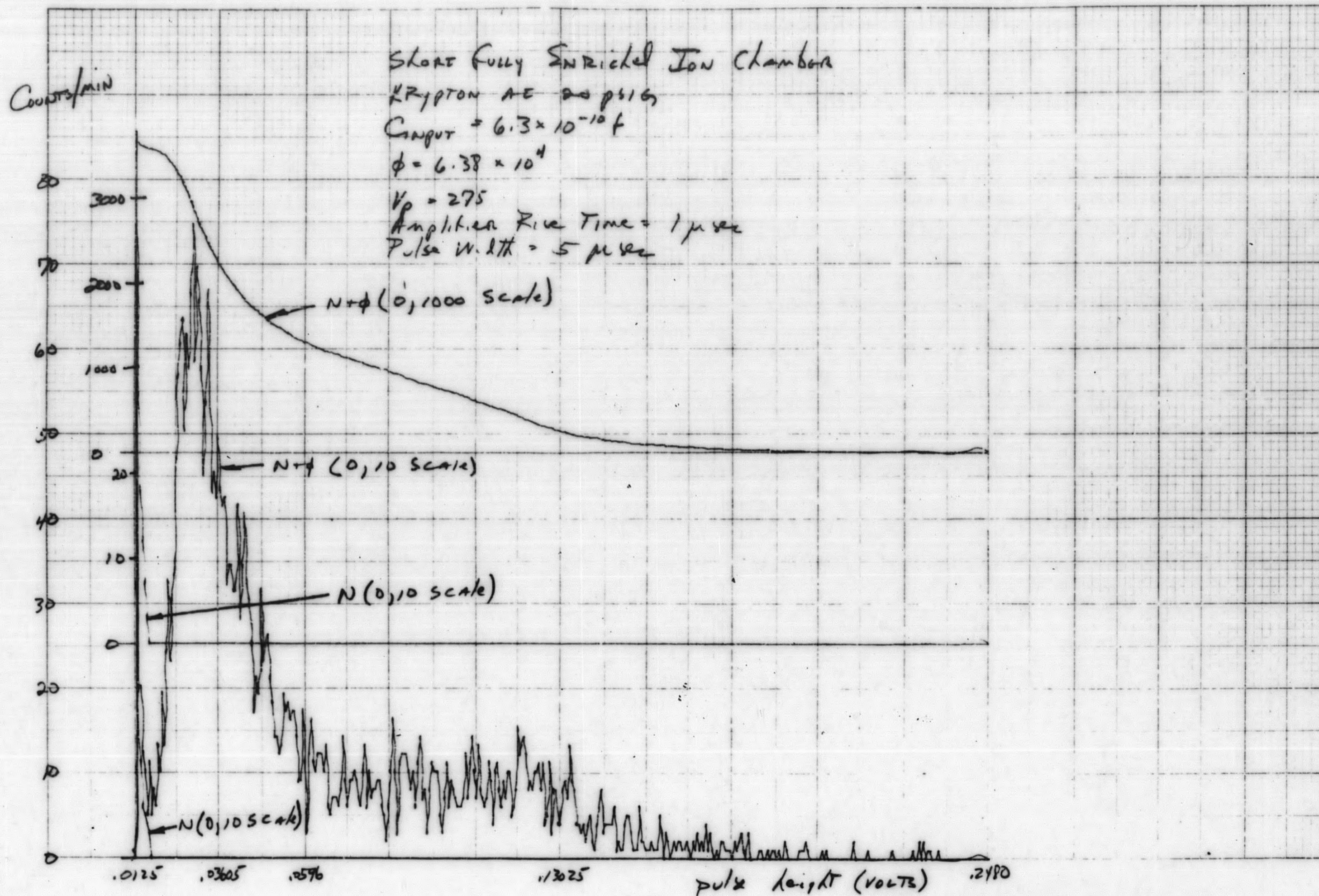


Figure 3-39. Differential and Integral Bias Curves

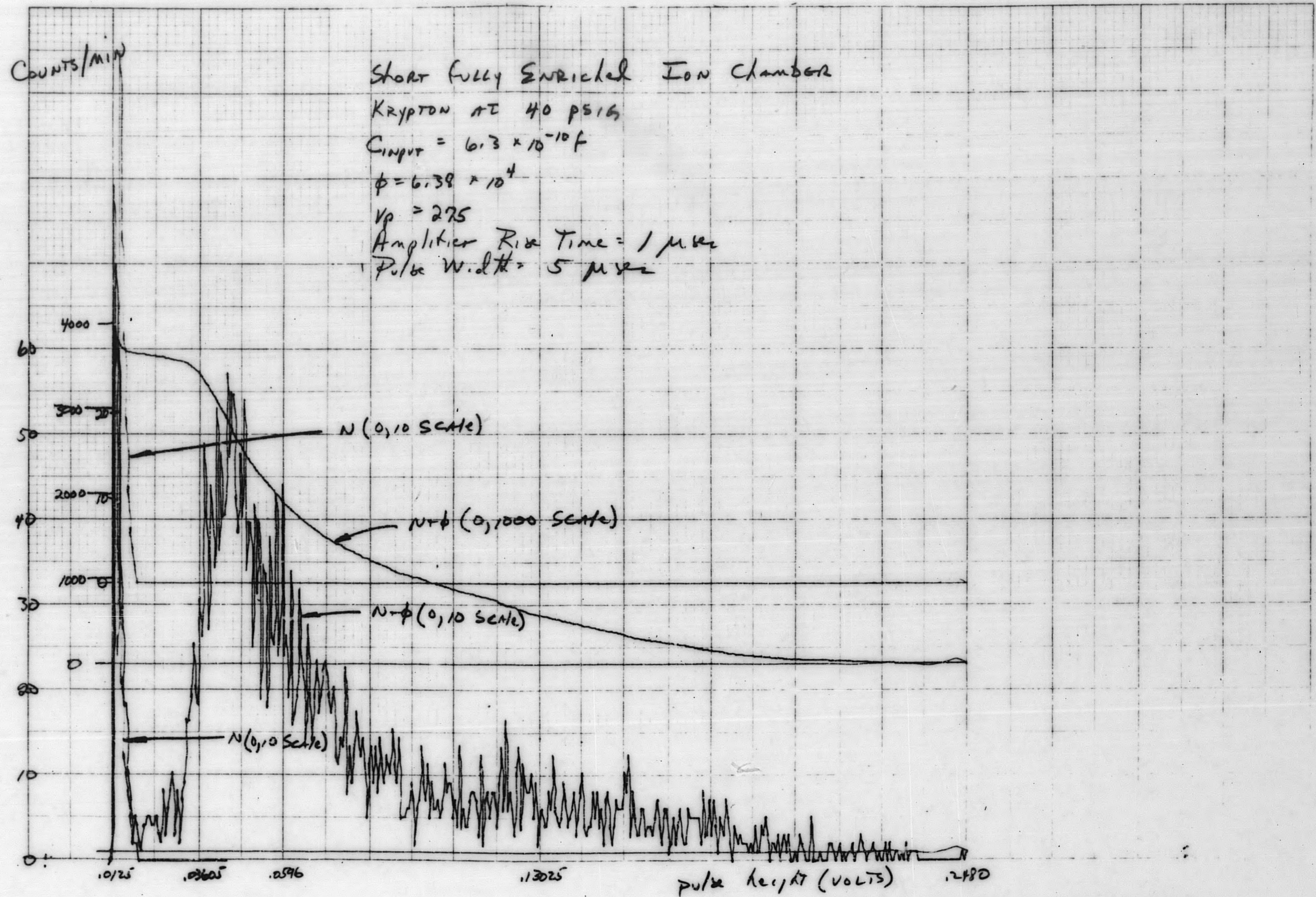


Figure 3-40. Differential and Integral Bias Curves

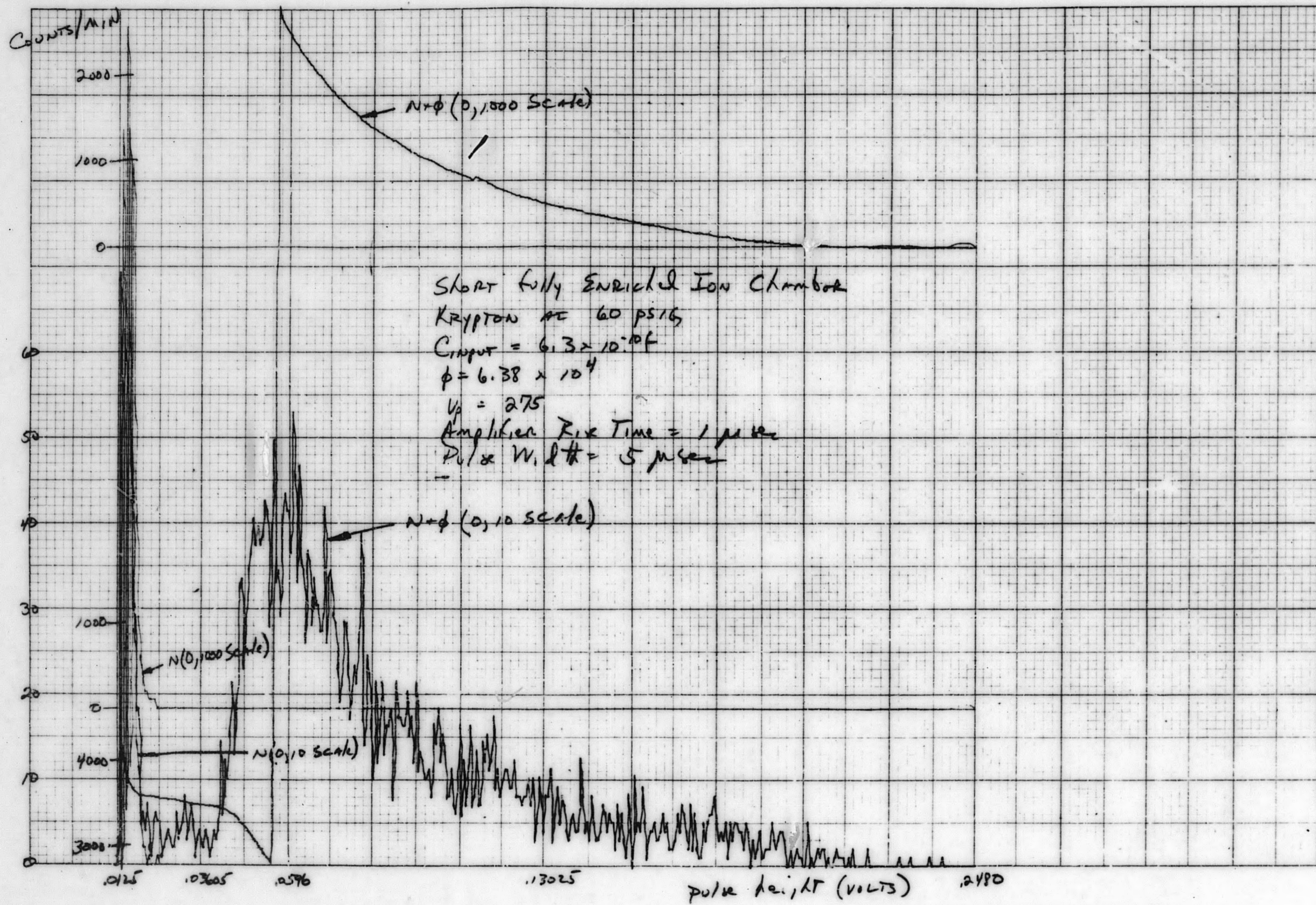


Figure 3-41. Differential and Integral Bias Curves

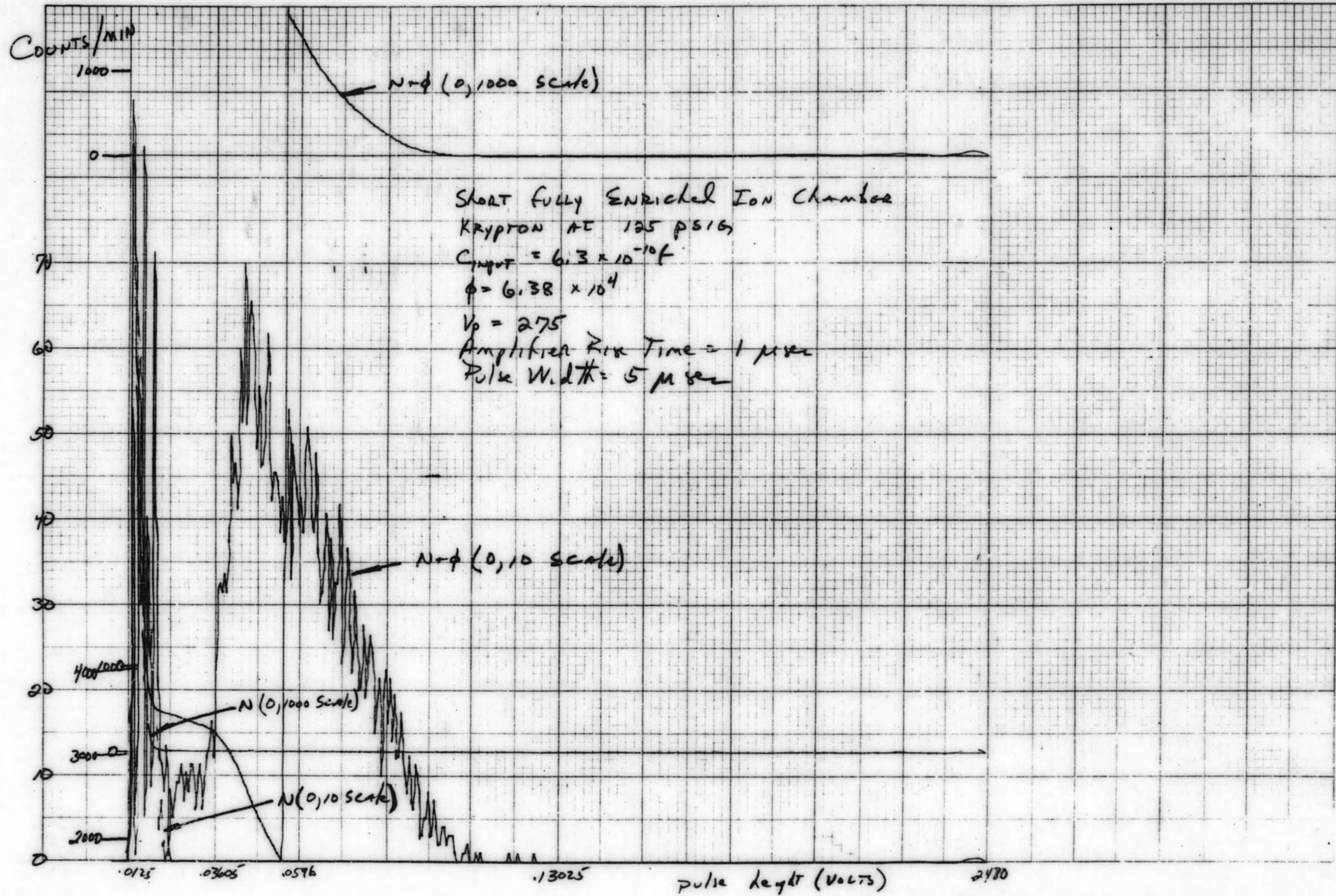


Figure 3-42. Differential and Integral Bias Curves

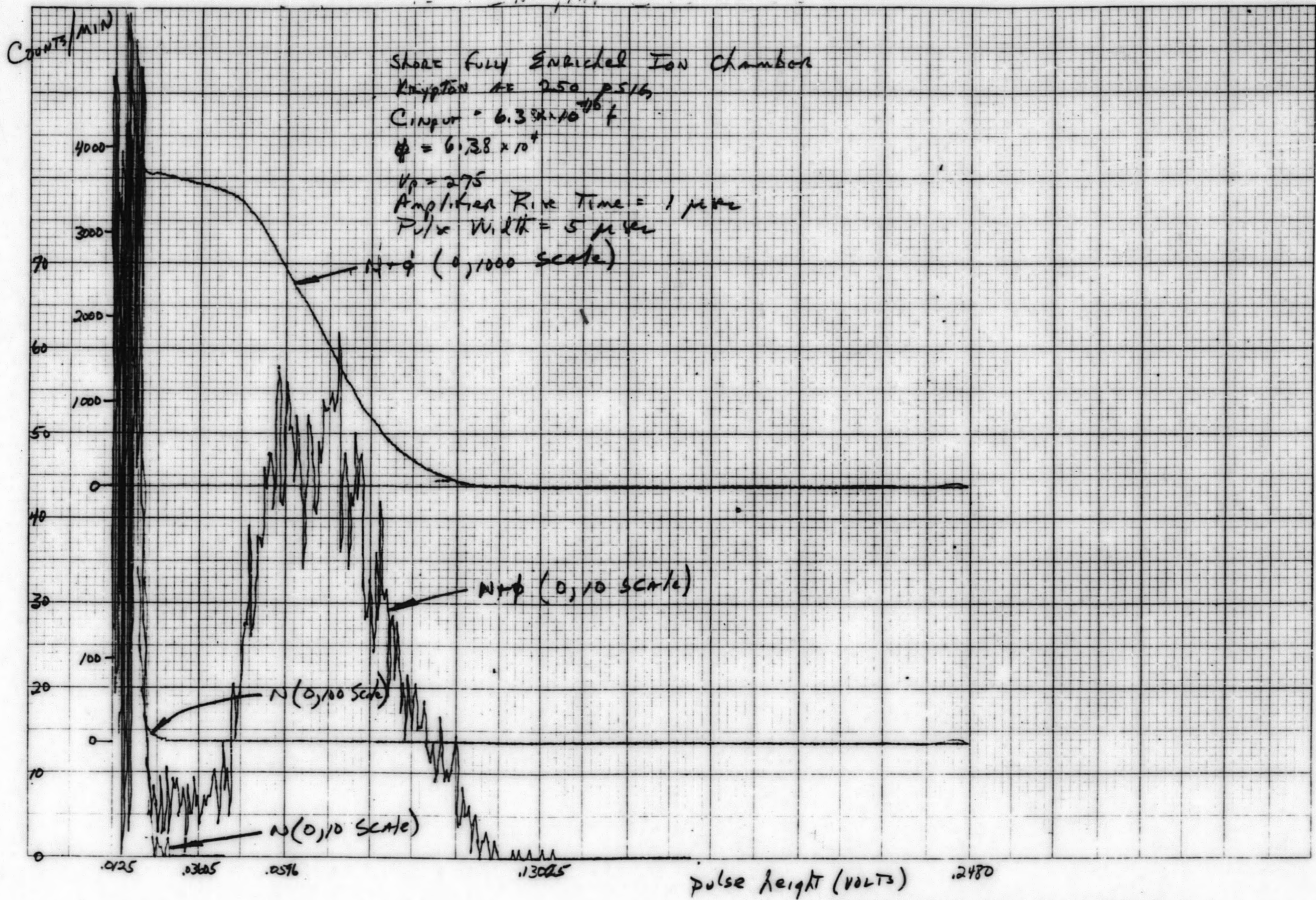


Figure 3-43. Differential and Integral Bias Curves

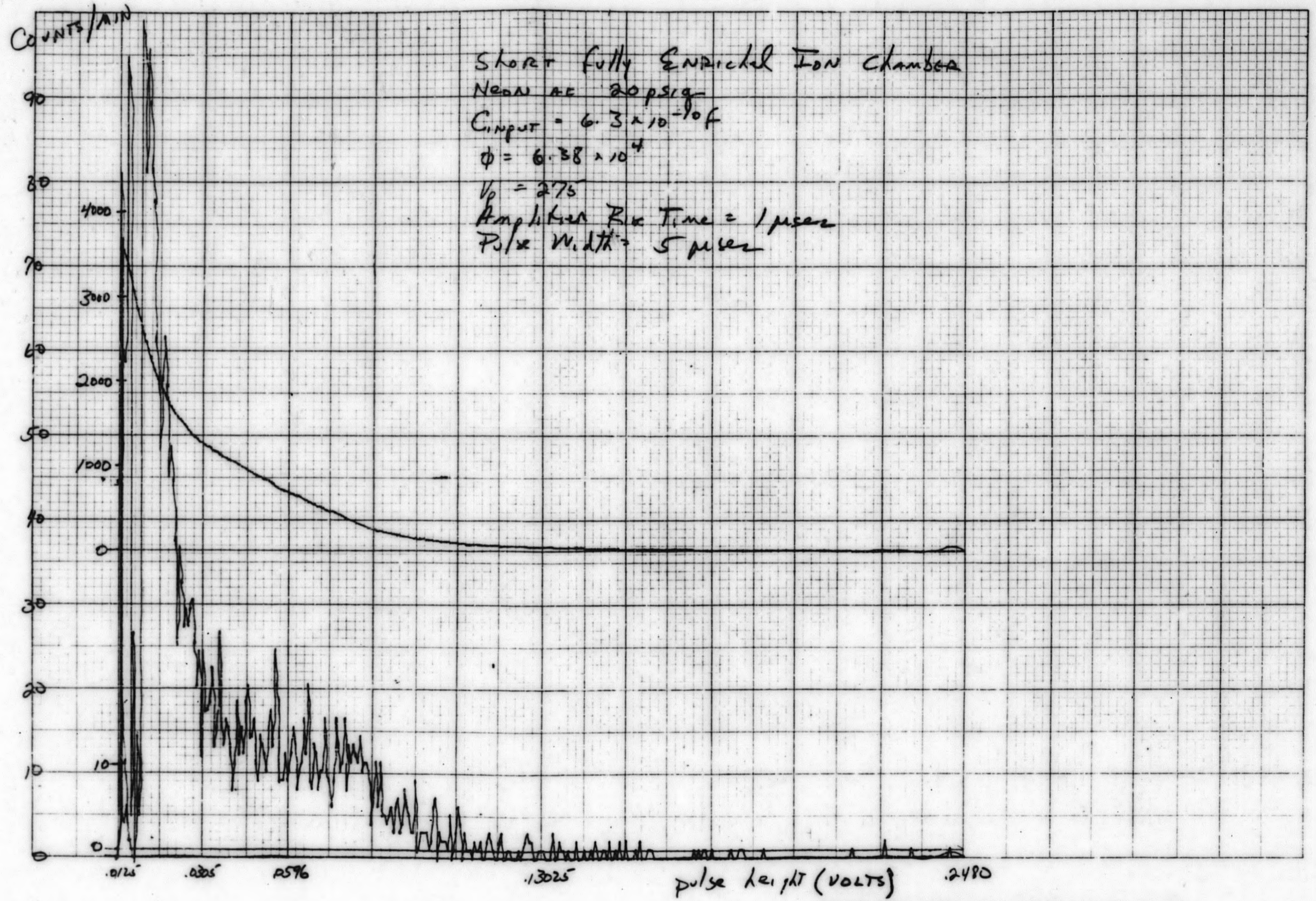


Figure 3-44. Differential and Integral Bias Curves

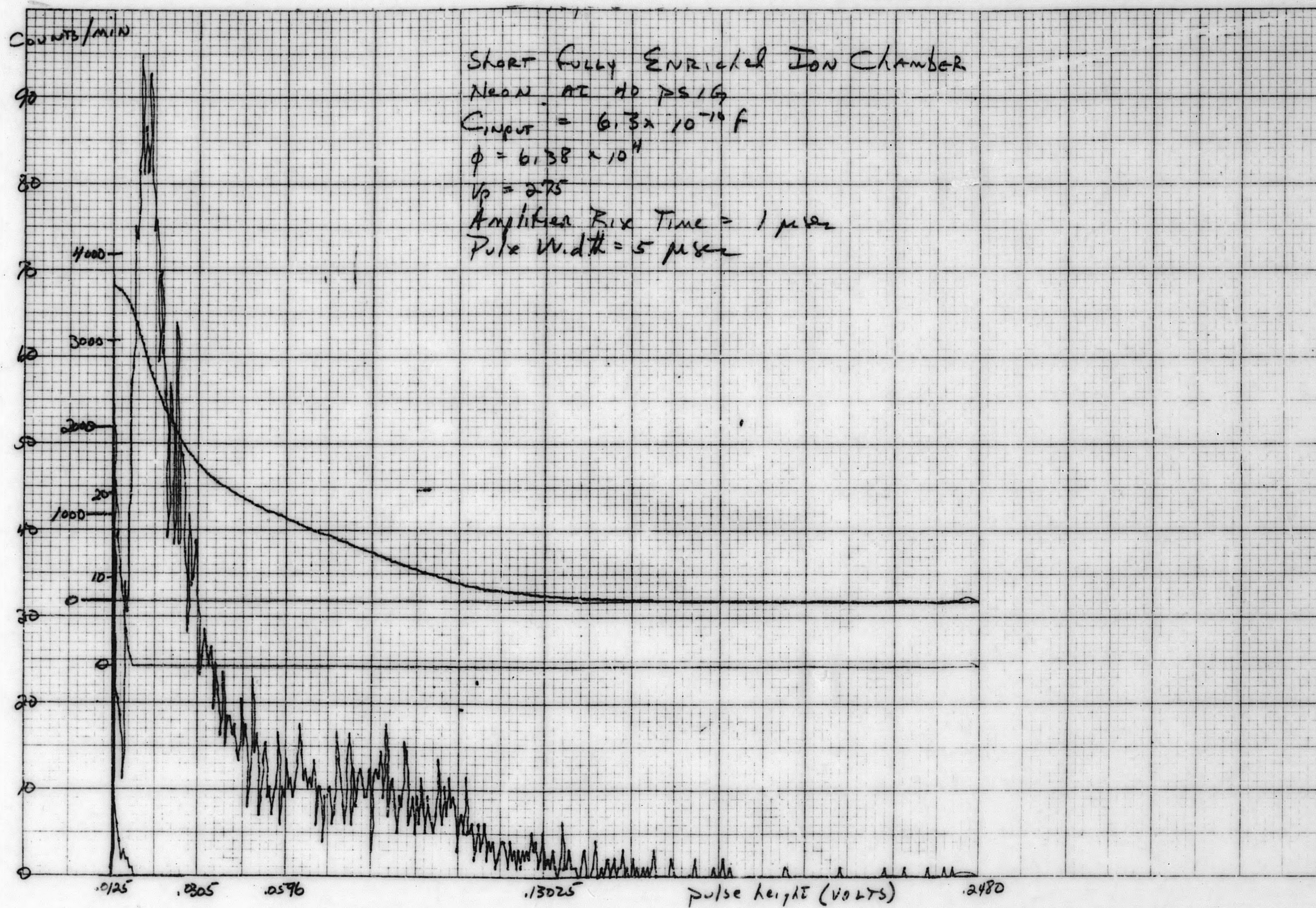


Figure 3-45. Differential and Integral Bias Curves

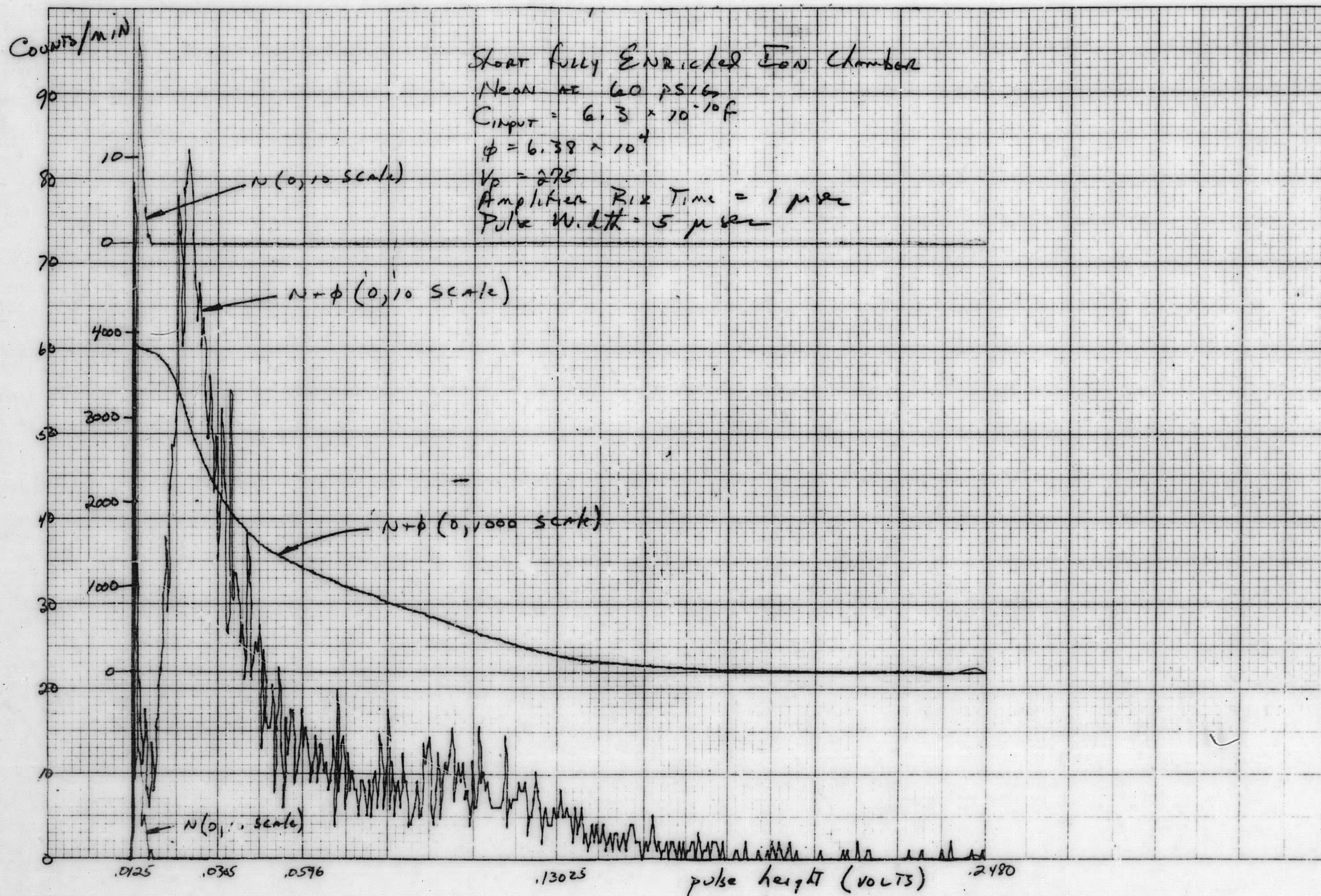


Figure 3-46. Differential and Integral Bias Curves

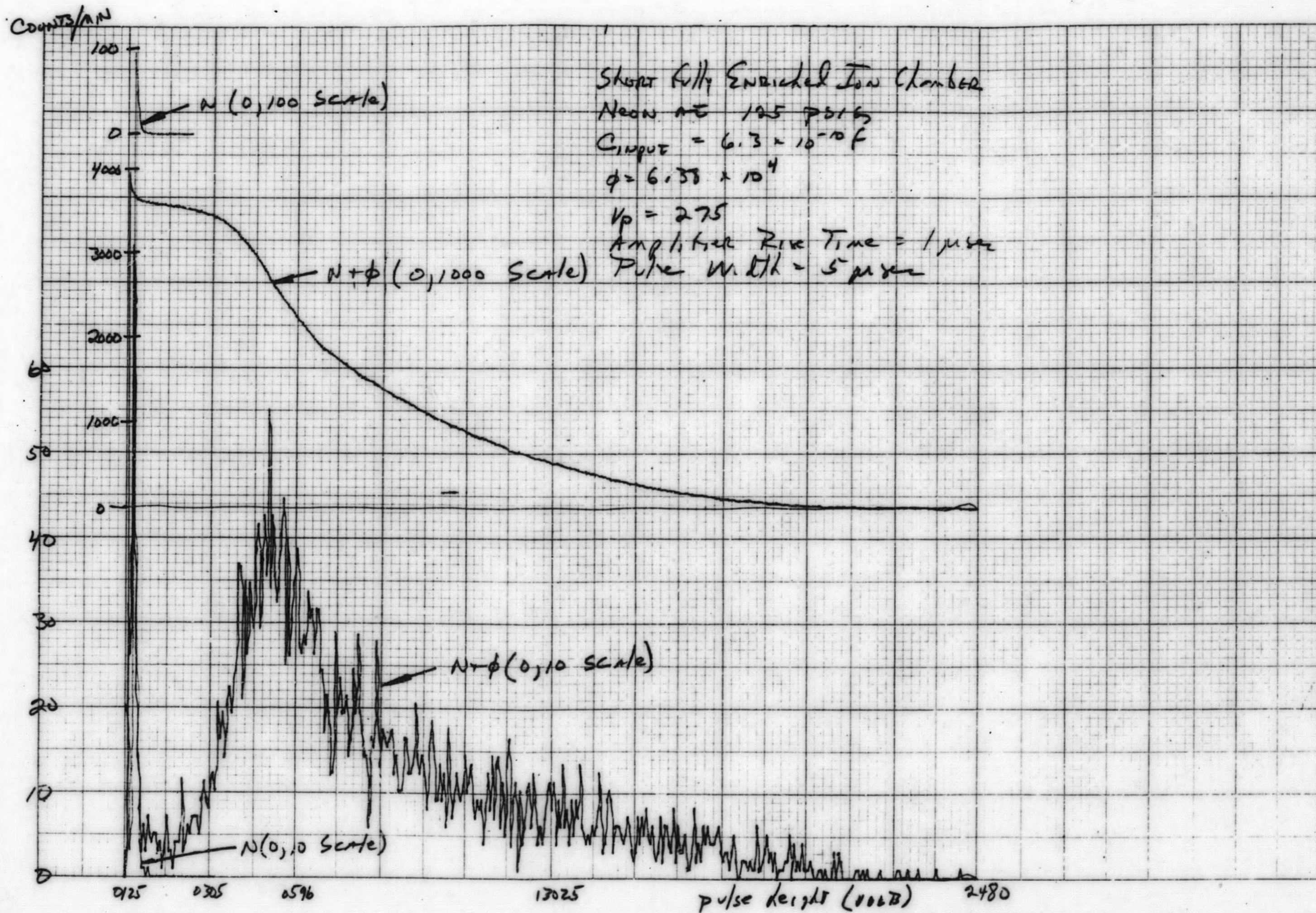


Figure 3-47. Differential and Integral Bias Curves

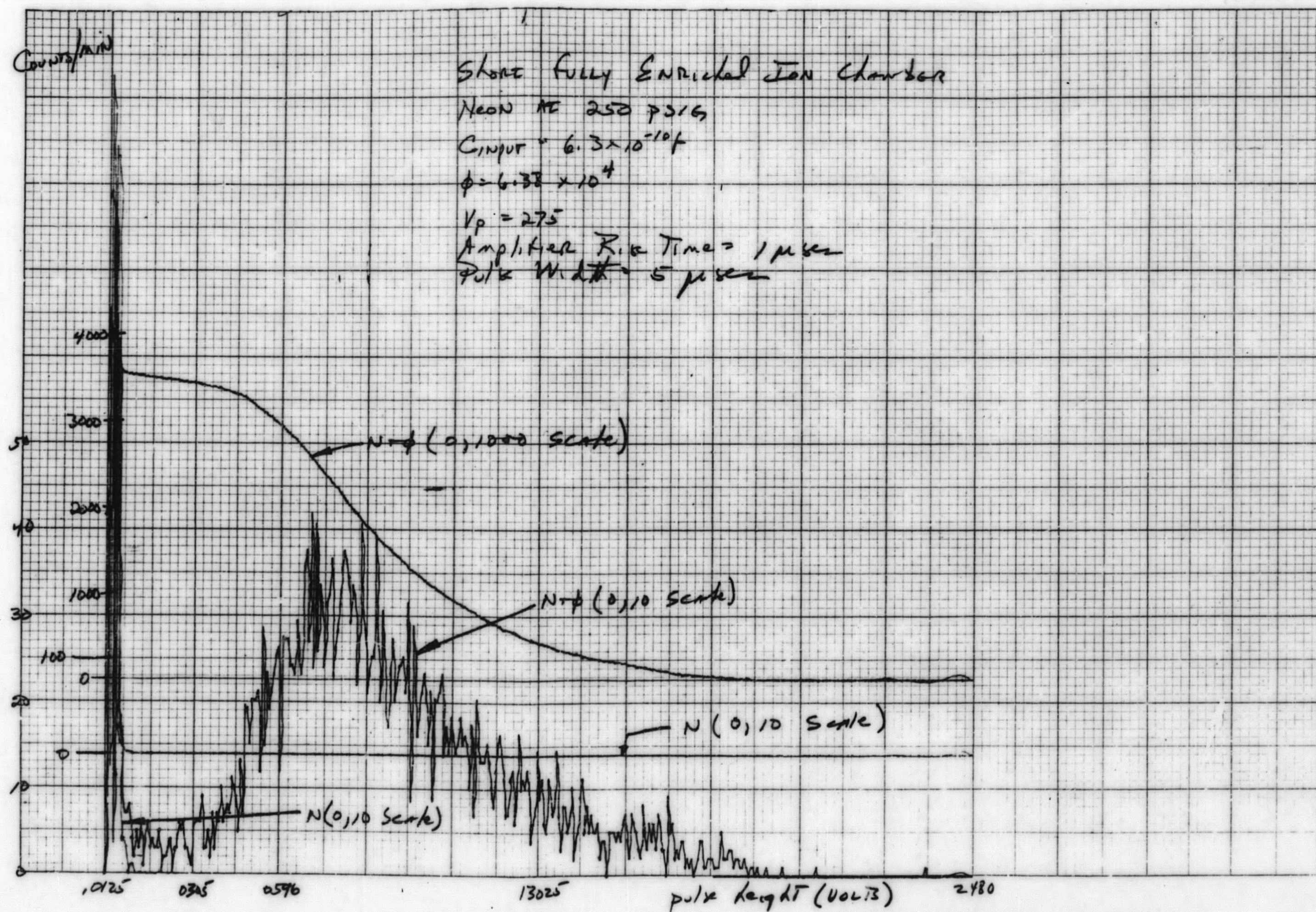


Figure 3-48. Differential and Integral Bias Curves

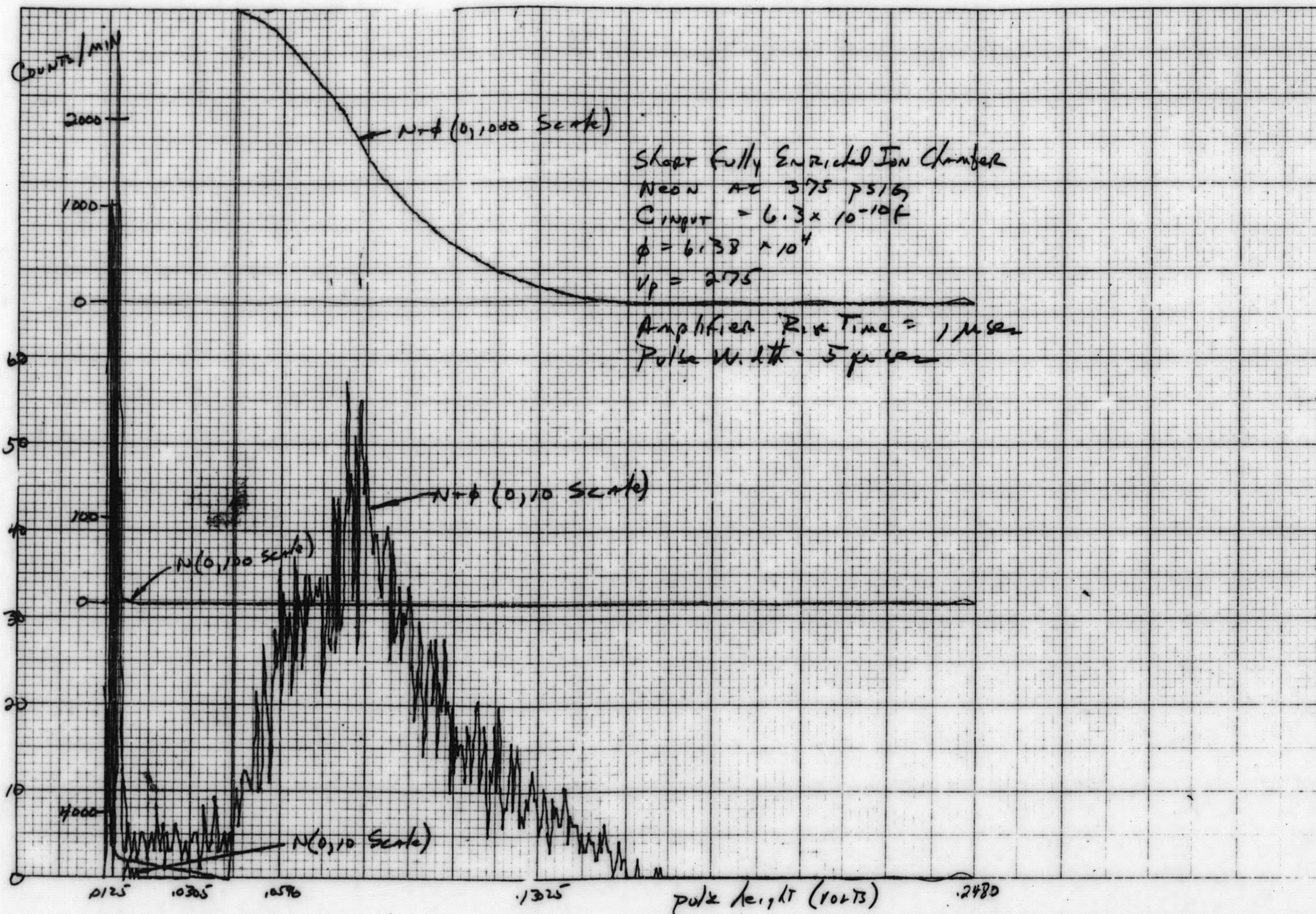


Figure 3-49. Differential and Integral Bias Curves

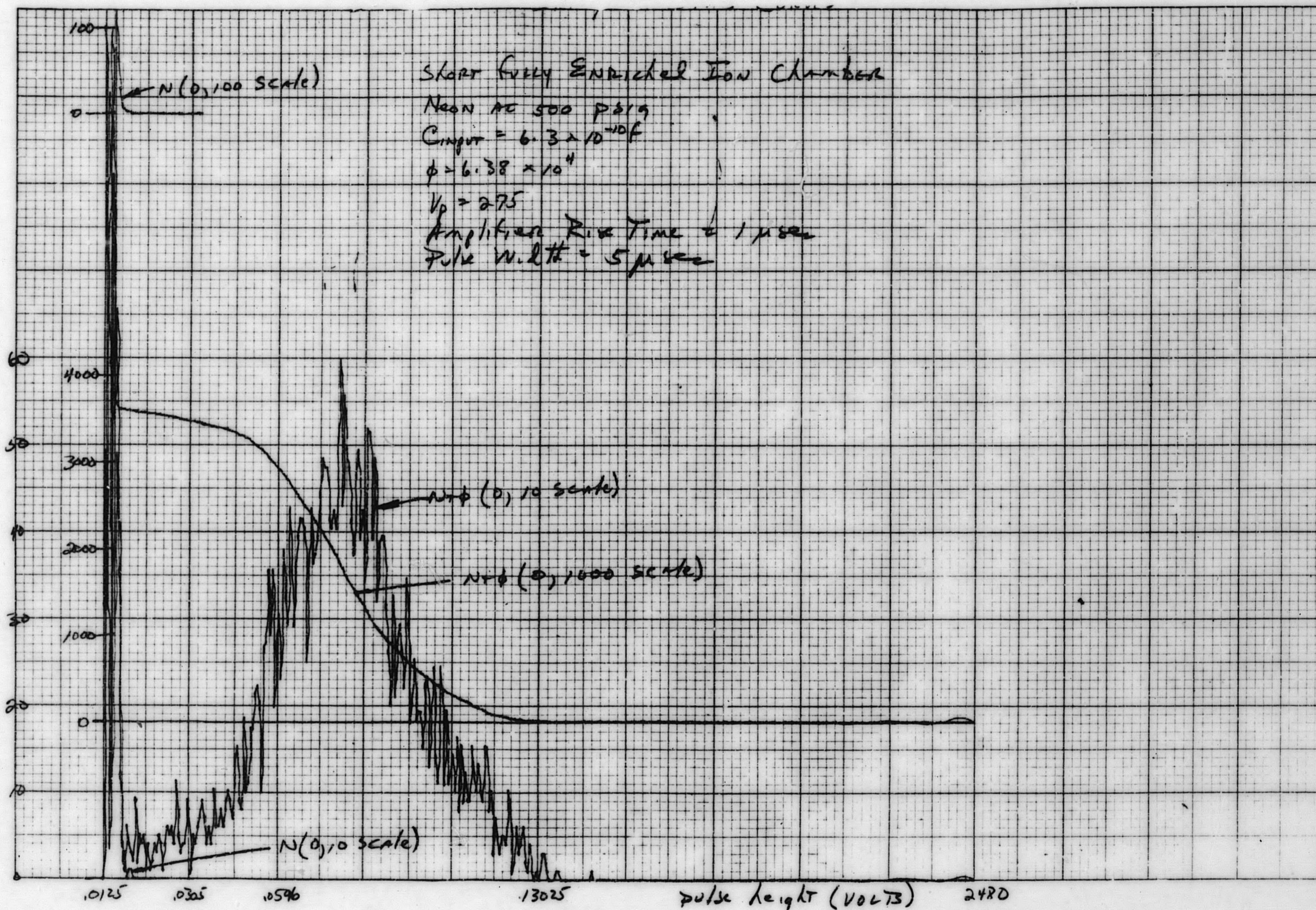


Figure 3-50. Differential and Integral Bias Curves

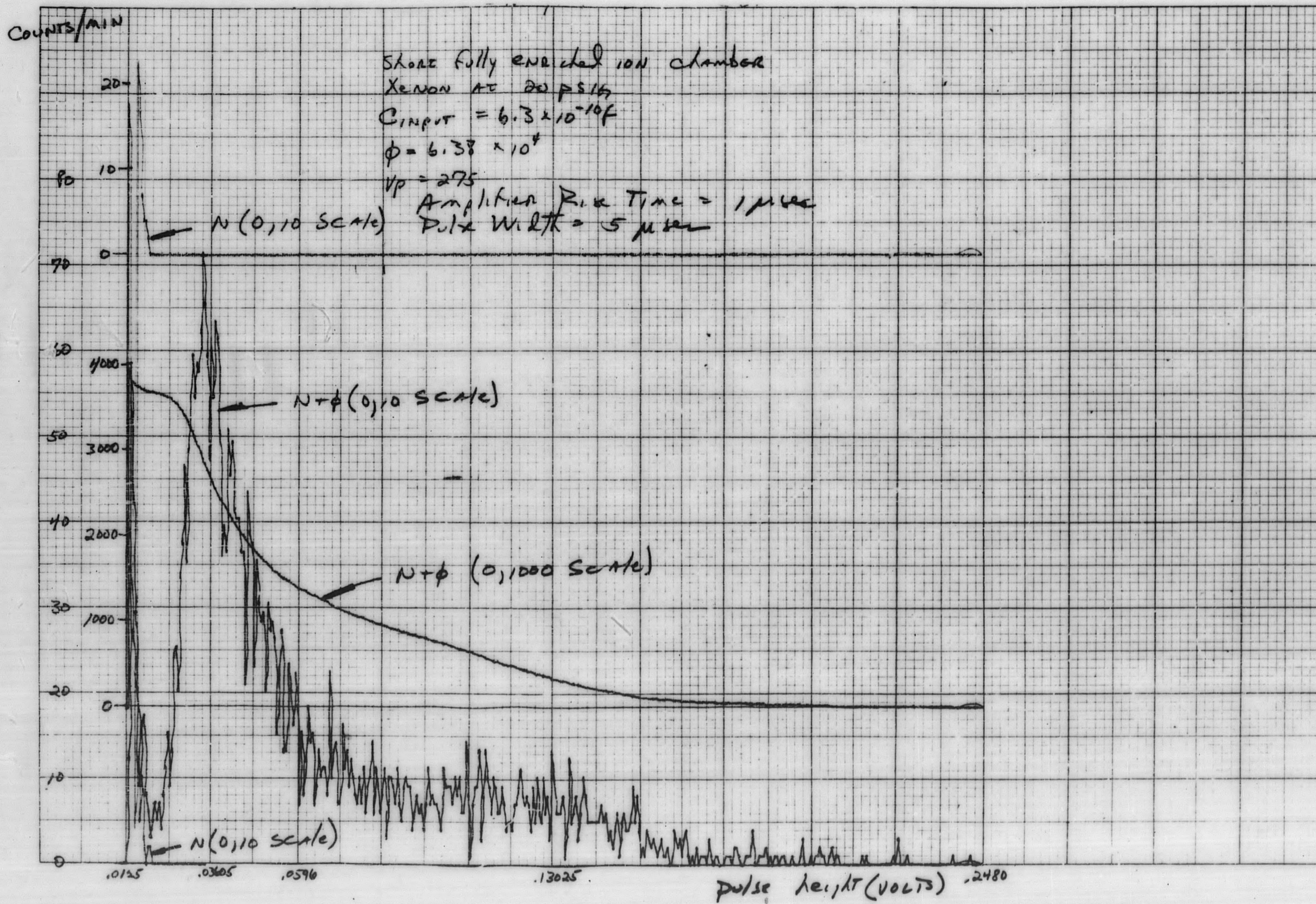


Figure 3-51. Differential and Integral Bias Curves

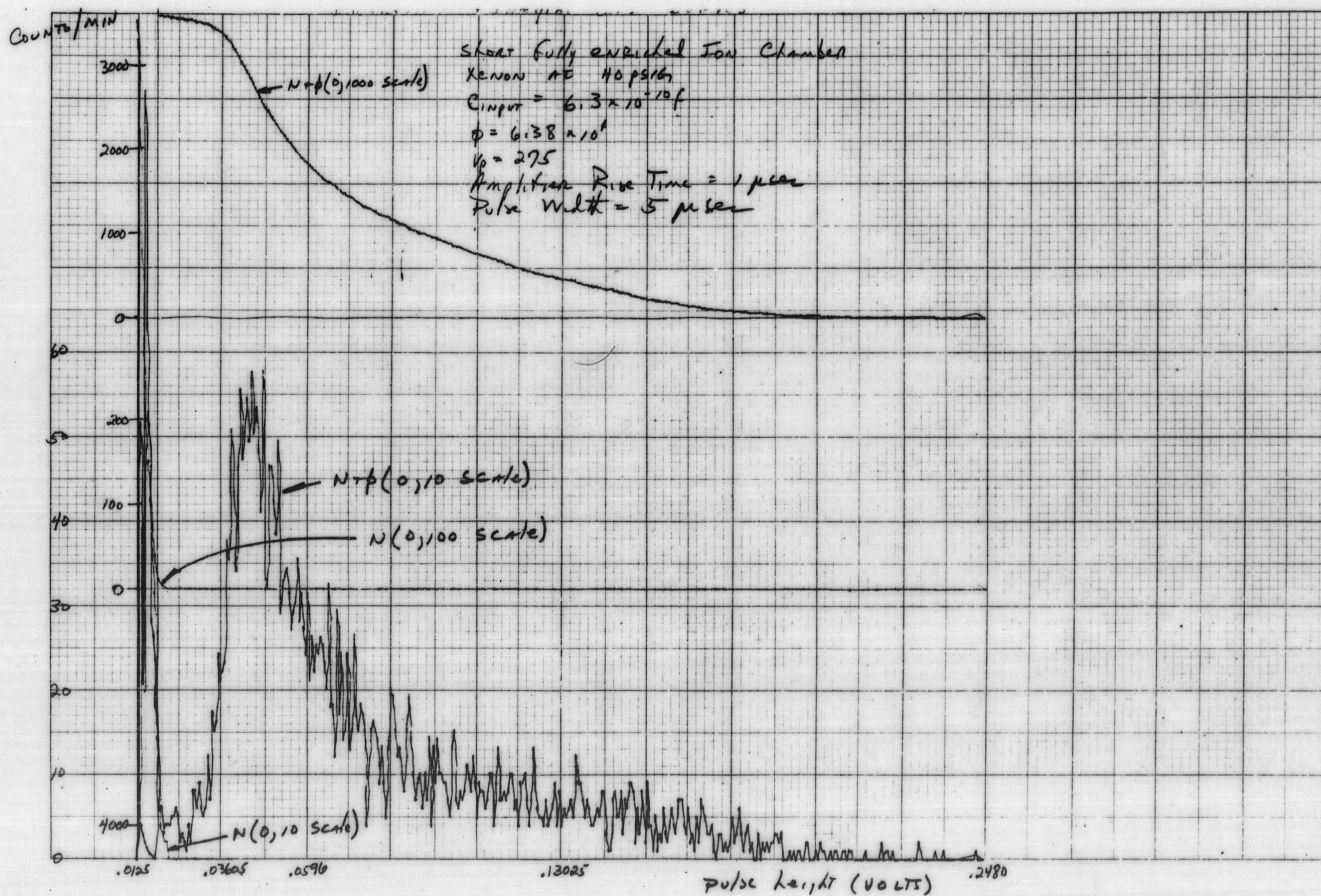


Figure 3-52. Differential and Integral Bias Curves

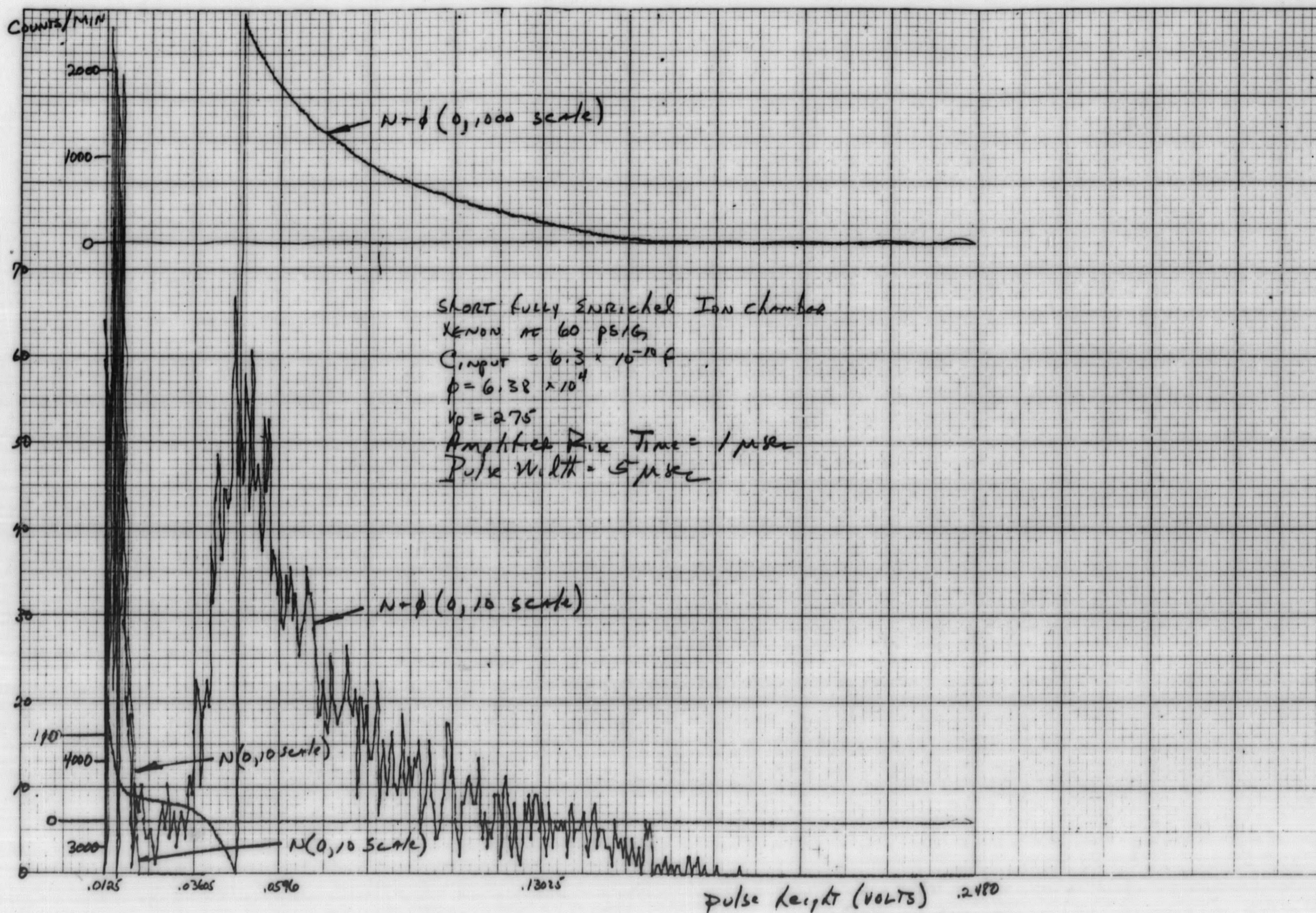


Figure 3-53. Differential and Integral Bias Curves

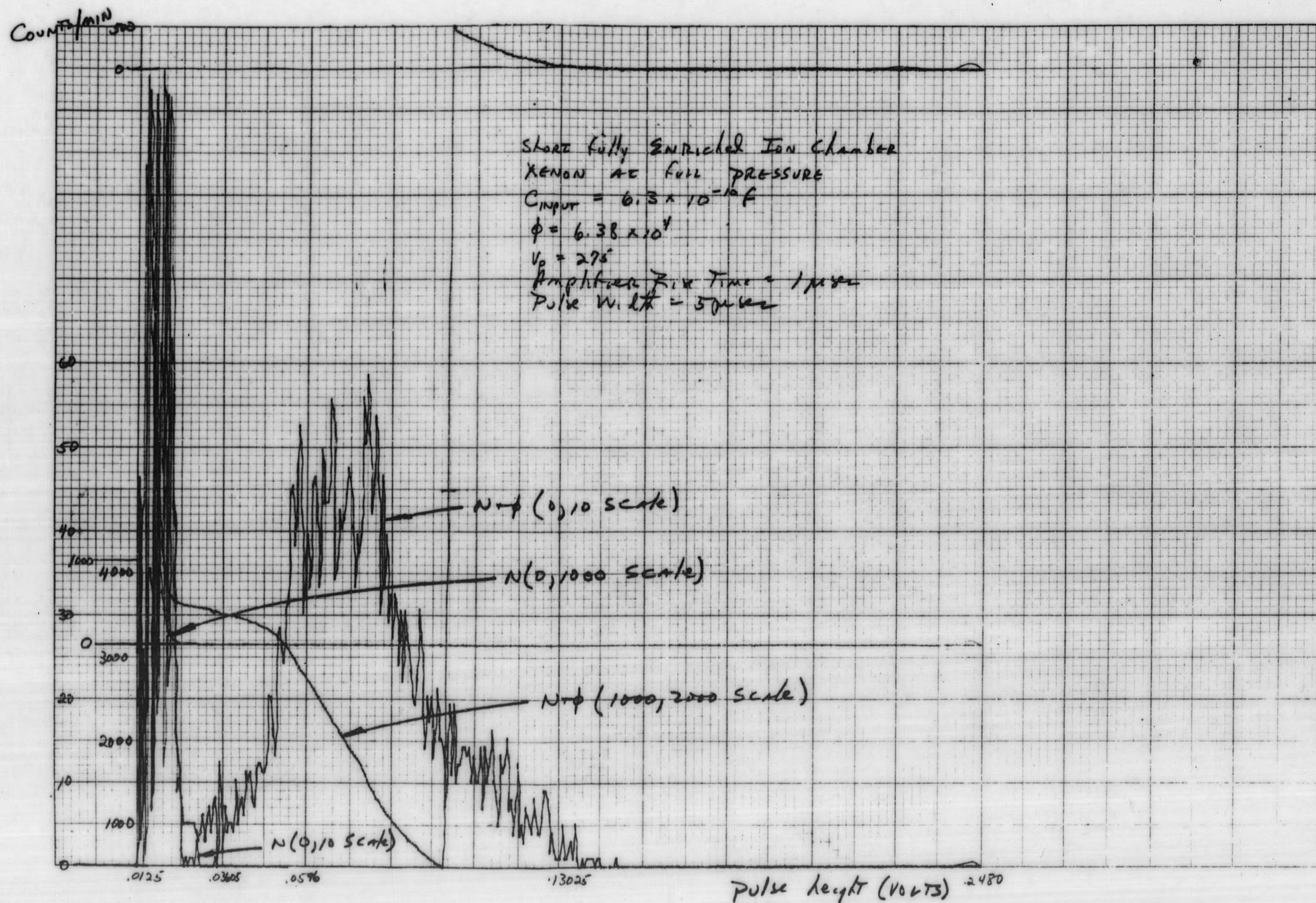


Figure 3-54. Differential and Integral Bias Curves

BIBLIOGRAPHY

Section II

- (1) Campbell, N. R. Proc. Camp. Phil. Soc. 15, 177, 310, 513 (1909).
- (2) Gillespie, A. B., Signal, Noise and Resolution in Nuclear Counter Amplifiers (1953).
- (3) Lichtenstein, R. M., "Radiation Measuring Instrument", U. S. Patent 2,903,591 (2/55).

Section III

- (1) Jesse and Sadouskis, Phys. Rev. 88, 417.
- (2) Jesse and Sadouskis, Phys. Rev. 90, 1120.
- (3) Curran, S. C., and Craggs, J. D., Counting Tubes, p. 15 (1949).
- (4) Wilson, R. S., Beghian, L. E., Collie, C. H., Holban, H. H. and Bishop, C. R.,
Rev. Sci. Instr. 21, 699 (1950).
- (5) Facchini, V. and Malvicini, A., Nucleonics 13, No. 4, p. 36 (1955).

END